Theoretical Models and Numerical Approaches to Nanoscale Microscopies and Spectroscopies of Plasmonic Systems

Claire Anne West

A dissertation
submitted in partial fulfillment of the
requirements for the degree of

Doctor of Philosophy

University of Washington

2021

Reading Committee:
David J. Masiello, Chair
Anne B. McCoy
Cody W. Schlenker

Program Authorized to Offer Degree:
Chemistry

University of Washington

Abstract

Theoretical Models and Numerical Approaches to Nanoscale Microscopies and Spectroscopies of Plasmonic Systems

Claire Anne West

Chair of the Supervisory Committee:
Professor David J. Masiello
Department of Chemistry

Harnessing electromagnetic and thermal interactions among single and coupled metal nanoparticle systems creates opportunities to advance scientific endeavors and enhance different engineered technologies. Designing these nanoparticle systems and measuring their manufactured properties pose two challenges which may be addressed through the development of analytic and numeric models. This dissertation contains models which describe the optical and thermal response of coupled, plasmonically active metal nanoparticle systems. The models are used to design different nanoparticle structures which support actively tunable properties. Also included in this dissertation are models of single-particle microscopy and spectroscopy measurements on plasmonic systems (photothermal-based measurements in Part II and electron energy loss measurements in Part III). These models are used to interpret experimental data obtained from collaborators. Feedback between theory and experiment allows the models to be verified and improved to more accurately approximate the different experimental observables and to design more advanced nanostructures with exotic thermal and electromagnetic properties.

TABLE OF CONTENTS

LIST OF FIGURES

LIST OF TABLES

GLOSSARY

LSP: Localized surface plasmon

DDA: Discrete dipole approximation

T-DDA: Thermal discrete dipole approximation

PSF: Point spread function

ACKNOWLEDGMENTS

An ecosystem of mentors, role models, mentees, and collaborators have enabled me to complete the following work. I wish to acknowledge a subset of those who were the most impactful.

First, I wish to acknowledge my advisor, Professor David J. Masiello, who consistently made time to teach innumerable scientific lessons and provide professional advice. I am thankful I had the opportunity to work in the group as a National Science Foundation Research Experience for Undergraduates student the summer before my senior year of undergraduate. Those positive experiences inspired me to return to his group for graduate school. Upon doing so, he created opportunities for me to work on many different research projects in collaboration with numerous interdisciplinary teams. He graciously and patiently worked with me through the growing pains I experienced by the transition from sunny Santa Barbara to the long, dark winters in Seattle. David taught me many invaluable research skills and a research ethos that I will take with me in my future career endeavors.

Next, I wish to thank my committee members. For my second-year exam, Professor Munira Khalil, Professor Joshua C. Vaughan, and Professor Lutz Maibaum. They helped me identify important ways for me to grow as a scientist. I look fondly back at the questions asked and advice given by my general exam committee members: Professor Munira Khalil, Professor Joshua C. Vaughan, Professor Anne B. McCoy, and Professor Vincent Holmberg. I now thank my thesis committee, Professor Anne B. McCoy, Professor Cody W. Schlenker, and Professor Elizabeth Nance for reading my dissertation and providing helpful feedback. One of my committee members who I wish to give extra acknowledgement to is Professor Anne B. McCoy for her continued support and mentorship throughout my time at UW. She

importantly helped me find confidence in myself as a scientist and leader.

I also wish to acknowledge the many collaborators I have had the pleasure to work with over the course of my Ph.D. These include Professor Stephan Link and his group at Rice University, Professor Katherine A. Willets and her group at Temple University, Professor Jon P. Camden and Agust Olafsson at the University of Notre Dame, Dr. Juan Carlos Idrobo at Oak Ridge National Laboratory, Professor Philip D. Rack and Grace Pakeltis at University of Tennessee, Knoxville, Dr. Bert de Jong at Lawrence Berkeley National Labs (LBNL), and Prof. Tess E. Smidt (formerly at LBNL), now at Massachusetts Institute of Technology. I feel very fortunate to have had the opportunity to work with and learn from these amazing scientists and engineers. In particular, I wish to acknowledge two collaborators Prof. Willets and Prof. Smidt who both made extra efforts to ensure my success. On many occasions, Kallie and Tess went out of their ways to advocate for me and make time to mentor me in ways that were pivotal to my career.

In addition to the faculty, there have been numerous graduate students and postdocs who have played critical roles in my academic work and personal well-being. In my early career as both an undergraduate summer student and as a graduate student, I received important mentoring from Dr. Charles Cherqui, Dr. Niket Thakkar, Dr. Steven Quillin, and Dr. Nicholas Montoni. In particular, my first office-mates Steve and Nick helped me tremendously by patiently showing me how to code, teaching me the basics of plasmonics, and wholeheartedly welcoming me into Seattle and the Masiello group.

Four other members of the Masiello group: Dr. Harrison J. Goldwyn, Dr. Jacob A. Busche, Dr. Kevin C. Smith, and Elliot K. Beutler, each deserve their own paragraph of acknowledgement for how positively impactful they have been to me throughout my time at UW. They have walked me through derivations, proof-read my proposals and manuscripts, and helped advise me on which scientific directions to take my research. Equally valuable have been the coffee walks, fountain laps, lunches on The Ave, hikes, camping trips, potluck

dinners, and pints at College Inn I have shared with the four aforementioned Masiello members as well as C. Praise Anyanwu. I will cherish the friendships we created, and hope that my future co-workers can be as wonderful of an influence as you all have been.

I also would like to thank the different postdocs who I have learned from and worked with during the more recent years of my PhD. I appreciated learning from Dr. Xiang-Tian Kong and Dr. Zhongwei Hu while working together on thermoplasmonics projects. I am thankful I was able to briefly collaborate with Dr. Marc Bourgeois and Dr. Aniruddha (Ronnie) Bhattacharya.

I have enjoyed mentoring the recent Masiello graduate students in the Masiello group: Siamak Khorasani, Austin Nixon, Nicole Panek, Andrew Rossi, and Matthieu Chalifour. To those whom I have had the opportunity to work with, thank you for being patient while I learned how to be a good mentor. I look forward to reading about the outstanding research you all will continue to do.

In my final year at UW, I worked closely with Danica Hendrickson at the Clean Energy Institute and the Molecular Engineering Materials Center. I am very thankful for the time she spent mentoring me, teaching me about education research, and providing me with the resources to explore the field.

Dr. Michael J. Wilensky, you have helped me tremendously during my time at UW. I am grateful for all the times you took to help me solve different physics / math problems and answer my coding questions. I am so appreciative for all of the multi-course meals you cooked for us after we both had exhausting days. I am consistently inspired by your drive and your curiosity. For these reasons, I acknowledge and thank you for the significant role you have had in the completion of my thesis. I look forward to continuing our lives together.

I also would like to acknowledge Tank. Even though you bite and scratch me with much more frequency than any of the others in this acknowledgment, your snuggles and playful antics provided me with much needed stress-relief in the final year of my dissertation.

To my brother, Matthew West, thank you for the extended talks we have together about math. I admire your relentless passion for mathematics and teaching.

Finally, I wish to thank my parents, Dr. William West and Deborah West, for supporting me throughout my life. It is impossible to acknowledge everything you have done for me because at every stage in my life you both have done everything possible to ensure my happiness and success. Dad, thank you for encouraging me to pursue physics and for charting the waters of graduate school for our entire family. It has been tremendously helpful over the years to be able to call you to ask for advice, and to share with you my research-related woes and triumphs. Mom, your unwavering work ethic inspired me and fueled the late nights and early mornings I needed to take to finish manuscripts and debug code. I wish to acknowledge all of my slack you both picked up because of our emphasis on my education. (This ranged from letting me leave the dinner table early without doing my dishes so that I could get a head start on my homework, to doing the heavy lifting to figure out how to move out and start the next chapter of my life while I was busy writing this dissertation.) I love you both so much and cannot thank you enough.

DEDICATION

to my family

Part I

INTRODUCTION

Chapter 1

HISTORICAL CONTEXT

1.1 An Abridged History of Light

For millennia, people have sought to understand and harness light to study the world around themselves. Some of the earliest evidence of humans manipulating light dates back to illustrations of lenses found in ancient Egyptian hieroglyphs and 8000 year-old anthropogenic obsidian mirrors found in Anatolia (modern-day Turkey).[1] Accompanying these early optical tools came different theories attempting to explain what light fundamentally is, and why it interacts with materials in different ways.[2]

One of the first recorded theories of light is attributed to the Greek philosopher Empedocles in the 5th century B.C. He proposed that light is a stream of particles which emanate from the eye. Over the following centuries many other philosophers proposed similar descriptions of light as a matter flux. This inaccuracy, however, did not prevent the correct theories of different light-matter interactions from arising. For example, different scholars around the world separately discovered and rediscovered Snell's Law of Refraction.[1] In 1662, Pierre de Fermat finally offered the correct explanation for this popular empirical formula by proposing that the speed of light is finite[2], and that light will travel slower in denser media.

While the early refraction experiments were not seemingly in conflict with the matter-flux description of light, diffraction experiments began to expose inconsistencies. Francesco Grimaldi, and subsequently many other philosophers in the late 1600s, conducted different diffraction-based experiments with light and proposed new theories of light as a wave.

---

[1]Snell's Law was first described by the Persian scientist, Ibn Sahl in 984. Although other scientists independently derived the formula, it was named after Willebrord Snellius (Snell) posthumously.

[2]Seventeen years later Ole Christensen Rømer demonstrated this fact experimentally.

Christiaan Huygens notably published a theory of light which demonstrates mathematically that light may consist of radiating spherical waves which interfere to form a total wavefront (later named the Huygens-Fresnel Principle). This led to the breakthrough and controversial proposition that light is a wave. This theory was in direct conflict with Newton's corpuscular theory of light which could explain polarization, while at the time the wave theory could not. However, in the early 1800s Thomas Young performed his now famous double slit experiment which showed definitively that light is a wave. It was Augustin-Jean Fresnel in 1821 who finally proposed the correct explanation of light. Over the course of his lifetime, he was able to change the minds of many famous skeptics of the wave theory and ultimately garner acceptance from the scientific community at large.

1.2 Modern Physics

While Young and Fresnel were characterizing the wave-like properties of light, Michael Faraday was conducting important experiments with electricity and magnetism. In 1864, James Maxwell used Faraday's findings, in companion with experiments of his own, to discover that electricity and magnetism and light are physically the same phenomena. Equally important, Maxwell produced a set of twenty differential equations which form the foundation for describing different electromagnetic interactions. Oliver Heaviside reduced the original twenty equations down to the four commonly used today. Following Maxwell's breakthroughs came many scientific discoveries and innumerable opportunities for further scientific exploration. For brevity, all subsequent endeavors will not be summarized in this dissertation. Instead, this remainder of this section will focus on the emergent solutions to and approximate models of nanoscale light-matter interactions.

An important outstanding question during this time was the mathematical solution to light interacting with a spherical particle. In 1869, John Tyndall got close to an answer when he discovered that light scattering off nanoparticles creates a blue hue. He hypothesized that this could be what causes the sky to appear blue. It was after using Maxwell's unification of electromagnetism and light that Lord Rayleigh (John William Strutt) proved these conjec-

tures in 1881 by formulating a theoretical framework which describes how light scatters off particles much smaller than the wavelength of that light (now referred to as Rayleigh scattering). While others added to this framework to enable the study of more diverse sphere materials and sizes, the theory was still limited to very specific conditions. Finally, in 1908, Gustav Mie published an all-encompassing solution to the scattering by a spherical particle of any size by solving Maxwell's equations for an electromagnetic plane wave interacting with a homogeneous sphere.[3] Despite deriving the closed form expressions for the scattering, absorption, and extinction of light interacting with a sphere, this solution did not become useful until much later when computers could evaluate the functions numerically.

1.3 The Emergence of Nanoscience and the Field of Plasmonics

The next fifty years ushered in a new flavor of science characterized by the invention of quantum mechanics. In this era, the nature of light was brought into question again. One important discovery, foundational for the scope of this dissertation, was made in the 1950s by David Bohm[4] and David Pines. Based off of experiments done by Rufus Ritchie [4] and others [5] on the energy lost by electrons in gases and thin foils, they proposed the correct explanation of these energy losses to be from surface waves of the conduction band electrons. These collective oscillations of electrons, or plasma oscillations, are now called plasmons. Two different of surface plasmon excitations were classified during this time: surface plasmon polaritons and localized surface plasmons (LSPs). The latter will be subject of this dissertation.

Despite LSPs being mathematically discovered in the 1950s - 1960s, their unique proper-

[3]Gustav Mie was not the only person to arrive at this solution. Ludvig Lorenz and others independently derived the same result.

[4]Of the different physicists discussed so far, Bohm has a particularly unusual history. Bohm was an American and an active communist during World War II. He was a PhD student in Robert Oppenheimer's research group, but was disallowed from participating in the Manhattan Project due to his political ideologies. However, while completing his dissertation, his work was found to be useful for the Project. It was immediately classified which prevented him from accessing his work. Thus, he could not write his thesis or defend! Fortunately, Oppenheimer vouched for Bohm, and he was awarded a PhD. For more on Bohm's life, see Ref. [3]

ties have been unknowingly exploited dating back to the Romans who used metallic nanoparticles in their stained glass and to create the famous color-changing Lycurgus cup. Faraday also accidentally created a gold nanoparticle solution with plasmonic properties. He observed it's brilliant ruby color, and made predictions about the underlying physics. More recently, Richard Zsigmondy (the inventor of the dark-field microscope) made observations of gold nanoparticle colloids; it is believed that these observations inspired Mie to develop his theory.[5]

In addition to the beauty of metallic nanoparticle colloids, scientists have discovered more practical applications of LSPs. One particularly useful application has been the development of different surface-enhanced spectroscopies. For example, in 1973, scientists, at the time unknowingly, used a now-popular technique: surface enhanced Raman spectroscopy (SERS). With its scientific explanation coming a few year later, researchers realized they could use the intense local fields produced by LSPs to amplify the Raman signal from a sample. This enabled the characterization of molecules down to the single-particle level. Other emergent applications in the more recent years include using LSPs as biosensors for molecular detection, smaller and safer data storage technologies, low-electricity water purification systems, and less-invasive photothermal therapies.

1.4 Microscopies and Spectroscopies for Nanoscience

Observing and measuring the properties of nanoparticles and other nanomaterials[6] requires sophisticated microscopes. This is because microscopes designed to perform at these small length scales must be built to overcome the diffraction limit. The first microscopes which were made in the fifteen to sixteen hundreds were used to observe much larger objects (e.g, cells, bacteria, protozoa) by using lenses to focus and magnify light. In 1873, Ernst Abbe discovered that these light-based microscopes would have a fundamental limit on their

[5]Zsigmondy received the Noble Prize in 1925 for his work using microscopy on colloids.

[6]I will use the word *nanomaterial* to refer to any material with nanometer features.

resolution which would prevent the study of objects smaller than the diffraction limit:

$$d = \frac{\lambda}{2n_b \sin\theta} = \frac{\lambda}{2\mathrm{NA}} \tag{1.1}$$

where d is the minimum diameter light may be focused to, λ is the wavelength of light, n_b is the refractive index of the background, θ is the angle of the cone of focused light, and NA is the numerical aperture of the lens.[7] Thus, new instruments were needed in order to gain accurate images of objects at the nanoscale.

One critical technological advancement came when Ernst Ruska and Max Knoll built the first transmission electron microscope in 1931. It was discovered that accelerated electrons in a vacuum behaved similar to light in that electric and magnetic fields could be used as lenses to bend and shape the electrons' trajectories. Given that the electrons would not be limited to the diffraction limit of light, electron microscopes were shown to be a clear alternative to optical microscopes.

While microscopes may be used to create images of objects, spectroscopes are used to measure the color content of light. In the early days, spectroscopes could simply be a prism which diffracts white light into its different colors. Two important spectroscopies that are critical measurements for determining the properties of plasmonic system are of the light absorbed and scattered by the nanomaterial. Performing these measurements is very challenging on the single-nanoparticle level. For both scattering and absorption, the signal is much weaker than background signal and is thus very difficult to detect. Therefore, many different kinds of spectroscopy have been proposed and implemented over the years. The most common scattering technique, dark-field spectroscopy, was expanded upon in the 2000s to both image and measure scattering spectra of metal particles.[6, 7]. One experiment for measuring absorption is photothermal contrast spectroscopy [8]. There have been many other approaches, but none which are ubiquitous.

---

[7]The best numerical apertures modern lenses can achieve is around 1.4-1.6.

1.5 Outline of Dissertation

My contributions to this field are summarized in the following publications and in preparation manuscripts. The five manuscripts I first and co-first authored are included in the main text of this dissertation.

1. **West, C.**, Shooter, J., Willets, K., Link, S., & Masiello, D. Nonlinear Effects in Photothermal Imaging of Strongly Scattering Plasmonic Nanoparticles. In preparation.

2. **West, C.**, Hendrickson, D., & Li, X. Assessing the Impact of a Virtual Nanoscience Summer Camp on Middle - High School Students' Engagement with Content and Science Identity. In preparation.

3. Reinhardt, P., Crawford, A., **West, C.**, DeLong, G., Link, S., Masiello, D., & Willets, K. Toward Quantitative Nanothermometry Using Single-Molecule Counting. J. Phys. Chem. B 125, 44 12197-12205 (2021). Ref. [9].

4. Jebeli, S.,* **West, C.**,* Lee, S., Goldwyn, H., Bilchak, C., Fakhraai, Z., Willets, K., Link, S, & Masiello, D. Wavelength-dependent photothermal imaging probes nanoscale temperature differences among subdiffraction coupled plasmonic nanorods. Nano Lett. 21, 12 5386-5393 (2021). Ref. [10].

5. Baiyasi, R., McCarthy, L., Goldwyn, H., **West, C.**, Masiello, D., Link, S., & Landes, C. Coupled dipole modeling and experimental characterization of geometry-dependent trochoidal dichroism in nanorod trimers. ACS Photonics 8, 4 1159-1168 (2021). Ref. [11].

6. Pakeltis, G., Garfinkel, D., Rotunno, E., Khorassani, S., **West, C.**, Collette, R., Idrobo, J., Masiello, D., & Rack, P. High spatial and energy resolution electron energy loss spectroscopy of the magnetic and electric excitations in plasmonic nanorod oligomers. Opt. Express, 29, 3 4461-4671 (2021). Ref. [12].

7. **West, C.**,* Olafsson, A.,* Pakeltis, G., Garfinkel, D., Rack, P., Masiello, D., Camden, J., & Idrobo, J. Plasmon hybridization in nanorhombus assemblies. J. Phys. Chem. C. 124, 49, 27009-27016 (2020). Ref. [13].

8. Bhattacharjee, U.,* **West, C.**,* Jebeli, S.,* Goldwyn, H., Kong, X., Hu, Z., Beutler, E., Chang, W., Willets, K., Link, S. & Masiello, D. Active Far-Field Control of the Thermal Near-Field via Plasmon Hybridization. ACS Nano 13, 8, 9655-9663 (2019). Ref. [14].

9. Cheng, X.,* Anthony, T.,* **West, C.**, Hu, Z., Sundaresan, V., McLeod, A., Masiello, D. & Willets, K. Plasmon heating promotes ligand reorganization on single gold nanorods. J. Phys. Chem. Lett. 10, 6, 1394-1401 (2019). Ref. [15].

10. Pakeltis, G., Hu, Z.,* Nixon, A.,* Mutunga, E., Anyanwu, C., **West, C.**, Idrobo, J., Masiello, D., Fowlkes, J. & Rack, P. Focused Electron Beam Induced Deposition Synthesis of 3D Photonic and Magnetic Nanoresonators. ACS Appl. Nano Mater. 2, 12, 8075-8082 (2019). Ref. [16].

11. Cherqui, C., Wu, Y.,* Li, G.,* Quillin, S.,* Busche, J., Thakkar, N., **West, C.**, Montoni, N., Rack, P., Camden, J. & Masiello, D. STEM/EELS Imaging of Magnetic Hybridization in Symmetric and Symmetry-Broken Plasmon Oligomer Dimers and All-Magnetic Fano Interference. Nano Lett. 16, 6668-6676 (2016). Ref. [17].

* indicates co-first authorship

The remainder of this dissertation is organized in the following way. Ch 2 goes into further detail of the LSP and includes multiple analytic and numeric models which describe the LSP's electromagnetic and thermal properties. This ends the introduction presented in Part I. Part II includes three manuscripts which use photothermal imaging as a tool to understand the plasmonic properties of single and coupled gold nanoparticles. Ch. 3 and

Ch. 4 are reproductions of Refs. [14] and [10]. Both works use photothermal imaging to identify nanoscale temperature gradients in hybridized plasmonic nanoparticle systems. Ch. 5 is an unpublished manuscript which presents a novel model of the photothermal imaging experiment which describes the properties of experiment on large nanoparticles. Part III contains one publication [13] in Ch. 6 which uses a coupled harmonic oscillator model to interpret EEL line spectra and spectrum images of hybridized nanorhombuses. Finally, Part IV is a slight departure from the previous chapters in that it contains Ch. 7 which is an unpublished manuscript in the field of chemistry education. This chapter reports the results of a study I conducted on the impact a nanoscience summer camp (which I designed and taught) had on middle to high school students. The publications which I could not include as chapters can be found on my Google Scholar page. Some of the accompanying codes discussed in this dissertation can be found on my Github profile.

Chapter 2

LOCALIZED SURFACE PLASMON RESONANCES

The macroscopic Maxwell equations are an appropriate starting point for understanding light-matter interactions at the nanoscale.[1] The electric **E** and magnetic **B** fields sourced by a charge density ρ and current density **J** may be solved for (in Gaussian units and $\mu = 1$) according to

$$\begin{aligned} \boldsymbol{\nabla} \cdot \epsilon \mathbf{E} &= 4\pi\rho & \boldsymbol{\nabla} \times \mathbf{B} &= \frac{4\pi}{c}\mathbf{J} + \frac{\epsilon}{c}\frac{\partial \mathbf{E}}{\partial t} \\ \boldsymbol{\nabla} \cdot \mathbf{B} &= 0 & \boldsymbol{\nabla} \times \mathbf{E} &+ \frac{1}{c}\frac{\partial \mathbf{B}}{\partial t} = 0. \end{aligned} \tag{2.1}$$

Notably different compared to the microscopic Maxwell equations is the introduction of the dielectric function, $\epsilon = \epsilon(\omega)$. $\epsilon(\omega)$ is a complex quantity, often frequency dependent, which is a measure of the electric polarization of a material. It's imaginary part indicates the absorptive properties of the material. Interpreting the dielectric function of metals and their background environments is the first step towards describing and understanding the properties LSPs.

2.1 The Dielectric Function of Metals

The ratio $\left|\mathrm{Im}[\epsilon(\omega)]/\mathrm{Re}[\epsilon(\omega)]\right|$ of a material may be used to suggest its electronic properties. This quantity is referred to as the plasmon quality factor [19] and may be used to approximate whether a material may support plasmonic excitations. For example, when the ratio is $<< 1$, the material is a good dielectric and the lack of mobility of the electrons will restrict its ability to support LSPs. Alternatively, when the ratio is $>> 1$, the material is

[1] The procedure for converting the microscopic Maxwell equations to the macroscopic equations can be found in §4.3 in Ref. [18].

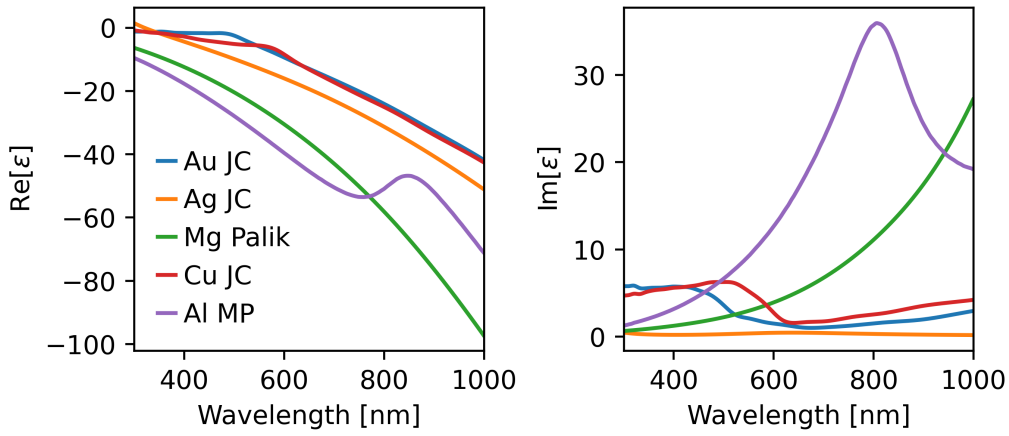

Figure 2.1: Experimental data of the real and imaginary parts of the dielectric function of different metals at room temperature. The gold, silver, and copper data are from Ref. [20], the magnesium data is from Ref. [21], and the aluminum data is from Ref. [22]. The large, negative Re$[\epsilon(\omega)]$ values corresponds to materials with high electron mobility, i.e., easily polarized. The small, positive Im$[\epsilon(\omega)]$ values indicate the material has minimal energy loss from absorption. The peaks in aluminum (purple trace), gold (blue trace), and copper (red trace) are from interband transitions, which restrict opportunities for plasmonic excitations.

a conductor and may be a potential candidate for plasmonic applications. Fig. 2.1 shows the real and imaginary parts of $\epsilon(\omega)$ for different metals across optical wavelengths at room temperature. In general, Re$[\epsilon(\omega)]$ for the metals is large and negative (the negative sign indicates the abundance of free electrons), and Im$[\epsilon(\omega)]$ is small and positive. Gold, copper, and aluminum additionally experience increased Im$[\epsilon(\omega)]$ at < 550 nm, < 600 nm, and ~ 880 nm, respectively, due to the onset of interband transitions.

Gold and silver are by far the most popular plasmonic materials due to their high electron mobility, low losses in the visible part of the spectrum, and their advantageous surface chemistry properties. Aluminum has also been shown to support LSPs [23], but it's interband transitions restrict plasmonic activity to the ultraviolet and part of the visible spectrum, which significantly limits it's popularity. While copper's interband transitions appear to be only slightly more limiting compared to gold, it's surface chemistry entirely prevents applicability. Magnesium [24], and other metals and alloys [19], are actively being explored

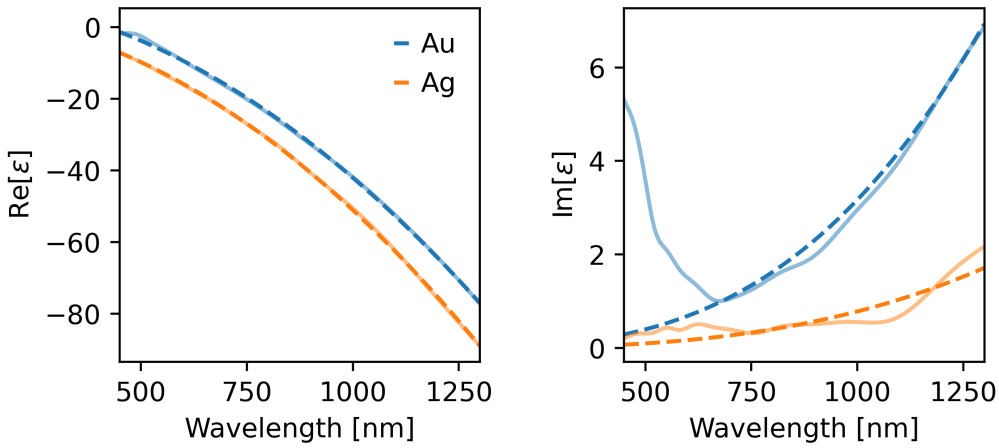

Figure 2.2: The Drude model, Eq. 2.2, fit to experimental data of the dielectric function for gold and silver. The dashed traces are the fit, the solid traces are the experimental data replot from Fig. 2.1.

to determine if other materials can outperform gold or silver. As yet, however, gold and silver remain to be the most well-studied materials. The remainder of this dissertation only includes studies on silver and gold plasmonic materials.

This frequency-dependant dielectric response (excluding interband transitions[2]) may be modeled by approximating the material as a free electron gas with electron density N embedded in a fixed positive ionic core background. Using $\epsilon\mathbf{E} = \mathbf{E} + 4\pi\mathbf{P}$, the macroscopic polarization $\mathbf{P}$ may be approximated as the number density of the electrons times a harmonically oscillating dipole moment, $\mathbf{p}$. The equation of motion for $\mathbf{p} = e\mathbf{x}$ driven by a harmonic force is $m\ddot{\mathbf{x}} + m\gamma\dot{\mathbf{x}} = e\mathbf{E}_0 e^{-i\omega t}$ where m is an effective mass, and γ is the damping from collisions. Assuming the steady-state, $\mathbf{x} = \mathbf{x}_0 e^{-i\omega t}$, and incorporating the influence of the positive ionic core leads to [26]:

$$\epsilon(\omega) = \epsilon_\infty - \frac{\omega_p^2}{\omega^2 + i\omega\gamma} \tag{2.2}$$

[2]To incorporate interband transitions, one or more Lorentz oscillators may be added to the model [25].

where ω_p is the plasma frequency, $\omega_p = \sqrt{\frac{4\pi N e^2}{m}}$. Eq. 2.2 is the Drude model and it describes the response of the electrons to an applied electric field in the absence of boundaries or surfaces. Fig. 2.1 shows the Drude model fit to a subset of the data from Fig. 2.1. The model accurately fits Re[$\epsilon(\omega)$], and as expected does not capture the interband transitions in Im[ϵ] which begin in gold at the lower wavelengths. This model is widely used to gain intuition about the plasmonic nature of materials.

2.2 A Sphere in the Presence of a Static Field

The dielectric function $\epsilon(\omega)$ is a macroscopic quantity which describes a material's bulk response to light; it does not contain any information about the size or shape of the material. A good starting place to model these effects is to solve for the response of a sphere in the presence of a static electric field.

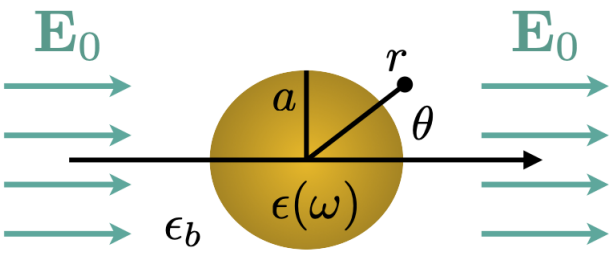

Figure 2.3: Sphere of radius a in the presence of a static field $\mathbf{E}_0$. The field excites a static dipole at the center of the sphere with polarizability α equal to the Clausius–Mossotti.

Consider a sphere of radius a and dielectric function $\epsilon(\omega)$ embedded in a background ϵ_b and driven with a static field $\mathbf{E}_0$, as shown in Fig. 2.2. When illuminated, the free electrons in the sphere will be displaced from their ionic background. The displaced charge will produce an overall dipole moment, $\mathbf{p}$ at the center of the sphere. The resulting electric field outside of the sphere will be the superposition of the incident field $\mathbf{E}_0$ and the field scattered by

the dipole $\mathbf{E}_{\text{dip}}$. The form of these fields are derived by solving the Laplace equation[3] and matching the boundary conditions at the surface of the sphere. Given the axial symmetry, solutions will take the form [18]

$$\begin{aligned}\Phi_{\text{in}} &= \sum_{l=0}^{\infty} A_l r^l P_l(\cos\theta) \\ \Phi_{\text{out}} &= \sum_{l=0}^{\infty} (B_l r^l + C_l r^{-(l+1)}) P_l(\cos\theta).\end{aligned} \tag{2.3}$$

In the far-field ($r = \infty$), $\Phi \to -E_0 z$. The boundary conditions are:

$$\begin{aligned}-\frac{1}{a}\frac{\partial \Phi_{\text{in}}}{\partial \theta}\Big|_{r=a} &= -\frac{1}{a}\frac{\partial \Phi_{\text{out}}}{\partial \theta}\Big|_{r=a} \\ -\epsilon\frac{\partial \Phi_{\text{in}}}{\partial r}\Big|_{r=a} &= -\epsilon_b\frac{\partial \Phi_{\text{out}}}{\partial r}\Big|_{r=a}.\end{aligned} \tag{2.4}$$

Using the above expressions, the coefficients A_l, B_l, and C_l are determined. This leads to

$$\begin{aligned}\Phi_{\text{in}} &= -\Big(\frac{3\epsilon_b}{\epsilon + 2\epsilon_b}\Big) E_0 r\cos\theta \\ \Phi_{\text{out}} &= -E_0 r\cos\theta + \Big(\frac{\epsilon - \epsilon_b}{\epsilon + 2\epsilon_b}\Big) E_0 \frac{a^3}{r^2}\cos\theta.\end{aligned} \tag{2.5}$$

The first term in Φ_{out} is from the incident field, and the second term is that due to the presence of a dipole at the center of the sphere. Using the form for the potential of an ideal dipole, the dipole moment $\mathbf{p}$ may be defined as:

$$\mathbf{p} = \epsilon_b a^3 \frac{\epsilon - \epsilon_b}{\epsilon + 2\epsilon_b}\mathbf{E}_0 \equiv \alpha \mathbf{E}_0 \tag{2.6}$$

where α is the Clausius–Mossotti polarizability.[4] Taking the gradient of Eq. 2.5 gives the

---

[3]Gauss's law in the absence of charge, and $\mathbf{E} = -\boldsymbol{\nabla}\Phi$ gives the Laplace equation: $\nabla^2\Phi = 0$

[4]There are different ways of defining the polarizability in Eq. 2.6. Some define the dipole moment as $\mathbf{p} = \epsilon_b \alpha \mathbf{E}_0$ and α does not have the extra factor of ϵ_b [27]. In this dissertation, α is defined as stated in Eq. 2.6.

electric field scattered by a dipole (without the incident field) to be:

$$\mathbf{E}_{\text{dip}} = [3\mathbf{r}(\mathbf{r}\cdot\mathbf{p}) - \mathbf{p}]\frac{1}{r^3} \tag{2.7}$$

This is the electric near-field produced by a static dipole. Eqs. 2.6 and 2.7 are appropriate starting points for developing models of plasmonic systems. When the nanoparticles are small ($\sim$ 5 nm), modeling the response of their electrons as instantaneous and using these static expressions is a very accurate approximation. This is referred to as the quasistatic limit.

2.3 A Sphere Driven by an Oscillating Field

Now consider what happens when the incident field $\mathbf{E}_0$ is turned off. The positive ionic background will pull the displaced electrons back towards their equilibrium positions. The accelerating electrons will overshoot these positions, and the electrons will continue to oscillate in this manner until all energy is lost. In the presence of an oscillating field, this electronic oscillation may be driven resonantly. This resonantly driven collective oscillation of electrons is referred to as a localized surface plasmon resonance. To lowest order, this process may be interpreted as an oscillating dipole, as depicted in Fig. 2.3.

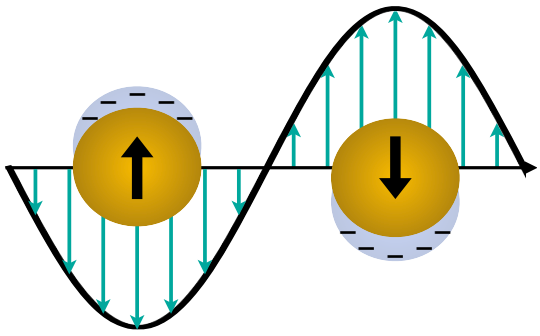

Figure 2.4: An oscillating electric field collectively drives the conduction band electrons in a sphere. This phenomena is known as a localized surface plasmon resonance.

The solution to the electric fields produced during this process is a much more complicated derivation compared to the static case. It involves solving Maxwell's equations by expanding the fields into vector spherical harmonics. A careful accounting of this procedure is done in § 4.1-4.4 of Ref. [27]. The final expressions of the fields will not be included herein because due to their complexity, no intuition is gained by simply looking at the expressions. Less complicated, though equally inscrutable by inspection, are the expressions for the cross-sections. Because these quantities will be referred to with more frequency, the extinction σ_{ext}, scattering σ_{sca}, and absorption σ_{abs} cross sections are included here for a reference:

$$\begin{aligned}
\sigma_{\text{ext}} &= \frac{2\pi}{k^2}\sum_{n=1}^{\infty}(2n+1)\text{Re}[a_n + b_n] \\
\sigma_{\text{sca}} &= \frac{2\pi}{k^2}\sum_{n=1}^{\infty}(2n+1)(|a_n|^2 + |b_n|^2) \\
\sigma_{\text{abs}} &= \sigma_{\text{ext}} - \sigma_{\text{sca}}
\end{aligned} \tag{2.8}$$

where a_n and b_n are the Mie coefficients:

$$\begin{aligned}
a_n &= \frac{m\psi_n(mx)\psi_n^{'}(x) - \psi_n(x)\psi_n^{'}(mx)}{m\psi_n(mx)\xi_n^{'}(x) - \xi_n(x)\psi_n^{'}(mx)} \\
b_n &= \frac{\psi_n(mx)\psi_n^{'}(x) - m\psi_n(x)\psi_n^{'}(mx)}{\psi_n(mx)\xi_n^{'}(x) - m\xi_n(x)\psi_n^{'}(mx)}
\end{aligned} \tag{2.9}$$

and $\psi_n(\rho) = \rho j_n(\rho), \xi_n = \rho h_n^{(1)}(\rho)$ are the Riccati-Bessel functions, $j_n(\rho)$ are the spherical Bessel functions, and $h_n^{(1)}(\rho)$ are the spherical Hankel functions. These solutions are powerful because they are exact for spherical particles, and they can be evaluated numerically with minimal computational resources. However, they cannot be used to describe coupled nanoparticles, or non-spherical nanoparticles. Further, physical intuition and visualization of these quantities cannot be done due to their complexity. For these reasons, different analytic models and computational frameworks have been developed which provide meaningful intuition and quantitative solutions to more sophisticated plasmonic systems.

2.4 Models of Localized Surface Plasmons

One of the most common strategies for modeling the fields and cross sections produced by LSPs is by only considering the lowest order ($n = 1$), dipolar response of the LSP. Modeling LSPs in this limit simplifies the analytics significantly, and presents a very flexible and fast numerical approach to study arbitrarily shaped LSP systems. These models are often referred to the discrete dipole or coupled dipole approximations. There are many other computational procedures which may be used to solve for the fields and cross sections of non-spherical systems with multiple nanoparticles which do not rely on the discrete dipole approximation. For a discussion of other softwares, see Ref. [28].

The following subsections overview two separate, yet closely related approaches for approximating the plasmonic response of one or multiple point dipoles. The first model, often referred to as the coupled dipole or discrete dipole approximation, models the fields and cross sections of the LSP as those of a radiating dipole. The second model uses harmonic oscillator equations of motion which approximate the dipole radiation as a dipole oscillator. Both models account for single and coupled / hybridized nanoparticle systems.

2.4.1 Modeling LSPs as Radiating Point Dipoles

In this model, often referred to as the coupled dipole approach, the sphere in Fig. 2.3 is replaced by an oscillating (radiating) point dipole. The electric field scattered by this dipole, derived in § 9.2 of Ref. [18], is

$$\mathbf{E}_{\text{dip}} = k^3 \left(\frac{3\hat{\mathbf{r}}\hat{\mathbf{r}} - \mathbf{1}}{(kr)^3} - i\frac{3\hat{\mathbf{r}}\hat{\mathbf{r}} - \mathbf{1}}{(kr)^2} - \frac{\hat{\mathbf{r}}\hat{\mathbf{r}} - \mathbf{1}}{kr} \right) e^{ikr} \cdot \mathbf{p}. \tag{2.10}$$

Notice that for small kr, the above expression reduces to the static field, Eq. 2.7. The three terms in Eq. 2.10 are referred to as the near-field, intermediate-field, and far-field ($1/(kr)^3, 1/(kr)^2$ and $1/(kr)$, respectively). It is therefore straightforward from here to cal-

culate the total scattering cross-section. In general, the cross section is defined as:

$$\sigma_i = \frac{\langle P_i \rangle}{I_0} \tag{2.11}$$

where i is either extinction, scattering, or absorption, and I_0 is the incident intensity, $I_0 = cn/8\pi|\mathbf{E}_0|^2)$. By evaluating Eq. 2.10 in the far field ($kr \to \infty$) and integrating the Poynting vector:

$$\langle P_{\text{sca}} \rangle = \int_A \langle \mathbf{S}_{\text{sca}} \rangle \cdot \hat{\mathbf{r}} dA \tag{2.12}$$

where $\mathbf{S}_{\text{sca}} = c/4\pi(\mathbf{E}_{\text{sca}} \times \mathbf{B}_{\text{sca}})$ and $dA = r^2 \sin\theta d\theta d\phi$. Substituting in $\mathbf{p}(\omega) = \alpha(\omega)\mathbf{E}_0$ leads to:

$$\sigma_{\text{sca}}(\omega) = \frac{8\pi}{3}\Big(\frac{\omega}{c}\Big)^4 \big|\alpha(\omega)\big|^2. \tag{2.13}$$

The extinction cross-section is obtained using the Optical Theorem (derived in § 9.14 of Ref. [18]) which relates the total extinction to the forward scattering amplitude. Written in terms of the polarizability, the extinction cross section is:

$$\sigma_{\text{ext}}(\omega) = 4\pi\frac{\omega}{c}\text{Im}\big[\alpha(\omega)\big] \tag{2.14}$$

As in Eq. 2.8, the absorption cross section may be evaluated by taking the difference between σ_{ext} and σ_{sca}.

These expressions are only valid for a single point dipole. To model systems with multiple nanoparticles, these expressions need to be modified to account for multiple, coupled dipoles. In this case, the dipole moment of dipole i is not equal to $\alpha_i(\omega)\mathbf{E}_0$, but instead is the total field $\mathbf{E}_{\text{tot}}$ resulting from the incident field plus the fields scattered by all other N dipoles, . Using Eq. 2.10, the total dipole moment of dipole i is:

$$\mathbf{p}_i(\omega) = \alpha_i(\omega)\mathbf{E}_{\text{tot}} = \alpha_i(\omega)\Big(\mathbf{E}_0 + \sum_{j\neq i}^{N} \mathbf{G}_{ij}\mathbf{p}_j(\omega)\Big), \tag{2.15}$$

$\mathbf{G}_{ij}$ is the dipole-relay tensor:

$$\mathbf{G}_{ij} = k^3 \left(\frac{3\hat{\mathbf{r}}_{ij}\hat{\mathbf{r}}_{ij} - \mathbf{1}}{(kr_{ij})^3} - i\frac{3\hat{\mathbf{r}}_{ij}\hat{\mathbf{r}}_{ij} - \mathbf{1}}{(kr_{ij})^2} - \frac{\hat{\mathbf{r}}_{ij}\hat{\mathbf{r}}_{ij} - \mathbf{1}}{kr_{ij}} \right) e^{ikr_{ij}} \tag{2.16}$$

and r_{ij} is the distance between dipole i and dipole j. These are now coupled equations of motion, which may be rewritten as a matrix equation $\tilde{\mathbf{G}}\tilde{\mathbf{p}} = \tilde{\mathbf{E}}_0$. Therefore, solving for the total and per particle cross-sections (derived in Ref. [29] and restated here):

$$\sigma_{\text{ext}} = \sum_{j=1}^{N} \sigma_{\text{ext},j} = \frac{4\pi k}{|\mathbf{E}_0|^2} \sum_{j=1}^{N} \text{Im}\left[\mathbf{E}_{0,j}^* \cdot \mathbf{p}_j\right] \tag{2.17}$$

$$\sigma_{\text{abs}} = \sum_{j=1}^{N} \sigma_{\text{abs},j} = \frac{4\pi k}{|\mathbf{E}_0|^2} \sum_{j=1}^{N} \left(\text{Im}\left[\mathbf{p}_j \cdot (\alpha_j^{-1})^* \mathbf{p}_j^*\right] - \frac{2}{3}k^3 \mathbf{p}_j \cdot \mathbf{p}_j^* \right). \tag{2.18}$$

requires $\tilde{\mathbf{p}}$, which may be solved for by inverting $\tilde{\mathbf{G}}$. For simple systems, this can quickly be performed in a few lines of code. However, there are much more sophisticated implementations of this framework, including Bruce Draine's DDSCAT [29]. The former and the latter are used throughout this dissertation to approximate the absorptive and radiative properties of metallic nanoparticle systems.

2.4.2 Modeling LSPs as Coupled Harmonic Oscillators

This second dipole model approximates the radiating dipole using oscillator equations of motion. An explicit verification of this model is done in Appendix E. The equation of motion for a single driven and damped dipole oscillator is:

$$m\ddot{\mathbf{x}} + m\gamma_{\text{tot}}\dot{\mathbf{x}} + m\omega_0^2\mathbf{x} = \mathbf{F}_{\text{ext}} \tag{2.19}$$

where m is an effective mass, γ_{tot} is the total (radiative γ_{rad} and nonradiative γ_{nr}) damping experienced by the oscillator, ω_0 is the resonance frequency, and $\mathbf{x}$ the oscillator coordinate. In this model, the nonradiative damping represents the absorption by the LSP. The radiative

damping term is added in to account for the Abraham-Lorentz force. This is the reaction force which results from the emission of radiation by the oscillating (i.e. accelerating) charge. As derived in §17.2 of Ref. [18], $\mathbf{F}_{\text{rad}} = 2e^2/(3c^3)\,\dddot{\mathbf{x}} = -m\gamma_{\text{rad}}\dot{\mathbf{x}}$. Given a harmonic driving force, $\mathbf{F}_{\text{ext}} = eE_0e^{-i\omega t}\hat{\mathbf{x}}$, the steady-state solution to Eq. 2.19 is $\mathbf{x}(t) = x(\omega)e^{-i\omega t}\hat{\mathbf{x}}$ where

$$x(\omega) = \frac{eE_0/m}{-\omega^2 - i\omega\gamma_{\text{tot}} + \omega_0^2}. \tag{2.20}$$

Using $\mathbf{p}(\omega) = e\mathbf{x}(\omega) = \alpha(\omega)\mathbf{E}_{\text{inc}}$, the polarizability of the dipole oscillator is

$$\alpha(\omega) = \frac{e^2/m}{-\omega^2 - i\omega\gamma_{\text{tot}} + \omega_0^2}. \tag{2.21}$$

This polarizability may be used to derive the cross sections for the dipole harmonic oscillator, again using Eq. 2.11. In this case, the powers may be calculated using:

$$\langle P_i \rangle = \frac{1}{\tau}\int_0^\tau \mathbf{F}_i \cdot \dot{\mathbf{x}}dt \tag{2.22}$$

with $\mathbf{F}_{\text{ext}} = e\mathbf{E}_{\text{inc}}$, $\mathbf{F}_{\text{abs}} = -m\gamma_{\text{nr}}\dot{\mathbf{x}}$, and $\mathbf{F}_{\text{sca}} = -m\gamma_{\text{rad}}\dot{\mathbf{x}}$. Evaluating the scattering and extinction integrals exactly returns Eqs. 2.14 and 2.13. This approach, as well as a method for deriving these cross-sections for two coupled oscillators is detailed in Ref. [30].

Additionally, the oscillator model may be used to calculate the normal modes of a system of coupled nanoparticles. This framework is based on Refs. [31, 32]. The equation of motion for the i^{th} oscillator (oscillator coordinate $\mathbf{x}_i = x_i\hat{\mathbf{e}}_i$) coupled to N other oscillators is

$$m_i\ddot{x}_i + m_i\gamma_i\dot{x}_i + m_i\omega_{0i}^2x_i - \sum_{j\neq i}^{N} g_{ij}x_j = 0 \tag{2.23}$$

where the coupling between the ith and jth oscillators, g_{ij}, is defined using the dipole-relay

tensor (Eq. 2.16):

$$\begin{aligned} g_{ij} &= e^2 \hat{\mathbf{x}}_i \cdot \mathbf{E}_j(\mathbf{r}_i) \\ &= e^2 \hat{\mathbf{x}}_i \cdot \Big[\frac{3\hat{\mathbf{n}}_{ij}\hat{\mathbf{n}}_{ij} - \mathbf{1}}{r_{ij}^3} - k\frac{3\hat{\mathbf{n}}_{ij}\hat{\mathbf{n}}_{ij} - \mathbf{1}}{r_{ij}^2} - k^2 \frac{\hat{\mathbf{n}}_{ij}\hat{\mathbf{n}}_{ij} - \mathbf{1}}{r_{ij}} \Big] \cdot \hat{\mathbf{x}}_j e^{ir_{ij}k} \end{aligned} \tag{2.24}$$

There are multiple choices for defining the effective mass, m_i. It may be related to the Clausius-Mossotti polarizability and Eq. 2.21. It can also be fit to experimental or simulated spectra. For other models for m, see Appendix A. In this model, each oscillator corresponds to a 1D oscillating dipole, i.e. up to three oscillators may be assigned per particle. Taking the steady-state approximation yields:

$$(-\omega^2 - i\gamma_i\omega + \omega_{0i}^2)x_{i0} - \sum_{j\neq i}^{N} \frac{g_{ij}}{m_i} x_{j0} = 0. \tag{2.25}$$

where x_{0i} is the amplitude of oscillation for each dipole and is defined by $\mathbf{x}_i = x_{i0}e^{-i\omega t}\hat{\mathbf{e}}_i$. Adding $\omega^2 x_{i0}$ to both sides of the equation returns

$$\begin{bmatrix} -i\gamma_1\omega + \omega_{01}^2 & -g_{12}/m_1 & \dots & -g_{1N}/m_1 \\ -g_{21}/m_2 & -i\gamma_2\omega + \omega_{02}^2 & \dots & -g_{2N}/m_2 \\ \vdots & \vdots & \dots & \vdots \\ -g_{N1}/m_N & -g_{N2}/m_N & \dots & -i\gamma_N\omega + \omega_{0N}^2 \end{bmatrix} \begin{bmatrix} x_{01} \\ x_{02} \\ \vdots \\ x_{0N} \end{bmatrix} = \omega^2 \begin{bmatrix} x_{01} \\ x_{02} \\ \vdots \\ x_{0N} \end{bmatrix}$$

This is approximately an eigenvalue equation $\mathbf{A}(\omega)\mathbf{x} = \omega^2\mathbf{x}$ with the exception that the matrix $\mathbf{A}(\omega)$ is dependent on the square root of the eigenvalue. In the quasistatic limit, $\mathbf{A}$ does not depend on ω, and one may solve for the exact normal modes of the system. However the above equation must be solved numerically when the damping and / or the full dipole-relay tensor are included.

2.5 Nanoscale Heating from LSP Absorption

LSP absorption induces local temperature increases. The dipole models discussed in the prior sections may be used to approximate the joint optical, and resulting thermal processes. For nanofabricated gold nanoparticles in non-absorbing media, the primary heat transfer mechanism is conduction. The time-dependent heat diffusion equation dictates the temperature increase as a result of conduction. To derive this expression, consider a heat source which generates a heat power density q embedded in an infinite background medium. Due to conservation of energy, the rate of change of the heat energy in the system must be equal to the energy generated by the heat source per unit time minus the energy leaving the system through the surface of the sphere per unit time:

$$\frac{\partial}{\partial t}\int_V dV\, c_p \rho T = -\int_S dS \mathbf{J}\cdot\hat{\mathbf{n}} + \int_V q dV \tag{2.26}$$

where c_p is the specific heat capacity $\left[\frac{\mathrm{J}}{\mathrm{kg\ K}}\right]$, ρ is the mass density $\left[\frac{\mathrm{kg}}{\mathrm{m}^3}\right]$, and $\mathbf{J}$ is the heat flux $\left[\frac{\mathrm{J}}{\mathrm{s\ m}^2}\right]$. The surface integral may be turned into a volume integral using the divergence theorem. Lastly, the flux will produce a thermal gradient according to Fourier's Law:

$$\mathbf{J}(\mathbf{x},t) = -\kappa(\mathbf{x})\boldsymbol{\nabla} T(\mathbf{x},t). \tag{2.27}$$

Given that each term is now integrated over the same volume, V, and that the equality must hold true over all space, the volume integral may be dropped, resulting in the well-known heat diffusion equation:

$$c_p\rho\ \frac{\partial T(\mathbf{x},t)}{\partial t} = \boldsymbol{\nabla}\cdot[\kappa(\mathbf{x})\boldsymbol{\nabla} T(\mathbf{x},t)] + q(\mathbf{x},t) \tag{2.28}$$

There are a limited number of geometries wherein the above inhomogeneous differential equation has an exact solution. A much simpler equation to solve is the time-independent,

steady-state solution. In the steady-state limit ($\partial T/\partial t = 0$), Eq. 2.28 reduces to:

$$-\boldsymbol{\nabla} \cdot [\kappa(\mathbf{x})\boldsymbol{\nabla} T(\mathbf{x}, t)] = q(\mathbf{x}, t). \tag{2.29}$$

This may be recognized as equivalent to the Poisson equation. As such, geometries which have analytic solutions to the Poisson equation will also have analytic steady-state temperature solutions. It follows, then, that given the numerous computational approaches to solving Maxwell's equations, there should be a straightforward numerical procedure for solving for steady-state temperature distributions. Previous members of the Masiello group wrote a computational framework based on thermal discrete dipoles (t-DDA) [33]. I have extended this model to incorporate an infinite substrate without costing any additional computational cost. This was used to calculated temperatures in Ref. [15], and an explanation of the image dipole procedure used to implement the change is discussed in the Supplementary Information of the manuscript.

Part II

PHOTOTHERMAL IMAGING AS AN APPROACH TO OBSERVE NANOSCALE TEMPERATURE GRADIENTS

Part II of this dissertation covers three investigations which detail procedures for creating controllable, nanolocalized temperature gradients, and how to use photothermal microscopy / spectroscopy to observe them. These works are a result of a multi-discplenary collaboration among Prof. Stephan Link's group at Rice University, Prof. Katherine Willet's group at Temple University, and Prof. David Masiello's group at the University of Washington. Part II does not include a complete synopsis of all works resulting from this collaboration. I have, instead, elected to include the following three manuscripts I co-first authored. They include:

- Chapter 3: Bhattacharjee, U.,* **West, C.***, Jebeli, S.,* Goldwyn, H., Kong, X., Hu, Z., Beutler, E., Chang, W., Willets, K., Link, S. & Masiello, D. Active Far-Field Control of the Thermal Near-Field via Plasmon Hybridization. *ACS Nano* 13, 8, 9655-9663 (2019). Ref. [14]

- Chapter 4: Jebeli, S.,* **West, C.,*** Lee, S., Goldwyn, H., Bilchak, C., Fakhraai, Z., Willets, K., Link, S., & Masiello, D. Wavelength-dependent photothermal imaging probes nanoscale temperature differences among subdiffraction coupled plasmonic nanorods. *Nano Lett.* 21, 12, 5386-5393 (2021). Ref. [10]

- Chapter 5: **West, C.,*** Shooter, J.*, Lee, S., Jebeli, S., Willets, K., Link, S., & Masiello, D. Nonlinear Effects in Photothermal Microscopies of Strongly Scattering Plasmonic Nanoparticles. *In Preparation.*

* indicates co-first authorship

Chapter 3

ACTIVE FAR-FIELD CONTROL OF THE THERMAL NEAR-FIELD *VIA* PLASMON HYBRIDIZATION

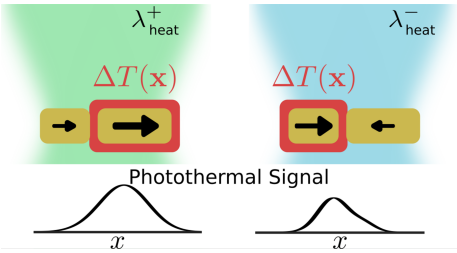

Reprinted with permission from:

Bhattacharjee, U.,* West, C.*, Jebeli, S.,* Goldwyn, H., Kong, X., Hu, Z., Beutler, E., Chang, W., Willets, K., Link, S. & Masiello, D. Active Far-Field Control of the Thermal Near-Field via Plasmon Hybridization. *ACS Nano* 13, 8, 9655-9663 (2019).

3.1 Abstract

The ability to control and manipulate temperature at nanoscale dimensions has the potential to impact applications including heat-assisted magnetic recording, photothermal therapies, and temperature-driven reactivity. One challenge with controlling temperature at nanometer dimensions is the need to mitigate heat diffusion, such that the temperature only changes in well-defined nanoscopic regions of the sample. Here we demonstrate the ability to use far-field laser excitation to actively shape the thermal near-field in individual gold nanorod heterodimers by resonantly pumping either the in-phase or out-of-phase hybridized dipole plasmon modes. Using single-particle photothermal heterodyne imaging,

we demonstrate localization bias in the photothermal intensity due to preferential heating of one of the rods within the pair. Theoretical modeling and numerical simulation make explicit how the resulting photothermal images encode wavelength-dependent temperature biases between each nanorod within a dimer, demonstrating the ability to actively manage the thermal near-field by simply tuning the color of incident light.

3.2 Introduction

The remarkable ability of noble metal nanoparticles to convert photon energy to thermal energy has had significant impact across fields as wide ranging as nanomedicine,[34, 35, 36] data storage,[37, 38, 39, 40] and clean energy.[41, 42, 43, 44] Underlying the conversion of light to heat is the nonradiative decay of the localized surface plasmon (LSP), a geometry-specific collective oscillation of the free electron gas within a noble metal nanostructure driven by electromagnetic radiation. Over the past decade significant advances in understanding the nonradiative decay of LSPs has led to the optimization of nanoparticle morphology[45] and assembly[46, 47] as to efficiently capture and convert incident light into heat at the nanoscale.

Modifying the temperature within and around plasmonic nanoparticles relies on managing the production of heat from the decay of LSPs. This process begins within femtoseconds of excitation when LSPs dephase into a nonthermal distribution of so-called "hot" electrons that subsequently relax over picoseconds by electron-electron and electron-phonon scattering.[48, 49] The resulting temperature is maximized when the particle is excited at the LSP absorption resonance, with a linear increase in temperature as a function of excitation power. If the nanoparticle is embedded in an environment with a low thermal conductivity, the temperature increase will be nearly uniform within the structure and will sharply fall off outside. Thus, highly localized thermal near fields can be generated at the surface of single plasmonic nanostructures by using far-field optical excitation.

By creating assemblies of nanoparticles, such as dimers and trimers, interparticle plasmon coupling can increase temperatures beyond those found in individual particles.[45, 47] The idea of using assemblies of plasmonic nanoparticles is well-established in surface-enhanced

spectroscopies, in which sizable electromagnetic field enhancements (e.g., "hot spots") can be generated in the gaps between adjacent nanoparticles.[50] However, the regions of strongest field enhancement in nanoparticle assemblies are not correlated with regions of high temperature,[51] as the thermal near field depends on both the power absorbed by each nanoparticle as well as the local landscape of thermal conductivities, which govern heat diffusion. In fact, the localization of the electric field between neighboring particles giving rise to the generation of spatially-localized electromagnetic "hot spots" is indicative of plasmon hybridization, which acts to delocalize absorption and optical heating. For example, Baffou and coworkers showed that while electromagnetic "hot spots" are localized in the gap of a nanosphere dimer upon excitation with light polarized along its long axis, the temperature rise due to photothermal heating is uniformly distributed across both nanospheres and is independent of excitation polarization.[52] Thus, while the electric field that penetrates neighboring particles can be exploited to increase the total heat generated[45], [53] (or, oppositely, to minimize unwanted heating in a multi-particle assembly),[54] it does not intuitively follow that localization of the thermal near field is achievable in these types of multi-particle assemblies. As a result, photothermal studies on nanoparticle assemblies typically focus on the regime where interparticle spacing is sufficiently large to prevent thermal diffusion between the particles[55] or to create assemblies that generate heat over microscale, rather than nanoscale, regions.[56, 57]

Recent theoretical work, however, has shown that clever design of the geometry of nanoparticle assemblies can create modified thermal profiles, such that heat can be preferentially deposited into specific particles within the assembly using far-field optical excitation.[33] This result suggests that it should be possible to use diffraction-limited far-field optical excitation to produce sub-diffraction-limited regions of enhanced thermal near fields within a nanoparticle assembly, thereby creating localized heating at nanoscale dimensions. Put another way, it should be possible to preferentially heat a single nanoparticle within a multi-particle assembly, even at interparticle spacings where plasmon hybridization occurs. However, no experimental validation of this prediction has yet been made.

In this paper, we demonstrate active light-driven control of the thermal near-field surrounding pairs of hybridized gold nanorods through a combination of single-particle photothermal heterodyne imaging,[58, 59, 60, 61, 8] together with coupled optical and heat diffusion modeling of the photothermal signal. By optically pumping either the bonding (λ_+) or antibonding (λ_-) dipole LSP resonances of nanofabricated nanorod heterodimers of varying interparticle spacing, we observe spatially asymmetric photothermal images that we correlate to modified local temperature distributions within each individual hybridized nanorod pair. The temperature profiles can be modified by tuning the excitation wavelength, polarization, and position of the excitation field, allowing us to control the thermal near field using only far-field excitation. Note that unlike in our previous theoretical work where we exploited near-field interferences between multiple normal modes to localize temperature increases,[33] here we bias the temperature between monomers within a single dimer normal mode based only upon the differing optical and thermal polarizabilities of each monomer within the hybridized dimer. Our results establish a strategy for the design of a class of thermal metamaterials capable of controllably directing heat power to precise nanoscopic regions of space, thereby producing thermal profiles of arbitrary shape that depend only upon parameters of the pump laser.[62]

3.3 Results & Discussion

To understand the design challenges introduced by LSP coupling, it is instructive to model the gold nanorod heterodimers as pairs of coupled dipoles. At close proximity the two independent plasmon dipoles, represented by the generalized coordinates Q_1 and Q_2, hybridize[63, 31, 64] into the bonding and antibonding normal mode pair

$$\begin{aligned} Q_+ &= \left(\frac{m_1}{m_2}\right)^{1/4} \cos\theta Q_1 + \left(\frac{m_2}{m_1}\right)^{1/4} \sin\theta Q_2 \\ Q_- &= -\left(\frac{m_1}{m_2}\right)^{1/4} \sin\theta Q_1 + \left(\frac{m_2}{m_1}\right)^{1/4} \cos\theta Q_2 \end{aligned} \tag{3.1}$$

with effective mass, $m_j (j = 1, 2)$ inversely proportional to the polarizability of the jth LSP and rotation angle $\theta = \frac{1}{2}\tan^{-1}\left(\frac{2g}{\sqrt{m_1 m_2}(\omega_1^2 - \omega_2^2)}\right)$ dictating the degree of mode mixing between isolated nanorod monomers with dipole-dipole coupling strength g and detuning $\omega_1^2 - \omega_2^2$. As shown below, asymmetrically increasing the temperature in one of the nanorods relative to the other will require that the Q_1 (or Q_2) contribution is minimized in the hybridized $Q_{+,-}$ modes. This can be accomplished by tuning parameters such as relative nanorod length, material composition, interparticle separation, and angle of illumination.[45] In this paper, we fix the effective mass (or polarizability) ratio with 250 nm and 150 nm long gold nanorods while varying the coupling g by changing the interparticle spacing.

Figure 3.1 (a,c) presents single-particle extinction and absorption spectra of individual gold nanorods and individual gold nanorod heterodimers with interparticle gaps of 15 nm, 20 nm, and 100 nm. The absorption measurements were performed in a glycerol environment with the nanorods fabricated on a silica substrate, and the pump laser polarized along the heterodimer's long axis. As we are limited to wavelengths below 1000 nm for our current absorption spectroscopy setup,[65] extinction spectra collected in a normal incidence geometry on individual nanostructures complement the spectral characterization of these nanostructures.[66] Simulated absorption and extinction spectra are calculated in a glycerol background only as silica and glycerol have similar optical constants in the relevant visible and near infrared regimes. Simulated extinction and absorption spectra (Figure 3.1(b,d)) agree well with the experiments and allow for identification of the hybridized modes. The extinction spectra in Figure 3.1(a,b) show the hybridized bonding (+) and antibonding (-) modes of each heterodimer, as well as the peak LSP wavelengths of the isolated monomers. Reducing the gap size between the nanorods increases coupling and shifts the bonding resonance to longer wavelengths and higher amplitude. The antibonding mode decreases in amplitude as coupling increases, and slightly red shifts due to competition between mode splitting, radiation damping, and the presence of higher-order plasmon modes. Figure 3.1(c) shows the spectral decomposition of the photothermal signal (i.e., the absorption spectra) of the three nanorod heterodimers' antibonding modes; the bonding modes seen in the sim-

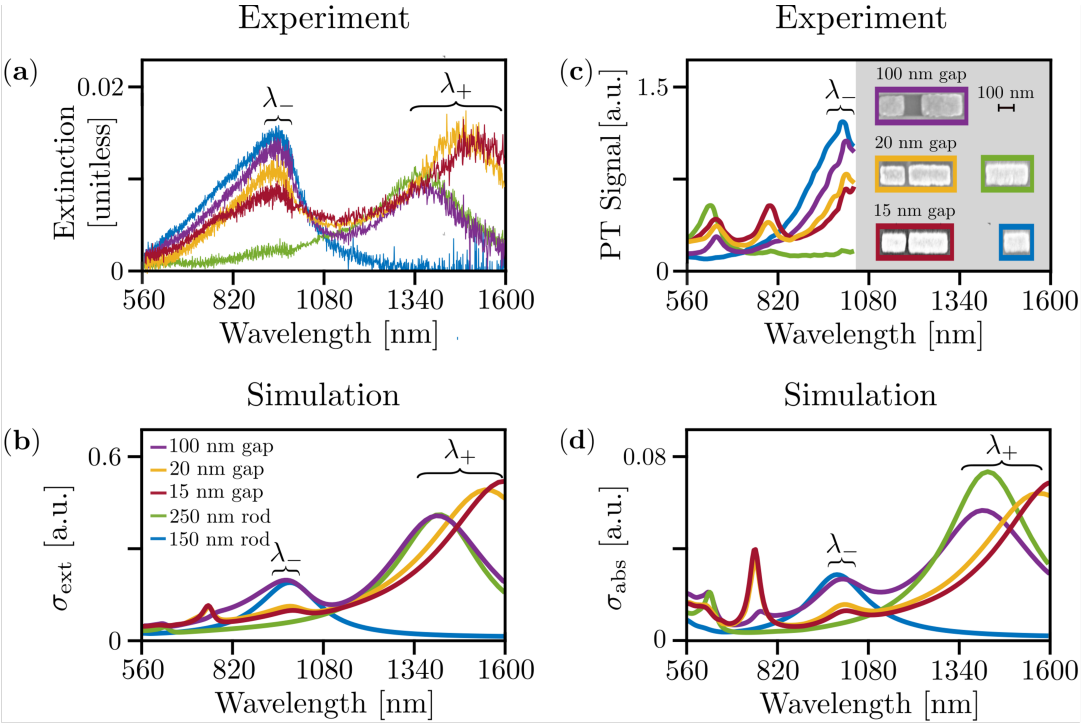

Figure 3.1: Experimental (a,c) and simulated (b,d) extinction and absorption spectra of individual gold nanorod heterodimers as a function of gap size. The dipole resonances of their basic nanorod components are indicated by the blue and green curves. Scanning electron microscope images of the nanoparticles are shown in (c) with the colored outlines indicating the corresponding spectra. All spectra are for light polarization parallel to the main heterodimer axis; perpendicular polarization is shown in Figure S1. Absorption spectra are limited to 1000 nm due to experimental limitations (see supporting information section 1). As nanoparticle separation decreases, the bonding (+) mode increases in amplitude while the antibonding (-) mode decreases, due to increased hybridization. The bonding mode redshifts with decreasing interparticle gap away from the uncoupled resonance of the 250 nm rod, while the antibonding mode remains almost constant with a small redshift. Worth noting is the correspondence of both modes of the 100 nm gap dimer with the uncoupled rod modes, indicating the weak electromagnetic coupling and weak hybridization across this largest gap heterodimer investigated. Slight differences in relative amplitudes between experiment and simulation are due to small variations in geometry between the nanorods produced by electron-beam lithography and the idealized nanorods used in simulation. Furthermore, the extinction spectra in (a) are stitched together from two detectors, potentially biasing the amplitude of the antibonding mode.

ulated absorption spectra (Figure 3.1(d)) are not experimentally characterized due to the aforementioned detection limitations for acquiring absorption spectra. The resonance peaks between 560-820 nm are higher order modes discussed in Figure S6.

Photothermal imaging of each individual heterodimer using excitation wavelengths that span across the dipolar bonding and antibonding modes was performed to map the spectral evolution of the thermal near field. Unlike the absorption spectrum (Figure 3.1(c)), where we are limited spectrally to 1000 nm, photothermal images can be measured up to 1550 nm (see supporting information section 1). In the following we will show that the spatial profile of each photothermal image is an indirect measure of the local temperature distribution created when exciting different hybridized plasmon modes and is dependent upon the specific imaging method.

Photothermal heterodyne imaging is a two-laser technique in which the first laser resonantly heats the system at a modulated frequency, thereby increasing the nanorod temperature and, in turn, that of its surrounding local environment. This temperature gain increases the refractive index of the surrounding environment according to

$$n(T(\mathbf{x})) \approx n(T_R) + \frac{dn}{dT}\Big|_{T=T_R}(T(\mathbf{x}) - T_R) \tag{3.2}$$

where $n(T(\mathbf{x}))$ is the temperature- and space-dependent refractive index and T_R is the initial ambient temperature before optical pumping. A second off-resonant probe beam incident on these regions of increased refractive index scatters differently from the unpumped room temperature system. The photothermal image is created by raster scanning the sample and recording the scattered probe intensity via lock-in detection. Although photothermal imaging is diffraction-limited, a two-beam imaging technique has an inherent resolution advantage and the nanorod heterodimers fabricated here are sufficiently large to make it possible to spatially resolve differences in the photothermal signal across each individual heterodimer (Figure S2). If the far field excitation source is able to differentially heat each nanorod within the heterodimer, then we expect a spatial asymmetry in the photothermal image due

to spatial variations in the temperature-dependent refractive index of the surroundings.

Indeed, Figure 3.2 shows different spatial profiles for the photothermal images of the three nanorod heterodimers over a range of pump wavelengths, spanning the dipolar bonding and antibonding mode resonances using a probe beam of 532 nm. Two-dimensional photothermal intensity images for each heterodimer at different pump wavelengths are shown together with one-dimensional line sections taken through the signal maximum. For all three heterodimers, the spatial bias of the photothermal signal intensity (and related temperature profile, as will be shown below) shifts from the 250 nm to the 150 nm nanorod as the excitation wavelength is tuned from the bonding to the antibonding LSP modes, respectively. This behavior is absent for a heating beam with polarization perpendicular to the nanorod main axis as mode selective excitation is no longer possible (Figure S3).

While not directly observable, thermal distributions of each heterodimer can be inferred from heat diffusion theory. Steady-state temperature profiles of the bonding and antibonding mode resonances are calculated by numerically solving the steady-state heat diffusion equation $-\boldsymbol{\nabla} \cdot [\kappa(\mathbf{x})(T\mathbf{x})] = Q(\mathbf{x})$ sourced by the heat power density $Q(\mathbf{x})$ absorbed from the pump laser, where $\kappa(\mathbf{x})$ and $T(\mathbf{x})$ are the space-dependent thermal conductivity and temperature. The calculation is performed using the thermal discrete-dipole approximation (T-DDA),[33] which generalizes the DDA[29, 67] concept by allowing each DDA target point to additionally be thermally conductive. In analogy to the familiar DDA, the target is discretized into a collection of thermally polarizable points that are each heated by absorption of light and come into self-consistency with all other points in accordance with Fourier's law of diffusion. Both the infinite background of glycerol and the silica substrate are included in the thermal calculations, the latter by exploiting an analogy to the image effect of electrostatics[18] (see supporting information section 2). Separate analysis of near-field thermal radiation as a heat transport mechanism shows minimal effects in this system in comparison to diffusion and is therefore omitted from the temperature calculations (see supporting information section 2). Additionally, due to the nanometer length scales of the heterodimer and surrounding glycerol, the characteristic velocity of the glycerol will be very

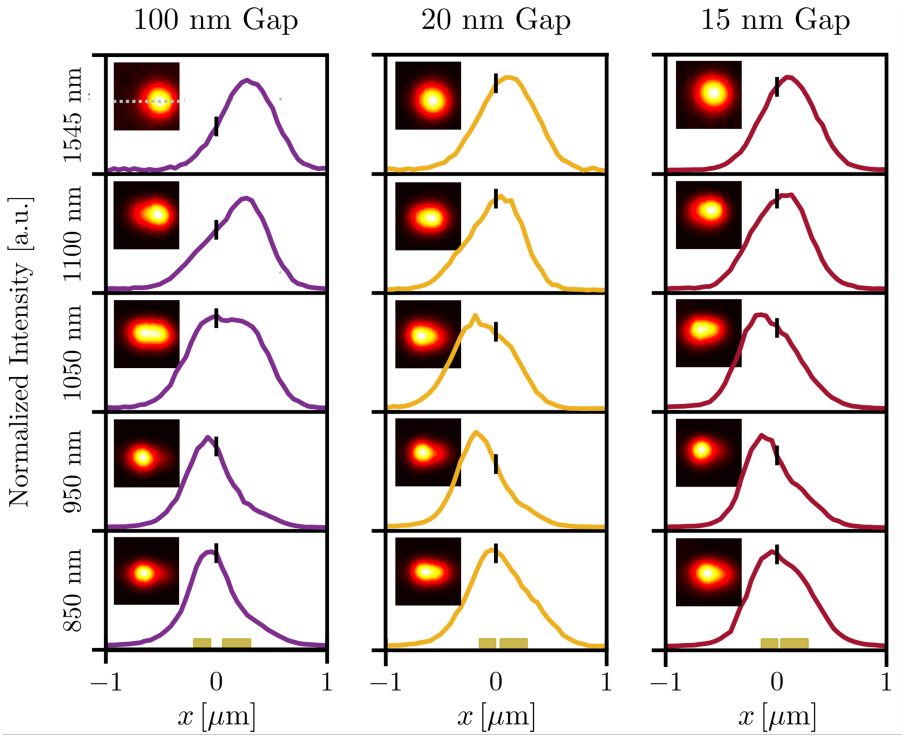

Figure 3.2: Photothermal images of three nanorod heterodimers of different gap size versus pump wavelength. The pump beam polarization is parallel to the nanorods' long axis, with the nanorods' orientation indicated by the gold bars in the bottom panels. As the wavelength is decreased the photothermal image maximum moves from the 250 nm nanorod (rightward biasing) to the 150 nm nanorod (leftward biasing). The one-dimensional line sections are the normalized photothermal signal intensity on the horizontal line going through the maximum of each image (dotted line in the first inset), clearly showing how the profile changes shape and position depending on coupling (i.e., gap size) and excitation wavelength. A black line is shown at $x = 0$ (center of nanoparticle gap) in each panel to guide in observing the transition from rightward to leftward biasing. The wavelengths between bonding and antibonding modes present a region that can be considered non-resonant for the excitation of the heterodimer modes. The response of higher order modes at shorter wavelengths is given in Figure S4. Note that we compare here the photothermal images taken at different wavelengths with their intensities normalized as we cannot compare the measured relative intensities directly without an independent standard. The standard used for the absorption spectra in Figure 3.1 was a 35 nm thin gold film that gave insufficient absorption beyond 1000 nm (see supporting information section 1). The spatial resolution is obtained by imaging the individual nanorods (Figure S2). It is 600 nm for the longest wavelength and 450 nm for all others as it is mainly determined by the 532 nm probe beam.

small, making heat transport via convection negligible in comparison to conduction.[68]

Figure 3.3 displays simulated temperature profiles of the three heterodimers as the Gaussian pump beam is raster scanned across the long axis of each heterodimer. The blue dot indicates the position of the center of the pump beam, where each new beam position excites a different temperature profile. At the bonding modes of all heterodimers, the temperatures is highest within the 250 nm rod, with the only difference between each beam position being a change in magnitude of the temperature difference between the 250 nm and 150 nm rod. This is consistent with the measured photothermal images in the first row of Figure 3.2 that display rightward biasing at the bonding modes. However at the antibonding modes for each heterodimer, the position of the Gaussian beam changes the magnitude and sign of the difference in temperature. When the beam is centered on the 250 nm nanorod in each of the three heterodimer gap sizes, the temperature on the 250 nm nanorod is slightly higher than the 150 nm nanorod. Yet, when the beam is centered on the 150 nm nanorod, that nanorod becomes hotter than the 250 nm nanorod. For the 100 nm gap heterodimer, the temperature difference between the two nanorods is greatest here, and in the 20 nm and 15 nm gap heterodimers the temperature magnitude is greatest, even though the differences in temperature between the nanorods are similar. By comparing the trends with decreasing gap size, it is clear that the differences in temperature between nanorods are decreasing, indicative of increased thermal coupling caused by the diminishing insulating material (i.e., glycerol) within the gap. This result elucidates the compromise between electromagnetically coupling the nanoparticles to drive stronger hybridization at the expense of heat diffusing between the particles causing the temperature to become more uniform across the heterodimer. Even so, it is apparent that hybridization enables the ability to tune the thermal profile within and around plasmonic nanoparticles in close proximity despite heat diffusion working in opposition.

To better understand the relationship between the experimental photothermal images and computed temperature profiles, we simulate the photothermal imaging process. As introduced in previous literature,[58, 59, 60, 61] the photothermal signal is determined by

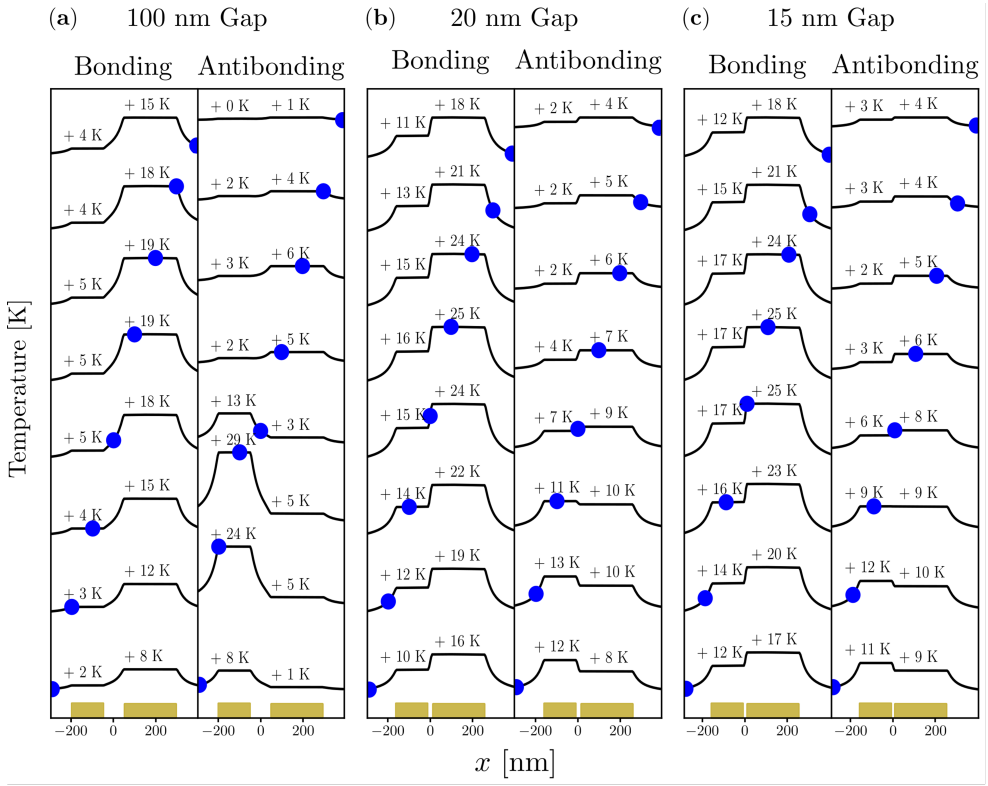

Figure 3.3: Simulated temperature profiles of the three nanorod heterodimers at their respective bonding and antibonding LSP resonances. The blue dots indicate the centroid of the Gaussian laser profile as the pump beam is raster scanned across the long axis of each heterodimer. The waist of the beam $w = 0.6\lambda/NA$ is chosen to model the experiment (λ is the bonding/antibonding wavelength, NA is the experimental numerical aperture) with values that range from $w \approx 480 - 830$ nm. As the beam is raster scanned across each heterodimer, different temperature profiles are created. At the bonding modes of all three gap sizes, the 250 nm rod is hotter than the 150 nm rod regardless of beam position. However, at the antibonding modes, the temperature difference between the two particles is dependent on beam position; the largest magnitude is achieved when the beam is centered on the 150 nm particle, while the sign of the difference changes when the beam is centered on the larger particle. These temperature profiles are used as input source for the simulated point spread functions in Figure 3.4.

subtracting the room temperature intensity (I^R, pump beam off) from the hot intensity (I^H, pump beam on), i.e., $I_{PT}(x) = I^H(x) - I^R(x)$ to construct simulated point spread functions (PSFs). While the experimental signal is extracted by modulating the pump beam, two separate scattering calculations are performed to simulate the same observable. In the first, the refractive indices of the metal are modified using the temperature profiles shown in Figure 3.3 based on the optical heat power absorbed by the rastered Gaussian pump laser using a temperature-dependent Drude model.[69] We then compute the scattering of a co-scanned Gaussian beam representing the probe beam through these heated points with thermally-modified refractive indices acting as a thermal lens. By collecting and integrating the forward scattered light at each beam position (x), we compute an observable proportional to the hot photothermal intensity, $I_H(x)$. The intensity of the probe field scattered at room temperature, $I_R(x)$, is calculated in the same manner but instead by using the room temperature values $n(\mathbf{x}, T) = n(\mathbf{x}, T_R)$ for all optical constants. The difference of these calculations represents the measured PSFs of the photothermal signal and can be compared to the experimental images and line sections shown in Figure 3.2.

Figure 3.4 displays the simulated photothermal PSFs of each nanorod heterodimer below the corresponding experimental data. Line sections of the PSFs along the symmetry axis of the heterodimers appear in black for all three gap sizes at both dipolar λ_+ and λ_- normal mode resonances. The blue and green curves display the corresponding signal for the isolated nanorods at the same wavelengths. The nanorod locations are represented by the rectangular gold bars with the gap centered at the origin. The isolated monomer PSFs are indicative of the spatial locations of those particles within the heterodimer, and thus comparing the heterodimer PSFs to those of the monomers quantifies the degree of asymmetry as a function of gap size at each hybrid LSP resonance.

Critical to the interpretation of the heterodimer PSF biasing in Figure 3.4 is an understanding of its relationship to local temperatures. The necessary connection can be elucidated through an idealized analytic model of two dipoles that are electromagnetically and thermally coupled in the near-field and that can scatter light to the far-field. As detailed in supporting

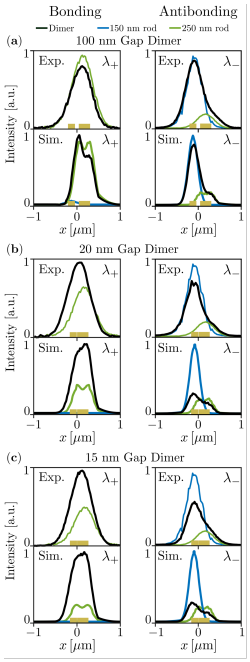

Figure 3.4: Excitation wavelength dependent biasing of the photothermal image. Experimental and simulated line sections of PSFs of the three nanorod heterodimers at each gap size are shown for excitation at the bonding λ_+ mode (1545 nm) and the antibonding λ_- mode (950 nm). Their respective isolated monomers are also given. Nanorod positions are indicated by the gold bars. Mapping of experimental PSFs and the actual nanostructure positions was achieved with fiduciary markers (Figure S5). Furthermore, the photothermal intensities are scaled to the measured signal allowing for a direct comparison of magnitudes. For all heterodimers, experimental and simulated PSF line sections indicate rightward biasing at the bonding λ_+ mode and leftward biasing at the antibonding λ_- mode. Additionally for the 20 nm and 15 nm gap PSFs, the magnitude of the heterodimer PSFs (black) are larger at the bonding mode compared to the isolated 250 nm nanorod (green), and, oppositely, the magnitude of the heterodimer at the antibonding mode is smaller than the isolated 150 nm nanorod (blue). The double lobed feature of the simulated 250 nm monomer PSF results from increased scattering at the nanorod ends and is not visible in the experiment due to resolution. Experimentally, no PSFs can be recorded for the isolated 150 nm nanorods at the bonding mode because the absorption is too weak (blue). Note that in experiment the excitation wavelengths are fixed and therefore a direct comparison of the PSF location and intensity between the different nanostructures is possible. Simulations model this scenario.

information section 3, the dependence of the photothermal images on temperature can be understood under the approximation that each nanorod embedded within its surrounding glycerol environment scatters light approximately as a polarizable point dipole, coupled to the neighboring nanorod dipole through near-field dipole-dipole interactions. The fields scattered by these effective dipoles at room and elevated temperatures are determined by their temperature dependent polarizabilities $\alpha_i(T) \approx \alpha_i^R + \frac{d\alpha_i}{dT_i}(T_i - T_R)$ expanded to first order in variation with temperature of the ith nanorod ($i = 1,\ 2$). Here, α_i^R is the room temperature polarizability and $T_i \equiv T(\mathbf{x}_i)$ is the temperature of the ith nanorod and the surrounding heated glycerol. Within this idealized model, the photothermal image can be understood as the superposition of two airy disk PSFs representing the near diffraction-limited image of each nanorod's scattered field. These scattered fields also interfere, effectively blurring the superposition of the two PSFs. As shown in supporting information section 3, by including both superposition and interference effects, the dependence of the photothermal image on the temperature of each nanorod can be written as

$$\begin{aligned}\frac{I^{PT}}{I_{inc}} = \frac{8\pi k^4}{3A_{PD}}\Bigg(&2\mathrm{Re}\Big[\alpha_1^{R*}\frac{d\alpha_1}{dT_1}\big|_{T_R}(T_1 - T_R)\Big] f_{PSF}(\mathbf{x} - \mathbf{x}_1) \\ &2\mathrm{Re}\Big[\alpha_2^{R*}\frac{d\alpha_2}{dT_2}\big|_{T_R}(T_2 - T_R)\Big] f_{PSF}(\mathbf{x} - \mathbf{x}_2) \\ &2\mathrm{Re}\Big[\alpha_2^{R*}\frac{d\alpha_1}{dT_1}\big|_{T_R}(T_1 - T_R) + \alpha_1^{R*}\frac{d\alpha_2}{dT_2}\big|_{T_R}(T_2 - T_R)\Big] f_{PSF}(\mathbf{x} - \mathbf{x}_1, \mathbf{x} - \mathbf{x}_2)\Bigg)\end{aligned} \tag{3.3}$$

assuming minimal coupling between the nanorods from the probe laser. In this expression, I_{inc} is the incident probe intensity and A_{PD} is the area of the photodetector. Each PSF (f_PSF) scales linearly with temperature (T_i), but also with the room temperature polarizability of the ith nanorod. The scaling of each PSF and interference PSF (f_IF) with temperature $\alpha_i^{R*}\frac{d\alpha_i}{dT_i}|_{T_R}$ differs between the two nanorods and complicates the relationship between local temperature and photothermal image magnitude. Also, because this image is

generated by rastering both the pump and probe lasers across positions $\mathbf{x}$, it is important to note that the nanorod temperatures $T_{1,2}$ are implicit functions of the beam position $\mathbf{x}$ as demonstrated in Figure 3.3. Nonetheless, it is evident that the photothermal image biases in the direction of increased temperature and increased polarizability, meaning that asymmetry in the PSF is positively correlated with nanoscale asymmetry in temperature and nanorod polarizability.

Equipped with the intuition gained from equation (3) to interpret the local temperature dependence of the photothermal PSFs, Figure 3.4 displays the experimental PSFs above those computed from the simulated temperatures in Figure 3.3. The bonding mode PSFs of the 100 nm, 20 nm, and 15 nm gap heterodimers in experiment and simulation exhibit strong localization to the longer nanorod, as seen by comparing the heterodimer PSFs (black) to the isolated 250 nm monomer PSFs (green.) The 100 nm, 20 nm, and 15 nm gap heterodimer PSFs at the antibonding wavelength are oppositely localized over the smaller 150 nm nanorod, yet retain noticeable shoulders over the 250 nm nanorod in both experiment and simulation. This lesser degree of photothermal localization compared to the bonding mode is due to non-negligible photothermal signal originating from the 250 nm nanorod even though it is minimally heated by excitation at the antibonding wavelength, as well as the smaller temperature differences between the nanorods compared to the large differences achieved at the bonding mode resonance.

3.4 Conclusion

Controlling the distribution of heat and temperature at nanoscale dimensions using far-field optical excitation is challenging due to the counteracting effects of the diffraction limit of light and the diffusion of heat. Here we have shown the surprising ability to overcome thermal diffusion and create nanolocalized distributions of increased temperature in hybridized plasmonic nanoparticle clusters that are actively tunable from the far-field simply by changing the wavelength of the pump field. Our approach relies upon asymmetries in the spatial distribution of in-phase and out-of-phase plasmonic normal modes in individual nanofabricated

gold nanorod heterodimers of varying inter-rod spacing. Using single-particle photothermal heterodyne imaging we observed spatial biasing in the photothermal PSFs measured at each normal mode resonance and correlate these biases to inhomogeneities of the thermal near-field using analytical models and numerical simulations of the coupled optical and thermal fields. Taken together this closely integrated experimental and theoretical work demonstrates the ability to actively manipulate the thermal near-field and points to future generalizations involving more complex nanoparticle clusters to create arbitrarily tunable thermal profiles below the diffraction limit. Even larger temperature biasing can be achieved for plane wave excitation where the illumination is larger than the coupled nanostructure as shown through simulations in Figure S8. This case will be the subject of future combined experimental and theoretical studies.

3.5 Methods

3.5.1 Experimental

In the photothermal heterodyne imaging measurements, the probe laser was a 532 nm diode laser (Coherent OBIS) and the pump laser (Fianium WhiteLase) wavelength was tuned from 500 nm - 1550 nm. The pump beam was modulated at a frequency of 30 kHz. The sample was placed in a confocal microscope with a 63x oil immersion objective with a NA = 0.7 to focus the laser beams onto the sample. A 50x air objective with a NA = 0.7 collected the scattered probe light in a transmission geometry. The signal generated by the scattered light was directed to a lock-in amplifier with an integration time of 30 ms and a sensitivity of 3 mV for all measurements. The pump power was 600 μW at 800 nm and the probe power was 1.1 mW. To obtain photothermal contrast images, the pump wavelength was held constant while the sample was moved using a piezo scanning stage.

3.5.2 Theoretical

The computational approach for obtaining confocal photothermal images used DDSCAT 7.3,[29] modified to account for a Gaussian beam excitation source. The calculations were performed on gold heterodimers using a temperature-dependent Drude model41 with 5 nm dipole spacing in a uniform infinite glycerol background (n = 1.473) at the wavelength corresponding to each normal mode. The resulting electric field and polarization information within the nanorods were used as inputs to a version of T-DDA[33] which includes a semi-infinite silica (κ =1.38 W/mK) substrate (see Supporting Information section 2.2). The temperatures of each nanorod were then used to modify the dielectric data of gold for a second scattering calculation, performed at an off-resonant probe wavelength of 615 nm. The total intensity of the forward scattered light from this second scattering calculation at a single Gaussian probe beam position, x_i, is $I_H(x_i)$. To obtain the entire photothermal signal, the room temperature intensity, $I_R(x_i)$, found by calculating the scattering from the room temperature nanorods at a probe wavelength of 615 nm, was subtracted from $I_H(x_i)$. Lastly, to obtain each position-dependent line-section, the entire procedure was carried out over a range of co-scanned excitation and probe beam positions that spanned the length of the dimer system.

3.6 Acknowledgments

This work was supported by the U.S. National Science Foundation under grant numbers NSF CHE-1727092 and CHE-1664684 (D.J.M.), CHE-1727122 (S.L.), CHE-1728340 (K.A.W.). S.L. also acknowledges support from the Robert A. Welch Foundation (grant C-1664). This work was facilitated through the use of advanced computational, storage, and networking infrastructure provided by the Hyak supercomputer system at the University of Washington.

Chapter 4

WAVELENGTHDEPENDENT PHOTOTHERMAL IMAGING PROBES NANOSCALE TEMPERATURE DIFFERENCES AMONG SUBDIFFRACTION COUPLED PLASMONIC NANORODS

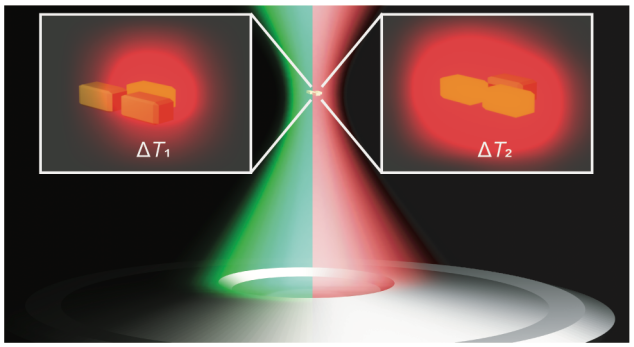

Reprinted with permission from:

Jebeli, S.,* West, C.,* Lee, S., Goldwyn, H., Bilchak, C., Fakhraai, Z., Willets, K., Link, S., & Masiello, D. Wavelength-dependent photothermal imaging probes nanoscale temperature differences among subdiffraction coupled plasmonic nanorods. *Nano Lett.* 21, 12, 5386-5393 (2021).

4.1 Abstract

Plasmonic structures confine electromagnetic energy at the nanoscale, resulting in local, inhomogeneous, controllable heating, but reading out the temperature using optical techniques poses a difficult challenge. Here, we report on the optical thermometry of individual

gold nanorod trimers that exhibit multiple wavelength-dependent plasmon modes resulting in measurably different local temperature distributions. Specifically, we demonstrate how photothermal microscopy encodes different wavelength-dependent temperature profiles in the asymmetry of the photothermal image point spread function. These asymmetries are interpreted through companion numerical simulations to reveal how thermal gradients within the trimer can be controlled by exciting its hybridized plasmon modes. We also find that plasmon modes that are optically dark can be excited by focused laser beam illumination, providing another route to modify thermal profiles beyond wide-field illumination. Taken together these findings demonstrate an all-optical thermometry technique to actively create and measure nanoscale thermal gradients below the diffraction limit.

4.2 Introduction

Harnessing the thermal response of optically excited noble metal nanoparticles has been used for a variety of different applications, including drug delivery,[70, 71, 72] photothermal therapies,[73, 74, 75] photocatalysis,[76, 77] heat generation from solar energy,[78, 79] heat-assisted magnetic recording,[80, 81, 82] and thermal manipulation of materials at the nanoscale.[83] In all of these applications, light interacts strongly with the nanoparticles and drives coherent charge oscillations known as localized surface plasmon (LSP) resonances. It is through the nonradiative decay of the LSP that the nanoparticle is heated, which in turn leads to temperature increases in the environment.[84, 85, 86] Measuring and understanding the induced nanoscale temperature gradients is critical for the optimization of many photothermal applications.[87, 88, 89, 90]

Current research in nanothermometry has focused on different methods to measure temperature at the nanoscale. For example, the ratio of Stokes to anti-Stokes photoluminescence spectra has been used to calculate nanoparticle temperatures; however, it requires the lattice and electron temperatures to be approximately the same to correctly interpret the results.[91, 92, 93] Electron energy-loss spectroscopy (EELS) uses phonon energy shifts combined with ratioing loss-to-gain signals to infer the lattice temperature of the material.[94, 95]

However, while EELS can map temperature changes at truly nanoscale dimension, it requires a high-fidelity electron microscope and ultrahigh vacuum conditions, which adds to the complexity of experiments.

Alternatively, photothermal microscopy is an optical, in situ method that relies on nanoparticle and local environment heating to collect signal.[96, 97, 98] This method uses two lasers: a heating laser tuned to excite the nanoparticle and induce nanoscale thermal gradients and a second laser to probe refractive-index changes in the system induced by these thermal modifications.[61] The pump beam is modulated by a low frequency signal from a function generator (100 kHz) and as a result the heat generation and temperature around the nanostructures are modulated at the same frequency. This approach results in a modulated refractive index change, which causes the intensity of the probe beam that reaches the detector to have an AC component on top of a DC signal. The AC part is detected using a lock-in amplifier and is proportional to the heat generated by the pump beam incident on the nanostructure. The probe wavelength can be chosen off-resonance to avoid melting the particles while having high power to increase the signal-to-noise ratio (SNR).[61, 99, 100] A previous demonstration of this method in individual plasmonic nanorod dimers showed that the centroid of the photothermal signal is biased toward the hotter nanorod within the hybridized dimer, indicating the sensitivity of the technique to spatially nonuniform thermal profiles.[14]

In this work, photothermal microscopy is performed on individual, asymmetric gold nanorod trimers and the resulting images are correlated with their wavelength-dependent nanoscale thermal profiles. The nanorod trimer structure is designed to host three unique nanoscale temperature distributions associated with its three hybrid LSP modes. In imaging these modes, we find that the full width at half maximum (fwhm) of the photothermal image in both x- and y-directions of the image plane (obtained by fitting a 2-dimensional Gaussian) varies with pump (heating beam) wavelength. We explain these trends through LSP mode analysis, coupled optical and heat diffusion simulations, and photothermal image modeling using a focused illumination source,[14, 31] revealing their origin in the asymmetric excita-

tion of the nanorod trimer's hybrid LSP modes and their associated thermal distributions. It is through this analysis of the ratio of x- and y-direction fwhm of the photothermal image that we uncover and herein report upon a new approach for all-optical thermometry at the nanoscale.

4.3 Results & Discussion

Figure 4.1a displays the gold nanorod trimer designed to produce wavelength-dependent, nanolocalized temperature distributions under steady-state optical excitation (see complete simulation details in section S1). The nanorod trimer's three hybrid LSP modes, labeled λ_1, λ_2, and λ_3, are illustrated in Figure 4.1a. The nanorods are each 80 nm long and 40 nm wide with a 20 nm separation, making the entire system (180 nm $\times$ 100 nm), well below the diffraction limit of the focused probe laser (360 nm). Each nanorod trimer is nanofabricated on a glass substrate and immersed in glycerol to provide a low thermally conductive environment for heat to diffuse. Nineteen such nanorod trimers, nanofabricated using electron beam lithography, are studied (see complete experimental details in section S2). Absorption and dark-field scattering spectra of all studied individual nanorod trimers are measured, each having the same general features as the blue traces shown in Figure 4.1b. The absorption spectra are obtained using a photothermal microscope and the scattering spectra are measured using a hyperspectral microscope.[101, 8] In both setups, the nanorod trimers are excited using a numerical aperture (NA) of 1.4 and the light is collected using a 0.7 NA objective after interacting with the structures. Simulated absorption and scattering cross sections resulting from a focused Gaussian beam excitation source to mimic the photothermal imaging experiments, using full-wave electromagnetic simulations in a modified discrete dipole approximation [29, 67] are shown in the orange traces in Figure 4.1b. The beam centroid lies at the center of the nanorod trimer and well approximates the experimental spectrum collected at the same point. The two resonances in the simulated absorption spectrum correspond to the hybrid LSP modes λ_1 and λ_2. These bright modes are indistinguishable in our measurements because of the broad line width of the laser (10 nm as

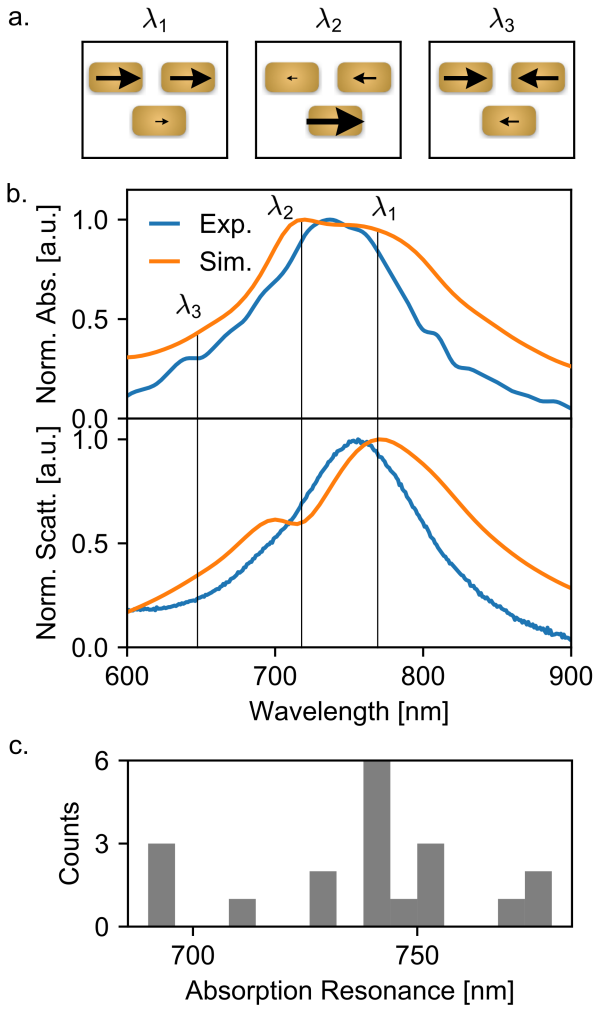

Figure 4.1: Absorption and scattering spectra of the individual, nanofabricated, and simulated nanorod trimer structures. (a) Hybrid dipolar modes of the nanorod trimer are calculated using a coupled oscillator model. (b) Absorption spectrum (top) of one of the nanorod trimers measured with photothermal spectroscopy using a 532 nm probe laser centered on the nanorod trimer (blue line). The simulated absorption spectrum (orange line) resolves two modes, labeled λ_1 and λ_2. The highest energy mode, λ_3, is inaccessible at this beam position. Scattering spectra (bottom) of the same nanorod trimer measured (blue line) and computed (orange line) are shown. The resonance at 700 nm is not resolved in experiment likely due to nanofabrication differences between simulation and experiment. (c) Histogram depicting the variability in experimental absorption resonance position of 19 individual nanorod trimers studied.

determined by the acousto-optic filter that selects the pump wavelength from a white-light laser), while the third hybrid mode, λ_3, is inaccessible when the pump beam is focused at the nanorod trimer center. Because of the small imperfections in the otherwise equivalent nanorod trimers, each of the 19 structures has a slightly different absorption spectrum. Figure 4.1c shows a histogram of the wavelength corresponding to the peak in their individual absorption spectra.

Our photothermal microscopy approach relies on raster scanning the beam within a 1 μm $\times$ 1 μm region of interest surrounding an individual structure. Even though the nanorod trimer's dimensions are well below the diffraction limit, different centroid positions of the focused pump beam drive different weighting of the three hybrid LSP modes. Figure 4.2 depicts the simulated dependence of the absorption spectrum on the position of the pump beam centroid. The schematic in Figure 4.2a labels the location of five different focused beam positions where absorption spectra are calculated. The schematic (top left) depicts the pump beam waist when centered at the origin for wavelengths ranging from 600 (dark gray) to 900 nm (lighter gray).

The resulting absorption spectra as a function of beam position are shown in Figure 4.2b, where the colors and line styles of the spectra correspond to the illustration in Figure 4.2a. When the beam is positioned to the left of the nanorod trimer (solid red $\oplus$), above the nanorod trimer (dashed blue $\oplus$), and in the center of the nanorod trimer (solid black $\oplus$), the two lowest energy modes at λ_1 and λ_2 are approximately driven the same. The third mode is nearly completely undriven. However, when the beam is positioned beneath the nanorod trimer (dashed red $\oplus$), the λ_2 mode is driven most strongly. Lastly, when the beam is positioned to the right of the nanorod trimer (solid blue $\oplus$), the previously plane-wave dark λ_3 mode can be driven nearly as strongly as the other two modes. The pump wavelength specific absorption cross-section maps in Figure 4.2c depict this absorption asymmetry at the three LSP mode wavelengths as a function of beam centroid position. The black contour lines represent equipotentials of constant absorption.

Each of these absorption profiles underlies different temperature distributions that evolve

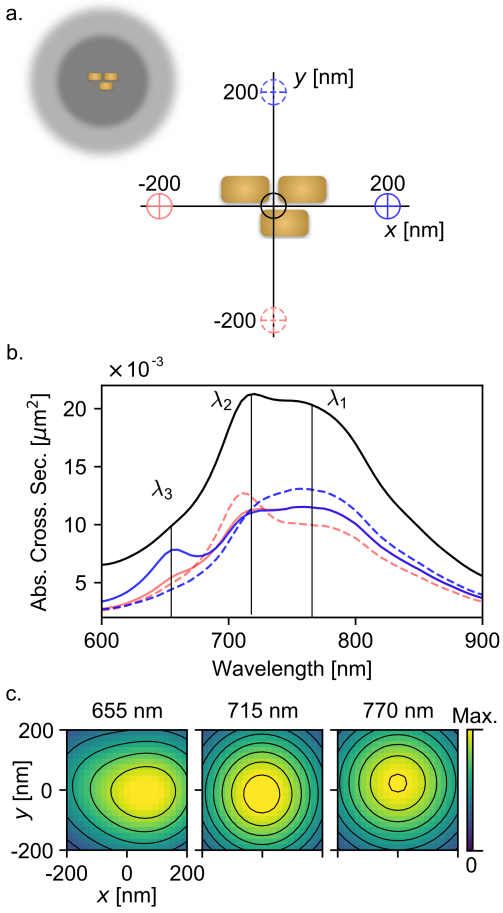

Figure 4.2: Focused pump beam drives different weighting of the three hybrid LSP modes depending on its centroid position relative to the nanorod trimer structure. (a) Illustration of the five beam positions with respect to the position of the nanorod trimer selected for simulations. The colors and line styles of the cross hairs correspond to the absorption spectra in the following panel. The schematic in the top left corner indicates the beam waist size when at the origin for a 600 nm wavelength pump beam (dark gray) and 900 nm wavelength pump beam (light gray). (b) Different absorption spectra resulting from the focused beam driving the nanorod trimer at the five labeled beam positions. When the beam is positioned at the solid red $\oplus$, the dashed blue $\oplus$, and the solid black $\oplus$, the two lowest energy modes are driven approximately equally. However, when the beam is located at the dashed red $\oplus$ or the solid blue $\oplus$, the λ_2 or λ_3 modes are strongly driven, respectively. (c) Absorption cross-section maps as a function of beam centroid at the three resonances. The overlaid black lines show equal contours of the absorption map. The color scale of the 655 nm image has been scaled up by a factor of 2 for ease in comparison with the more intense absorption maps at 715 and 770 nm.

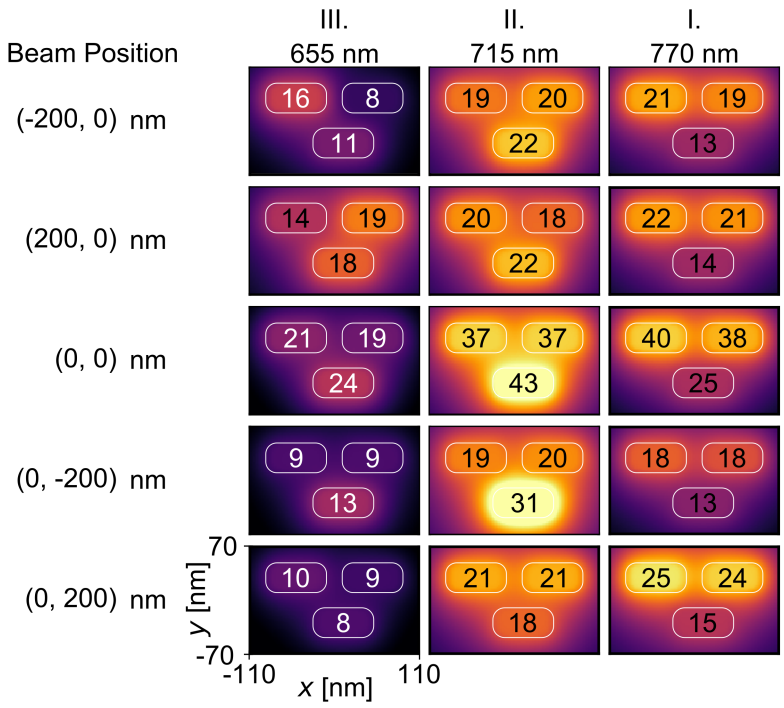

Figure 4.3: Wavelength and beam centroid dependent computed temperature maps of the nanorod trimer. Steady-state temperature maps of the nanorod trimer at the three hybrid modes and five unique beam positions labeled in Figure 4.2a. The temperatures listed are degrees Celsius above room temperature.

as a function of pump beam position and wavelength. Figure 4.3 depicts the computed thermal profiles associated with the five beam centroid positions displayed in Figure 4.2. Here, the steady-state temperature profiles are calculated using the thermal discrete dipole approximation,[33] and reflect the temperature of the particles above ambient room temperature. When the structure is excited at the lowest energy LSP mode, $\lambda_1 = 770$ nm, the top two particles heat up more than the bottom particle at every beam position in the 400 nm wide window shown. At the second hybrid mode, $\lambda_2 = 715$ nm, the temperature pattern switches with the bottom particle reaching higher temperatures than the top two for most (although not all) beam positions. Finally, the last hybrid mode, $\lambda_3 = 655$ nm, produces a more complex thermal profile that depends on the pump beam position with absolute and relative nanorod temperatures smaller than those found at λ_1 and λ_2. See Figure S1 for temperature difference maps at each beam position.

The prediction that the induced temperature shifts between the top region being hotter (when excited around 770 nm) to the bottom region being hotter (around 715 nm) is probed with photothermal microscopy. The images of 19 nanorod trimers are acquired by raster scanning the sample across the pump and probe lasers in a collinear focused beam geometry. 180 nm diameter gold nanodisks are measured alongside each nanorod trimer and are expected to generate uniform heating, thereby acting as a reference. Figure 4.4 shows the resulting photothermal images at two pump wavelengths, 700 and 800 nm, near the two lowest energy LSP modes of a representative nanorod trimer and nanodisk pair. The differences among the images are quantified by fitting the data to a point spread function (PSF) described by a 2-dimensional Gaussian $I(x,y) = A \cdot \exp\Big(- \frac{(x-x_0)^2}{2\sigma_x^2} - \frac{(y-y_0)^2}{2\sigma_y^2} \Big)$, where (x_0, y_0) is the Gaussian peak position, A is the amplitude, and σ_x, σ_y are the Gaussian widths in x and y. The Gaussian widths were converted into fwhm by the relationship $\mathrm{FWHM}_{x,y} = 2\sqrt{2\ln 2} \cdot \sigma_{x,y}$. The fits are shown in the second row of Figure 4.4. As expected, $\mathrm{fwhm}_x = \mathrm{fwhm}_y$ for the PSFs of the nanodisks under both 700 and 800 nm pump wavelengths. This result serves as a reference allowing us to correct for any wavelength-dependent asymmetry due to variation within our imaging setup. The nanorod trimer on the other hand exhibits a different PSF

than the nanodisk. The nanorod trimer image at 700 nm is elongated along the x-direction resulting in an asymmetry factor ($\text{fwhm}_x/\text{fwhm}_y$) larger than one. At 800 nm, the nanorod trimer image appears symmetric.

Simulated photothermal images are used to interpret the observed asymmetries in the experimental nanorod trimer PSFs. The simulated images are obtained by raster scanning a focused Gaussian beam across a nanorod trimer or nanodisk and integrating the superposition of the scattered field and the transmitted probe field over the solid angle (θ_d, ϕ_d) spanning the detector in the forward direction according to[59, 102]

$$I^{\text{PT}} = \frac{cn}{8\pi} \int\int_{(\theta_d,\phi_d)} (|\mathbf{E}_{\text{H}}(\theta,\phi) + \mathbf{E}_{\text{p}}(\theta,\phi)|^2 - |\mathbf{E}_{\text{R}}(\theta,\phi) + \mathbf{E}_{\text{P}}(\theta,\phi)|^2)\text{d}\Omega \tag{4.1}$$

where c is the speed of light, n is the refractive index at the detector, $\mathbf{E}_{\text{H,R}}(\theta,\phi)$ is the probe electric field scattered through the heated (H) or room (R) temperature system, $\mathbf{E}_{\text{P}}(\theta,\phi)$ is the probe beam (in the absence of the target) modeled as a Gaussian beam, and θ, ϕ are evaluated at the detector located 1 cm away. The collection angle of the photothermal experiment defines the bounds of integration for the simulation, which are set to be $\theta_d = 35°$ and $0° \leq \phi_d \leq 360°$. The scattered electric field through the heated system, $\mathbf{E}_{\text{H}}(\theta,\phi)$, is calculated by assigning the gold refractive index values according to the temperatures calculated at each wavelength and beam position. See section S4 for a description of the experimental temperature-dependent refractive indices of gold and section S3 for comparison to an alternative image function derived in Ref. [103]. The infinite glycerol background is assigned an increased refractive index corresponding to the average temperature of the gold particles. The resulting simulated photothermal images of the nanorod trimer and nanodisk are shown in the last row of Figure 4.4. The simulated PSFs for the nanodisk are symmetric for both the 700 and 800 nm pump, as is the case for the experimental images. The simulated nanorod trimer PSFs exhibit nearly symmetric PSFs at both 700 nm ($\text{fwhm}_x/\text{fwhm}_y = 0.99$) and 800 nm pump ($\text{fwhm}_x/\text{fwhm}_y = 1.02$), differing from the experimental results. This apparent contradiction between theory and experiment is further explored by comparing the

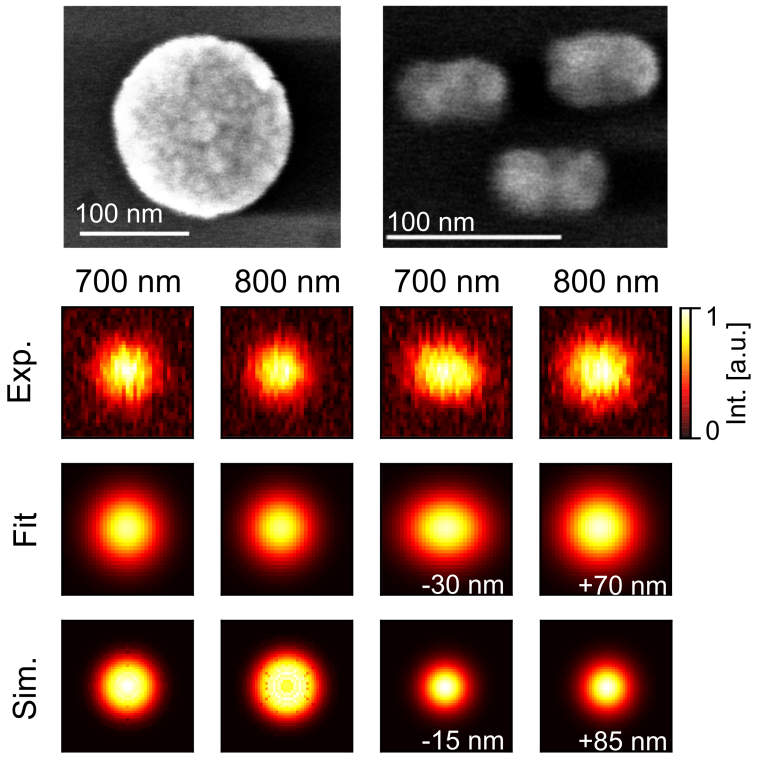

Figure 4.4: Photothermal images of a nanodisk (left two columns) and a nanorod trimer (right two columns) with representative SEM images shown on top. The image sizes of the experimental, fit, and simulated images are $1\mu m \times 1\mu m$. The first row depicts experimentally obtained photothermal images of the structures pumped at 700 and 800 nm with 190 and 170 μW powers. The second row shows the fit of the raw data to a 2-dimensional Gaussian function. The asymmetry in the PSF of the nanorod trimer at 700 nm is apparent and juxtaposed against the symmetric nanodisk images. The last row depicts the simulated photothermal images of the nanodisk and nanorod trimer. The printed values on the fit and simulated nanorod trimer images indicate the difference in wavelength between the pump wavelength and the nanorod trimer's absorption maximum. Each image has been individually normalized. Note that it is the asymmetry between the x and y FWHM values that are of importance for comparison between experiment and theory and not their absolute widths.

spectrally resolved simulations and experimental distributions.

Statistics of the PSF fit parameters extracted from the photothermal images are shown in Figure 4.5 for the 19 nanorod trimers investigated. The values have been corrected to account for effects of alignment drift and aberrations. The correction involves two steps: first, the PSF fwhm in each direction is normalized by the value of the nanodisk in the same direction (e.g., $\text{fwhm}_{x,\text{trimer}}/\text{fwhm}_{x,\text{disk}}$). The nanodisks and nanorod trimers are fabricated next to each other on the sample and a nanodisk-nanorod trimer pair is always imaged together, thus drift and aberrations in the system are captured by the nanodisk PSF and corrected for in the nanorod trimer PSF. In the second step, the normalized nanorod trimer fwhm values are multiplied by the average nanodisk fwhm as a universal scaling factor. Note that, even without normalization and correction, we still observe the same signature in the nanorod trimer images (Figure S2).

Figure 4.5a presents a histogram of the fwhm in the x- and y-directions from the fits of the nanodisk and nanorod trimer images at the two pump wavelengths. Just as qualitatively observed in Figure 4, under 700 nm pump, the fwhm in the x-direction (blue) is larger than the fwhm in the y-direction (orange) for nearly all nanorod trimers. Similarly, under 800 nm pump the fwhm in the x-direction is larger than the fwhm in the y-direction but to a smaller extent, making it not apparent in Figure 4. The statistical test results summarized in Table S1 confirm a statistically significant difference between fwhm_x and fwhm_y at 700 nm. Similarly, a smaller yet statistically significant difference at 800 nm is also observed.

To rule out any effect of scan direction or pump beam polarization, the sample was imaged in two different scan directions and two sample directions (Figure S3). The results in Figure S4 show that scan direction has no effect on the values of the nanodisk-corrected asymmetry factor at 700 nm pump. Also, any effect possibly resulting from sample orientation at 700 nm pump is negligible as shown in Figure S5. The correlation plot in Figure S6 illustrates that there is no correlation in sample orientation at 800 nm excitation as seen from the data clustering around $(1, 1)$. Furthermore, the asymmetry factors at the two different pump wavelengths are negatively correlated; that is, trimers with larger asymmetries at

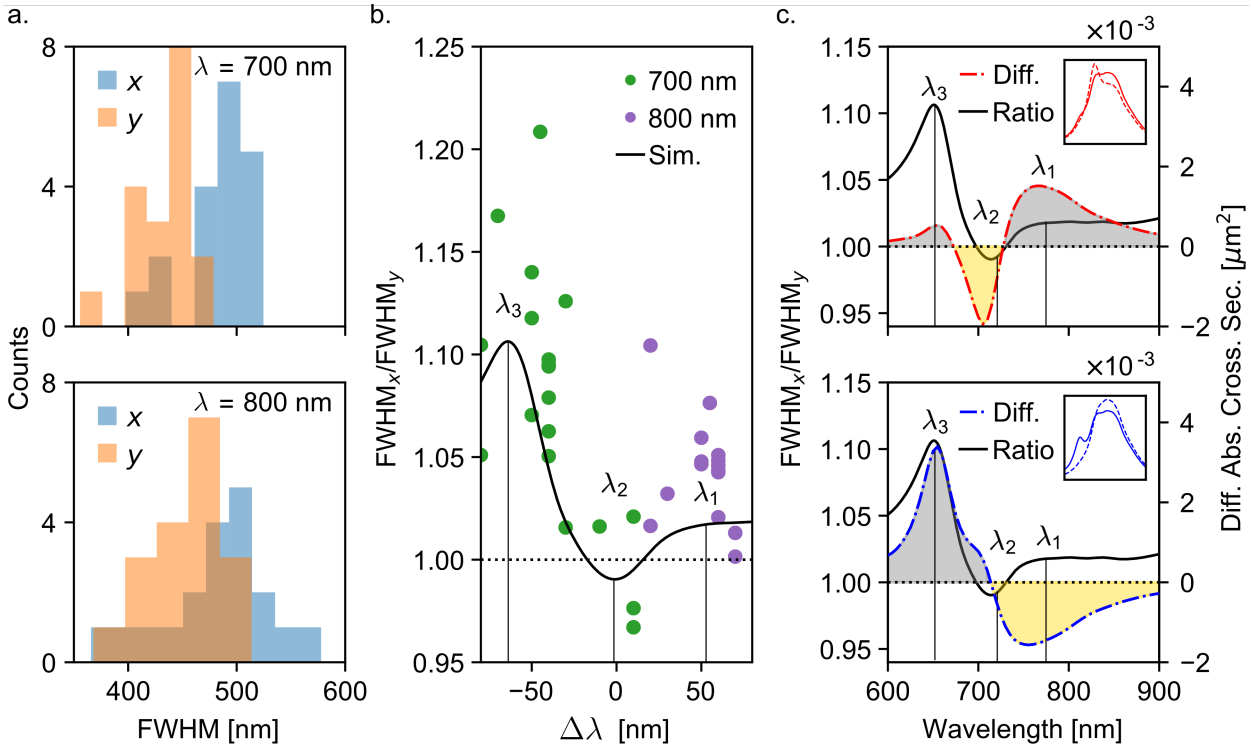

Figure 4.5: Spectra and photothermal image fitting results of different nanorod trimer structures. (a) Values of the fwhm in the x- and y-directions corrected by the nanodisk at 700 and 800 nm pump wavelengths are shown. (b) Experimental x and y fwhm ratios at 700 nm (green dots) and 800 nm (purple dots). The simulated fwhm ratios are shown by the black line. To align the experimental and simulated data on the same x-axis, the difference between the peak absorption and the pump wavelength is used. The width of the data points indicates the error in $\Delta\lambda$ according to the bandwidth of the pump laser (10 nm). The distribution in the asymmetry values comes from the different absorption maxima of the 19 nanofabricated nanorod trimers (Figure 1c). Note that the simulated and experimental data agree quantitatively without any scaling or adjustable parameters. (c) Differences between the absorption cross sections (from Figure 2b and reproduced in the insets) as a function of beam position. Absorption cross-section differences (dot-dashed curves) between beam positions (-200 nm, 0 nm) and (0 nm, -200 nm) indicated in red (upper panel) and beam positions (200 nm, 0 nm) and (0 nm, 200 nm) indicated in blue (lower panel).

700 nm will likely have smaller asymmetries at 800 nm and vice versa (Figure S7). These control experiments verify that the observed PSF asymmetries are generated by changing the wavelength of the pump beam and not by sample orientation or scan direction.

To understand the full wavelength-dependence of the photothermal images of the nanorod trimer, the data from Figure 5a is replotted to show the fwhm ratio ($\text{fwhm}_x/\text{fwhm}_y$) at the 700 nm pump wavelength (green dots) and at the 800 nm pump wavelength (purple dots) (Figure 4.5b). The experimental and simulated data are plotted on a common x axis by subtracting the pump wavelength (700 $\pm$ 5 and 800 $\pm$ 5 nm for green and purple dots, respectively) from the nanorod trimer absorption maximum (illustrated in Figure 1c) to find the distance of the resonance maximum from the pump wavelength ($\Delta\lambda$). Specifically, each nanorod trimer has a different absorption maximum with a range spanning from 690 to 780 nm (Figure 1c). By calculating the differences between the pump wavelengths of 700 and 800 nm and the resonance maxima of the nanorod trimers, a range of $\Delta\lambda$ values between -80 and 110 nm is obtained. This is equivalent to having a single maximum peak for all the nanorod trimers and sweeping the pump beam wavelength. Using this approach, we obtain the wavelength dependence of the asymmetry for the experimental trimer images. Simulated fwhm ratios at different pump wavelengths for a fixed calculated absorption spectrum (Figure 1b) are overlaid and given by the black line. These simulated fwhm ratios are obtained by fitting the photothermal images of the nanorod trimer pumped with wavelengths ranging from of 610 to 790 nm. The maximum in the simulated absorption spectrum of the nanorod trimer (715 nm) is then subtracted from the specific pump wavelength.

When the pump beam excites the nanorod trimer at wavelengths greater than or equal to the λ_1 ($\Delta\lambda \geq 55$nm) absorption resonance, the fwhm ratio is greater than one (Figure 4.5b). This excitation corresponds to the lowest energy hybrid mode, where the upper two nanorods heat up more than the lower nanorod (Figure 3, column I). The thermal lens created by the hotter upper nanorod pair is broader in the x direction than the y direction leading to an elongation in the photothermal image in the x direction and an asymmetric PSF. As the excitation wavelength approaches the λ_2 absorption resonance and goes slightly

to shorter wavelengths ($\Delta\lambda \approx 0$ nm), the fwhm ratio then dips below one (Figure 4.5b). In this case, the lower nanorod for most beam positions is significantly hotter than the upper pair (Figure 3 Column II) and the associated image distorts to slightly favor the y-direction, as evident in a fwhm ratio below 1 at $\Delta\lambda \approx 0$ nm. Finally, as the pump beam excites the nanorod trimer at shorter wavelengths near the λ_3 absorption resonance ($\Delta\lambda$ = -60 nm), the planewave dark mode becomes optically accessible to the focused beam excitation with a highly spatially dependent thermal profile. The excitation of the dark mode results in the increased asymmetry observed at $\Delta\lambda$ = -60 nm, which occurs when the pump wavelength is blue-shifted 60 nm from the absorption peak of the nanorod trimer.

The PSF asymmetries induced by beam position and pump wavelength are made more apparent when comparing the difference in absorption cross sections at the spatial positions marked in Figure 2a. Figure 5c demonstrates that the pump wavelength-dependent asymmetry is qualitatively reproduced by the differences in the spatially dependent absorption cross sections shown in Figure 2b calculated at different focused illumination beam positions. Those absorption cross sections have been reproduced in the insets of Figure 4.5c. Specifically, we find that by taking the difference between the absorption cross sections at (-200 nm, 0 nm; solid red) and (0 nm, -200 nm; dashed red), the resulting trace (dot-dashed red) changes sign where the fwhm ratio (black) dips above and below one at nearly the same wavelengths. Further insight is gained when similarly taking the difference between the absorption cross sections at (200 nm, 0 nm; solid blue) and (0 nm, 200 nm; dashed blue). In this case, there is a maximum at the same position as the dominant peak in the ratio plot. This maximum is due to the asymmetric driving capability of the focused beam in exciting the plane-wave dark mode λ_3. Certain beam positions preferentially excite one hybrid mode more strongly than the others, contributing to the distortion of the photothermal image. This result makes clear how the peak in the fwhm ratio near 650 nm ($\Delta\lambda$ = -60 nm) is due to the pump beam asymmetrically exciting the third hybrid mode.

Except for the λ_3 mode in the lower panel of Figure 4.5c, we observe that these cross-section differences change sign (indicated by the shaded spectral regions) at approximately

the same wavelengths where asymmetries in the PSFs occur, as reflected in the plotted fwhm ratio. Thus, these trends reveal how the measured asymmetry in the fwhm originates from spatial differences in absorption that depend upon the location of the pump beam. The observed PSF asymmetries are therefore correlated with asymmetric local heating of the nanorod trimer and the resulting inhomogeneous temperature changes that ensue. Taken together, these trends in the fwhm ratio reflect the spatial and wavelength-dependence of the absorbing hybrid LSP modes as well as their associated spatially- and wavelength-dependent thermal responses. Therefore, by combining our photothermal imaging measurements with corresponding numerical simulations, we are able to elucidate an indirect route to retrieve nanoscale thermal information using purely optical techniques.

4.4 Conclusion

In conclusion, we have demonstrated how asymmetries in the photothermal images of individual gold nanorod trimers excited at their hybridized LSP resonances are correlated with the spatially inhomogeneous thermal profiles associated with each mode. In particular, we showed how subdiffraction limited thermal gradients within the nanorod trimer can be controlled using focused laser excitation at different wavelengths and how these gradients are encoded as asymmetries in the fwhm of the 2-dimensional PSFs obtained from the photothermal images. Theoretical modeling of the nanorod trimer's optical and thermal responses together with the imaging optics allowed us to explicitly connect the experimental photothermal images with precise nanoscale temperature values. In this manner, we have demonstrated a new procedure combining experimental imaging and photothermal modeling to perform all-optical thermometry measurements on individual nanoscale objects that are smaller than the diffraction limit of light.

4.5 Methods

4.5.1 Experimental

Photothermal imaging was performed on a Zeiss inverted microscope. The pump-probe geometry consists of a 532 nm laser diode probe and a tunable VIS/NIR pump controlled using an acousto-optic tunable filter with a bandwidth of 10 nm. The lasers were collinearly focused on the sample using a 63 × 1.4 NA oil immersion objective. A 50 × 0.7 NA air objective was used to collect the light transmitted through the sample. The pump laser was filtered out using a band pass filter allowing only the transmitted/scattered probe beam to be collected. The transmitted probe beam was focused on a Si photoreceiver with a low noise voltage amplifier and processed with a lock-in amplifier, which used the signal driving the acoustooptic tunable filter modulation as the reference frequency (100 kHz). The photothermal signal at a specific position was created as the probe beam interacted with an oscillating refractive index generated by modulating the pump intensity (temporally changing the refractive index of the sample if there is appreciable absorption), causing differential scattering of the probe beam. This oscillating signal was detected through lock-in amplification. A photothermal image was formed by scanning the sample across the focused pump/probe beam using a piezo positioning stage, where the stage position provides the x and y position, and the probe signal provides the photothermal signal. Absorption spectra of individual structures were obtained by recording the signal intensity for a 210 μW probe beam (as measured incident at the sample plane) at the centroid of a single structure and scanning the pump wavelength (500–1000 nm) with a power of $\tilde{1}80\mu$W at 700 nm using an acousto-optic tunable filter. A reference gold film next to the structures was used to correct for the pump intensity as its wavelength was scanned according to previous work.[8] The particle spectrum was then normalized by the reference gold spectrum and corrected for the theoretical absorptivity of gold to obtain the final absorption spectrum for each particle or trimer.

4.5.2 Theoretical

The computational approach for obtaining the photothermal images used DDSCAT 7.31 modified to account for a Gaussian beam excitation source and the thermal discrete dipole approximation (T-DDA).[33] The scattering calculations were performed on gold nanorod trimers using an experimentally obtained temperature-dependent dielectric data set (See section S4) with 2 nm dipole spacing in a uniform infinite glycerol background with refractive index n = 1.473. The resulting electric field and polarization information within the nanorods were used as inputs for the steady-state temperature calculation performed in T-DDA, which includes a semi-infinite silica ($\kappa = 1.38$ W/m K) substrate. The temperatures of each nanorod were then used to select the appropriate temperature-dependent dielectric values for a second scattering calculation. This second scattering calculation was performed at an off-resonant probe wavelength of 600 nm with the nanoparticles embedded in a uniform background with a temperature-dependent refractive index value evaluated at the average nanoparticle temperature of the trimer. The focal spot of the probe beam was selected to be at the interface between the particle and the substrate. The resulting scattered electric fields were evaluated on a partial hemisphere 1 cm away from the particles and were used to calculate the total intensity as shown in the main text. To obtain the entire two dimensional photothermal image, this full procedure was carried out for a range of co-scanned excitation and probe beam positions that spanned a region of interest surrounding the nanorod trimer system.

4.6 Acknowledgments

This work was supported by the U.S. National Science Foundation under Grants NSF CHE-1727092 (D.J.M), CHE1727122 (S.L.), and CHE-1728340 (K.A.W.). S.L. also acknowledges support from the Robert A. Welch Foundation (Grant C-1664). The experimental work was conducted in part using resources of the Shared Equipment Authority at Rice University. The theoretical work was facilitated through the use of advanced computational, storage, and networking infrastructure provided by the Hyak supercomputer system at the University of

Washington. C.R.B. was supported by the NSF Partnerships for International Research and Education program at the University of Pennsylvania (NSF-PIRE, OISE1545884)

Chapter 5

NONLINEAR EFFECTS IN PHOTOTHERMAL MICROSCOPIES AND SPECTROSCOPIES OF STRONGLY SCATTERING PLASMONIC NANOPARTICLES

5.1 Introduction

The challenge to detect nanoparticles and measure their optical properties has inspired the development of numerous photothermal microscopies and spectroscopies [104, 105]. While there are different ways to perform these experiments on nanoparticles, many rely on detecting a refractive index change in the environment induced by a temperature increase from photons absorbed by the nanoparticle(s). Early pioneers of this approach used a modulated heating laser to generate a time-dependent heat distribution originating from the absorbing nanoparticle(s), and an off-resonance probe laser for detection [96, 58, 61]. The success of these experiments result from two phenomena which increase magnitude of the signal. First, by heating the nanoparticles with an on-resonant laser, the refractive index change causes the probe to scatter more compared to the non-heated system. Second, because the interference between the unperturbed transmitted or reflected probe laser and the scattered light $\mathbf{E}_{\text{int}}$ is much larger than the scattered signal alone $\mathbf{E}_{\text{sca}}$ (for small nanoparticles), a boost in signal occurs by measuring this interference. Detecting this interference signal produced from the heated system enables the measurement of traditionally non-scattering particles.

More recently, photothermal imaging has been used to detect larger particles and more sophisticated nanoparticle arrangements.[106, 107, 108]. Furthermore, researchers have demonstrated it may be used to infer temperature gradients in near-diffraction [14] and sub-diffraction [10] hybridized plasmonic systems. When the measurement is pushed into these new regimes, some assumptions made in the original models (e.g., $\mathbf{E}_{\text{int}} > \mathbf{E}_{\text{sca}}$) are no

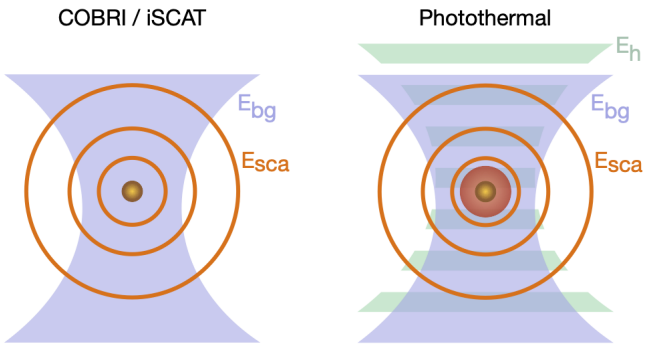

Figure 5.1: Illustration of iSCAT / COBRI microscopy approaches compared against photothermal microscopy. While both experiments are based on the interference between a reference signal and a scattered signal, the photothermal experiment has an additional modulated heating beam which elevates the temperature around the particle and increases the scattering signal. Furthermore, the photothermal experiment has a lockin detector which works to isolate the modulated signal from the background signal.

longer valid. Therefore, extracting physical meaning from the photothermal measurement on larger nanoparticle systems requires readdressing the underlying theories developed in the earlier work.

Models of other interferometry experiments similar to the photothermal measurement have been created to study larger, scattering nanoparticle systems. Two such experiments: coherent brightfield microscopy (COBRI) and interferometric scattering microscopy (iSCAT) are very closely related to photothermal microscopy. However in these approaches, the system is not heated. For these experiments, researchers have developed models of the interferometric scattering signal between the signal scattered by (room temperature) nanoparticles and a reference field [109, 110]. Often, the reference field is either the transmitted (COBRI) or reflected (iSCAT) probe beam. Recently developed models have incorporated the impacts of larger, scattering nanoparticles.[106, 111].

Herein, a new model is developed which approximates the photothermal signal produced by both small and large spherical nanoparticles measured in a confocal photothermal microscope. This approach extends the effective dipole model developed in Refs. [61, 112, 113, 103]

in order to account for large, scattering nanoparticles. It uses features similar to those developed in COBRI / iSCAT models [106, 111], yet with the incorporation of a modulated heating beam and lockin detection. Fig. 5.1 depicts a comparison between photothermal imaging experiment and the iSCAT / COBRI experiments. In both experiments, the signal which reaches the detector is $I_{\text{det}} = \frac{cn_b}{8\pi}\left|\mathbf{E}_{\text{bg}} + \mathbf{E}_{\text{sca}}\right|^2$ where the background field, $\mathbf{E}_{\text{bg}}$, is assumed to be either the transmitted or reflected probe beam. In terms of interferometry experiments, this field is referred to as the reference field. (The laser which heats the system produces a field $\mathbf{E}_{\text{h}}$, but is filtered out before reaching the detector.) However in the photothermal experiment, the detector is a lockin detector which extracts out the modulated heated signal. Many lockin detectors report the signal, Φ, with the following magnitude and phase [113]:

$$\Phi = \sqrt{\Phi_{\text{sin}}^2 + \Phi_{\text{cos}}^2} \qquad \Psi = \arctan\left[\frac{\Phi_{\text{sin}}}{\Phi_{\text{cos}}}\right] \tag{5.1}$$

where Φ_{cos} and Φ_{sin} are determined from the signal pre-lockin, $\Phi_{\text{pre}}(t)$

$$\Phi_{\left\{\substack{\text{sin}\\\text{cos}}\right\}} = \frac{1}{\tau}\int_0^\tau \Phi_{\text{pre}}(t)\left\{\begin{matrix}\sin\Omega t\\ \cos\Omega t\end{matrix}\right\}dt. \tag{5.2}$$

The signal pre-lockin, sometimes referred to as the normalized photothermal signal, takes the form:

$$\Phi_{\text{pre}}(t) = \frac{I_{\text{det}}(t) - I_{\text{bg}}}{I_{\text{bg}}}. \tag{5.3}$$

Prior photothermal models approximate $I_{\text{det}}(t)$ as

$$\begin{aligned} I_{\text{det}}(t) =& \frac{cn_b}{8\pi}\left|\mathbf{E}_{\text{bg}} + \mathbf{E}_{\text{sca}}(t)\right|^2 = \frac{cn_b}{8\pi}\left|\mathbf{E}_{\text{ref}} + \mathbf{E}_{\text{sca}}(t)\right|^2 \\ \approx& \frac{cn_b}{8\pi}\Big[|\mathbf{E}_{\text{ref}}|^2 + 2\text{Re}[\mathbf{E}_{\text{ref}}\cdot\mathbf{E}_{\text{sca}}^*(t)]\Big]. \end{aligned} \tag{5.4}$$

However, for photothermal imaging on large nanoparticles, $|\mathbf{E}_{\text{sca}}|^2$ may no longer be approximated as zero. A new model which incorporates these scattering effects will be presented in the following section. It is based on the model developed in Ref. [103], but is based on

different lockin scheme and different forms of the transmitted probe and scattered fields.

5.2 Effective Core-Shell Dipole Model with Scattering Effects

. The following model is designed to describe photothermal experiments in the transmission geometry where the background signal is the unperturbed probe field ($\mathbf{E}_{\mathrm{p}}$) and is treated as the reference field, $\mathbf{E}_{\mathrm{bg}} = \mathbf{E}_{\mathrm{p}} = \mathbf{E}_{\mathrm{ref}}$. As proposed in Refs. [103, 106], the heated system can be considered to be a time-dependent core-shell dipole model where the core is the metal nanoparticle and the shell is the background medium at the temperature-induced increased refractive index. Prior dipole models often only consider the scattering from the ball of increased refractive index and refer to it as a thermal lens. However in this model, both the scattering from the metal and the thermal lens will be accounted for using a core-shell polarizability.

The signal which reaches the detector is therefore

$$I_{\mathrm{det}}(t) = \frac{cn_b}{8\pi}\left|\mathbf{E}_{\mathrm{p}}(t) + \mathbf{E}_{\mathrm{sca}}(t)\right|^2 = \frac{cn_b}{8\pi}\left[|\mathbf{E}_{\mathrm{p}}(t)|^2 + |\mathbf{E}_{\mathrm{sca}}(t)|^2 + 2\mathrm{Re}[\mathbf{E}_{\mathrm{p}}(t)\cdot\mathbf{E}^*_{\mathrm{sca}}(t)]\right] \tag{5.5}$$

where n_b is the refractive index of the background material. The heating beam is amplitude modulated at Ω according to $P_{\mathrm{h}} = \frac{1}{2}P_{0,\mathrm{h}}(1+\cos\Omega t)$, where Ω is on the order of kHz. The detector "locks in" only to the signals which vary in-phase and out-of-phase with this oscillation. Following the definition of the signal pre-lockin in Eq. 5.3, $\Phi_{\mathrm{pre}}(t)$ in this model is:

$$\begin{aligned}\Phi_{\mathrm{pre}}(t) &= \frac{|\mathbf{E}_{\mathrm{sca}}(t)|^2 + 2\mathrm{Re}[\mathbf{E}_{\mathrm{p}}(t)\cdot\mathbf{E}^*_{\mathrm{sca(t)}}]}{|\mathbf{E}_{\mathrm{p}}(t)|^2} \\ &\equiv \Phi_{\mathrm{sca}}(t) + \Phi_{\mathrm{int}}(t)\end{aligned} \tag{5.6}$$

where $\Phi_{\mathrm{sca}}(t)$ and $\Phi_{\mathrm{int}}(t)$ have been introduced to label the pure scattering portion of the signal and the interference portion of the signal.

The heating and probe focused beams are well-approximated as Gaussian beams. The

electric field of a Gaussian beam (derived in Appendix B) which propagates in the $+z$ direction, polarized in the x direction, and is focused at a z offset position z_f is:

$$\mathbf{E}_{\mathrm{g}}(\mathbf{x},t) = E_0\hat{\mathbf{x}}\frac{w_0}{w(z)}e^{-(x^2+y^2)/w(z)^2}e^{ik(z-z_f)}e^{ik(x^2+y^2)/(2R(z))}e^{-i\psi(z)}e^{-i\omega t} \tag{5.7}$$

where w_0 is the beam waist, $w(z)$ is the radius where the field amplitude at the plane z along the beam is $1/e$ the value of that on the axis, $R(z)$ is the radius of curvature of the beam, and $\psi(z)$, the Gouy phase which changes the polarization direction from positive to negative across the focus. Mathematically, these quantities are $w(z) = w_0\sqrt{1+\left(\frac{z-z_f}{z_R}\right)^2}$, $R(z) = (z-z_f)\left(1+\left(\frac{z_R}{z-z_f}\right)^2\right)$, and $\psi(z) = \arctan\left(\frac{z-z_f}{z_R}\right)$ where $z_R = \pi w_0^2 n_b/\lambda$ is the Rayleigh range which corresponds to z distance along the beam where the cross sectional area is double compared to at the focus.

For this photothermal experiment, the reference field is the unhindered transmitted field of the incident probe beam evaluated at the detector, $\mathbf{E}_{\mathrm{ref}}(\mathbf{x},t) = \mathbf{E}_{\mathrm{g}}(\mathbf{x}=\mathbf{x}_{\mathrm{d}},t)$. $\mathbf{x}_{\mathrm{d}}$ is the position of the detector, which is assumed to be on the optical axis in the far field. The scattered field may be modeled using $\mathbf{E}_{\mathrm{sca}}(\mathbf{x},t) = \mathbf{G}(\mathbf{x})\cdot\alpha_{\mathrm{pt}}(t)\mathbf{E}_{\mathrm{g}}(\mathbf{x}=\mathbf{x}_{\mathrm{np}},t)$ where $\mathbf{G}(\mathbf{x})$ is the dipole relay tensor, $\mathbf{x}_{\mathrm{np}}$ is the position of the nanoparticle, assumed to be at the origin, and α_{pt} is the time-dependent photothermal polarizability (to be defined in the next section). The Gaussian beam evaluated at the detector $\mathbf{x}_{\mathrm{d}}$, and at the nanoparticle $\mathbf{x}_{\mathrm{np}}$, is approximated as:

$$\begin{aligned}
\mathbf{E}_{\mathrm{d}}(\mathbf{x},t) &= \mathbf{E}_{\mathrm{g}}(z >> (x,y,z_f),t) = \frac{E_0\hat{\mathbf{x}}}{z/z_R}e^{ik(z-z_f)}(-i)e^{-i\omega t} \\
\mathbf{E}_{\mathrm{np}}(\mathbf{x},t) &= \mathbf{E}_{\mathrm{g}}(\mathbf{x}=0,t) = \frac{E_0\hat{\mathbf{x}}}{\sqrt{1+(-z_f/z_R)^2}}e^{-ikz_f}e^{-i\arctan(-z_f/z_R)}e^{-i\omega t}
\end{aligned} \tag{5.8}$$

where $w(z) \approx w_0 z/z_R$ and $e^{-i\psi(z)} \approx -i$ at the detector ($z \to \infty$). The Gaussian beam in these limits may be used to calculate the reference and scattered fields from a nanoparticle / thermal lens target. Taking the probe field focus to be at z_p and using these new limits of

the Gaussian beam,

$$\mathbf{E}_{\mathrm{p}}(\mathbf{x},t) = \mathbf{E}_{\mathrm{d}}(\mathbf{x},t) = -i\frac{z_R}{z}E_0\hat{\mathbf{x}}e^{ik(z-z_p)}e^{-i\omega t}$$
$$\mathbf{E}_{\mathrm{sca}}(\mathbf{x},t) = \mathbf{G}(\mathbf{x})\cdot\alpha_{\mathrm{pt}}(t)\mathbf{E}_{\mathrm{np}}(\mathbf{x},t) = \frac{k^2e^{ikr}(\mathbf{1}-\hat{\mathbf{r}}\hat{\mathbf{r}})}{r}\cdot\frac{\alpha_{\mathrm{pt}}(t)E_0\hat{\mathbf{x}}}{\sqrt{1+(-z_p/z_R)^2}}e^{-ikz_p}e^{-i\arctan(-z_p/z_R)}e^{-i\omega t} \tag{5.9}$$

where $\mathbf{G}(\mathbf{x})$ is evaluated in the far-field. Returning to Eq. 5.6:

$$\begin{aligned}
\Phi_{\mathrm{int}}(\theta,\phi,t) &= \frac{2\mathrm{Re}[\mathbf{E}_{\mathrm{p}}\cdot\mathbf{E}^*_{\mathrm{sca}}]}{|\mathbf{E}_{\mathrm{p}}|^2} \\
&= 2\mathrm{Re}\Big[-i\frac{z}{z_R}e^{ik(z-z_p)}\frac{k^2e^{-ikr}}{r}\frac{\alpha(t)^*_{\mathrm{pt}}}{\sqrt{1+(-z_p/z_R)^2}}e^{ikz_p}e^{-i\arctan(-z_p/z_R)}\Big](1-\sin^2\theta\cos^2\phi) \\
&= 2\mathrm{Im}\Big[\frac{k^2}{z_R}\frac{\alpha(t)^*_{\mathrm{pt}}}{\sqrt{1+(z_p/z_R)^2}}e^{-i\arctan(-z_p/z_R)}\Big](1-\sin^2\theta\cos^2\phi) \\
&= \frac{4}{w_0^2\sqrt{1+(z_p/z_R)^2}}k\mathrm{Im}\Big[\alpha_{\mathrm{pt}}(t)^*e^{-i\arctan(-z_p/z_R)}\Big](1-\sin^2\theta\cos^2\phi)
\end{aligned}$$

$$\begin{aligned}
\Phi_{\mathrm{sca}}(\theta,\phi,t) &= \frac{|\mathbf{E}_{\mathrm{sca}}|^2}{|\mathbf{E}_{\mathrm{p}}|^2} \\
&= \frac{k^4}{r^2}|\alpha_{\mathrm{pt}}(t)|^2\frac{1}{1+(z_p/z_R)^2}\frac{z^2}{z_R^2}(1-\sin^2\theta\cos^2\phi)^2 \\
&= \frac{1}{z_R^2+z_p^2}k^4|\alpha_{\mathrm{pt}}(t)|^2(1-\sin^2\theta\cos^2\phi)^2
\end{aligned} \tag{5.10}$$

after making the approximation that $z \approx r$. One immediately notices here the resemblance of Φ_{int} to extinction (Eq. 2.14) and Φ_{sca} to scattering (Eq. 2.13).

The only term which will be impacted by the lockin integrals is the photothermal polarizability, $\alpha_{\mathrm{pt}}(t)$. Many prior models treat this polarizability as a thermal lens and model it using the Clausius-Mossotti polarizability. In this work, the photothermal polarizability will be modeled as a metal sphere surrounded by a large shell of uniformly heated background

material. (In this work, the background material is glycerol.) The next section will cover a derivation using the thermal lens only model, which recovers results previously derived. The following section will present a new model using a core-shell polarizability with retardation effects.

Both models approximate the temperature dependence of the photothermal polarizability using the following Taylor expansion:

$$\begin{aligned}\alpha_{\mathrm{pt}}(t) &\approx \alpha_{\mathrm{pt}}(T=T_0) + \frac{d\alpha_{\mathrm{pt}}}{dT}\Big|_{T=T_0}(T(\mathbf{x},t)-T_0) \\ &\approx \alpha_{\mathrm{pt},T_0} + \frac{d\alpha_{\mathrm{pt}}}{dn}\frac{dn}{dT}\Big|_{T=T_0} T_{\mathrm{avg}}(t)\end{aligned} \tag{5.11}$$

where dn/dT is the thermo-optic coefficient (for glycerol, $dn/dT \sim -10^{-4}$) and $T_{\mathrm{avg}}(t)$ is the average temperature over the target region above room temperature, T_0. This temperature $T_{\mathrm{avg}}(t)$ may be approximated by integrating the temperature rise outside a spherical heat source, $T_{\mathrm{sph}}(r,t)$, according to:

$$T_{\mathrm{avg}}(t) = \frac{4\pi}{V_{\mathrm{th}}}\int_0^{r_{\mathrm{th}}} r^2 T_{\mathrm{sph}}(r,t)dr \tag{5.12}$$

where $V_{\mathrm{th}} = 4/3\pi r_{\mathrm{th}}^3$ and $r_{\mathrm{th}} = \sqrt{2\kappa/c_p\Omega}$. The target volume, V_{th} is defined by the characteristic length for heat diffusion, the thermal radius r_{th}. The temperature rise $T_{\mathrm{sph}}(r,t)$ from a heat power source which is modulated according to $P_{\mathrm{abs}}(t) = \frac{1}{2}P_{\mathrm{abs},0}(1+\cos\Omega t)$. The resulting temperature rise (derived in Appendix D) is

$$T_{\mathrm{sph}}(r,t) = \frac{P_{\mathrm{abs},0}}{8\pi\kappa r}\Big(1 + e^{-r/r_{\mathrm{th}}}\cos\left(\Omega t - r/r_{\mathrm{th}}\right)\Big) \tag{5.13}$$

Integrating Eq. 5.12 leads to:

$$\begin{aligned}T_{\mathrm{avg}}(t) =& \frac{P_{\mathrm{abs},0}r_{\mathrm{th}}^2}{4e\kappa V_{\mathrm{th}}}\Big(e - \cos(1-\Omega t) + e\sin(\Omega t) + 2\sin(1-\Omega t)\Big) \\ =& \frac{P_{\mathrm{abs},0}r_{\mathrm{th}}^2}{\kappa V_{\mathrm{th}}}\big(0.25 + 0.105\cos(\Omega t) + 0.0732\sin(\Omega t)\big)\end{aligned} \tag{5.14}$$

The last remaining step is to assign the room temperature polarizability, α_{pt,T_0}, and it's derivative with respect to refractive index, $d\alpha_{\mathrm{pt}}/dn$.

5.3 Photothermal Polarizability in the Small Particle Limit

Small spherical metal nanoparticles primarily absorb light and do not scatter. This induces a temperature gradient and produces a large region of heated background with a modified refractive index. In this limit, it is appropriate to model the optical response of this system as a thermal lens, or a large sphere of heated background with volume V_{th} and a Clausius-Mossotti polarizability:

$$\alpha_{\mathrm{pt}}(T) = \frac{3V_{\mathrm{th}}}{4\pi}\epsilon_b \frac{\epsilon(T)-\epsilon_b}{\epsilon(T)+2\epsilon_b} \tag{5.15}$$

where $\epsilon(T)$ is the temperature-dependant dielectric function of the background medium. This makes $\epsilon(T=T_0)=\epsilon_b$. Using $\epsilon = n^2$,

$$\begin{aligned} \frac{d\alpha}{dn} &= \frac{3V_{\mathrm{th}}}{4\pi} n_b^2 \frac{2n(n^2+2n_b^2)-2n(n^2-n_b^2)}{(n^2+2n_b^2)^2} \\ \frac{d\alpha}{dn}\Big|_{T=T_0} &= \frac{V_{\mathrm{th}}}{2\pi} n_b \end{aligned} \tag{5.16}$$

and $\alpha_{\mathrm{pt},0}=0$. Thus,

$$\alpha_{\mathrm{pt}}(t) = \frac{dn_b}{dT}\frac{V_{\mathrm{th}}}{2\pi} n_b T_{\mathrm{avg}}(t) \tag{5.17}$$

Using Eq. 5.14, and $\Phi_{\mathrm{sca}} \approx 0$ for small particles, the lockin integral evaluates to:

$$\begin{aligned} \Phi_{\mathrm{int}\left\{\substack{\sin\\\cos}\right\}} =& \frac{4(1-\sin^2\theta\cos^2\phi)}{w_0^2\sqrt{1+(z_p/z_R)^2}} k \mathrm{Im}\left[e^{-i\arctan(-z_p/z_R)}\frac{1}{\tau}\int_0^\tau \frac{d\alpha_{\mathrm{pt}}^*}{dT}\Big|_{T_0} T_{\mathrm{avg}}(t)\begin{Bmatrix}\sin\Omega t\\ \cos\Omega t\end{Bmatrix} dt\right] \\ =& \frac{4(1-\sin^2\theta\cos^2\phi)P_{\mathrm{h},0}\sigma_{\mathrm{abs}}}{\pi w_{\mathrm{h},0}^2 \kappa\lambda} n_b^2 \frac{dn_b}{dT}\frac{r_{\mathrm{th}}^2}{w_0^2}\frac{z_p/z_R}{1+(z_p/z_R)^2}\begin{Bmatrix}0.0366\\0.0525\end{Bmatrix} \end{aligned} \tag{5.18}$$

where $\sin(\arctan(x)) = x/\sqrt{1+x^2}$ and $P_{\mathrm{abs},0} = I_{0,\mathrm{h}}\sigma_{\mathrm{abs}} = P_{0,\mathrm{h}}\sigma_{\mathrm{abs}}/(\pi w_{0,\mathrm{h}}^2)$. This nearly exactly reproduces the result derived in Ref. [113].

5.4 Photothermal Polarizability in Large Particle Limit

In the large particle limit, the scattered field by the photothermal target will contribute appreciably to total signal. Therefore, a core-shell model may be used to approximate the polarizability where the metal nanoparticle is the core, and the shell represents the large thermal lens. The polarizability is therefore [114]

$$\alpha_{\mathrm{pt}} = \frac{1}{3} r_{\mathrm{th}}^3 \frac{(\epsilon_2 - \epsilon_b)[\epsilon_1 q_1 - \epsilon_2(q_1 - 1)] r_{\mathrm{th}}^3 - (\epsilon_1 - \epsilon_2)[\epsilon_2(q_2 - 1) - \epsilon_b q_2] r^3}{[\epsilon_1 q_1 - \epsilon_2(q_1 - 1)][\epsilon_2 q_2 - \epsilon_b(q_2 - 1)] r_{\mathrm{th}}^3 - (\epsilon_1 - \epsilon_2)(\epsilon_2 - \epsilon_b) q_2(q_2 - 1) r^3} \tag{5.19}$$

where r_{th} is the thermal radius equal to radius of the shell, r is the radius of the nanoparticle, ϵ_2 is the dielectric function of the heated background, ϵ_1 is the dielectric function of the metal, and $q_i = \frac{1}{3} x_i^2 - i\frac{2}{3} x_i^3$ ($x_i = 2\pi r_i / \lambda_{\mathrm{p}}$, $r_1 = r, r_2 = r_{\mathrm{th}}$) are the depolarization factors proposed in Ref. [115] to account for retardation effects. The derivative on α with respect to refractive index is expanded as:

$$\frac{d\alpha}{dn}\Big|_{T=T_0} = \frac{d\alpha}{dn_1}\frac{dn_1}{dT}\Big|_{T=T_0} + \frac{d\alpha}{dn_2}\frac{dn_2}{dT}\Big|_{T=T_0} \tag{5.20}$$

The resulting terms in the photothermal signal according to Eq. 5.2 are:

$$\begin{aligned}
\Phi_{\mathrm{int}\left\{\substack{\sin\\\cos}\right\}} =& \frac{4(1 - \sin^2\theta\cos^2\phi)}{w_0^2\sqrt{1 + (z_p/z_R)^2}} k \mathrm{Im}\Big[e^{-i\arctan(-z_p/z_R)} \frac{1}{\tau}\int_0^\tau \Big(\alpha_{\mathrm{pt},T_0}^* + \\
& \qquad \frac{d\alpha_{\mathrm{pt}}^*}{dT}\Big|_{T_0} T_{\mathrm{avg}}(t)\Big)\begin{Bmatrix}\sin\Omega t\\ \cos\Omega t\end{Bmatrix} dt\Big] \\
=& \frac{4(1 - \sin^2\theta\cos^2\phi)}{w_0^2\sqrt{1 + (z_p/z_R)^2}} k \mathrm{Im}\Big[e^{-i\arctan(-z_p/z_R)} \frac{d\alpha_{\mathrm{pt}}^*}{dT}\Big|_{T_0}\Big] \frac{P_{\mathrm{h},0}\sigma_{\mathrm{abs}} r_{\mathrm{th}}^2}{w_{\mathrm{h},0}^2 V_{\mathrm{th}}\kappa}\begin{Bmatrix}0.0366\\ 0.0525\end{Bmatrix}
\end{aligned} \tag{5.21}$$

$$\begin{aligned}\Phi_{\mathrm{sca}\left\{\substack{\sin\\\cos}\right\}} =& \frac{(1-\sin^2\theta\cos^2\phi)^2}{z_R^2+z_p^2}k^4\frac{1}{\tau}\int_0^\tau \left|\alpha_{\mathrm{pt},T_0}+\frac{d\alpha_{\mathrm{pt}}}{dT}\Big|_{T_0}T_{\mathrm{avg}}(t)\right|^2\begin{Bmatrix}\sin\Omega t\\\cos\Omega t\end{Bmatrix}dt\\ =& \frac{(1-\sin^2\theta\cos^2\phi)^2}{z_R^2+z_p^2}k^4\Bigg(2\mathrm{Re}\Big[\alpha^*_{\mathrm{pt},T_0}\frac{d\alpha_{\mathrm{pt}}}{dT}\Big|_{T_0}\Big]\frac{P_{\mathrm{h},0}\sigma_{\mathrm{abs}}r_{\mathrm{th}}^2}{w_{\mathrm{h},0}^2V_{\mathrm{th}}\kappa}\begin{Bmatrix}0.0366\\0.0525\end{Bmatrix}+\\ &\qquad\qquad\left|\frac{d\alpha}{dT}\Big|_{T_0}\right|^2\frac{(P_{\mathrm{h},0}\sigma_{\mathrm{abs}})^2r_{\mathrm{th}}^4}{w_{\mathrm{h},0}^4V_{\mathrm{th}}^2\kappa^2}\begin{Bmatrix}0.0183\\0.0263\end{Bmatrix}\Bigg)\end{aligned} \tag{5.22}$$

5.5 Results & Discussion

The incorporation of a scattering metal complicates the photothermal signal. For small particles, the photothermal signal served as an approximate absorption cross-section measurement. However, the non-negligible scattering contribution to the total signal in larger particles starts to invalidate this approximation. Fig. 5.2a demonstrates when these consequence begin to take effect. The black trace is the photothermal signal post-lockin, Φ as defined in Eq. 5.1. The blue and red traces are calculated by adding the sine and cosine terms together in Eqs. 5.21 and 5.22, respectively. The Mie absorption and scattering cross-sections ($l = 10$) for the room-temperature gold spheres in glycerol of the corresponding radius are overlaid in the shaded gray and purple. The two dashed lines indicate the peak of the Mie cross-sections. In the first row, the heating laser wavelength is varied, and the probe wavelength is kept fixed, at 685 nm. For small particles, the total photothermal signal nearly exactly tracks the absorption cross-section. However, once the particle begins to scatter appreciably, 40-50 nm radii, the scattering portion of the photothermal signal begins to dominate over the interference portion (i.e., the red trace is greater in magnitude than blue trace). At r=50 nm, the total photothermal signal still has a bump at the absorption resonance, however the signal at lower wavelengths is drastically larger than that the absorption cross section. This is because in Eqs. 5.21 - 5.22, the only terms that vary along the x-axis are the absorption cross section of the nanoparticle, σ_{abs}, and the waist of the heating beam, $w_{\mathrm{h},0}$. Notice that the scattering term, Φ_{sca} has both a linear and quadratic dependency on

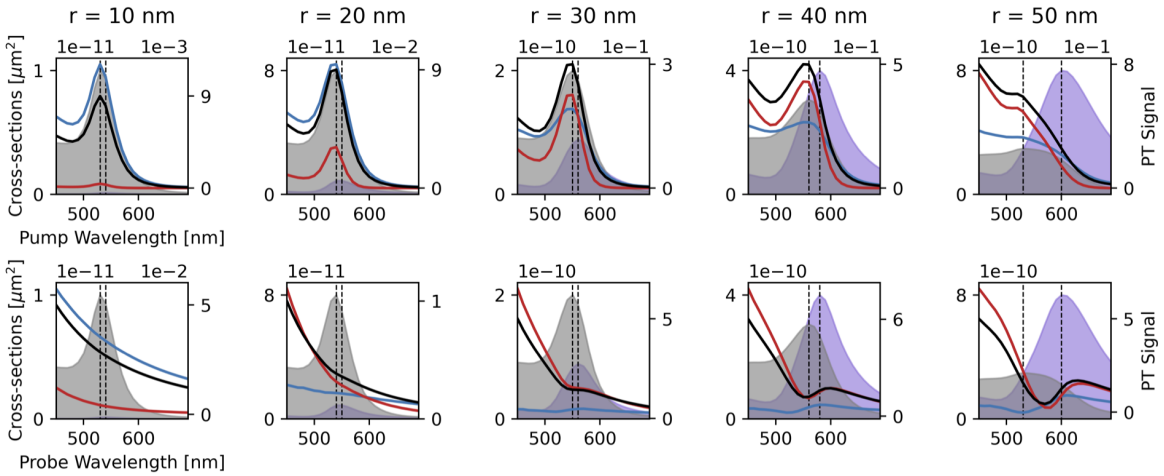

Figure 5.2: Photothermal spectra of the core-shell model with retardation of gold spheres of radius from 10 nm to 50 nm. The photothermal signal (post-lockin), Φ is evaluated in the far-field on the optical axis ($\theta = 0$, $\phi = 0$). The black and purple shaded regions are the Mie absorption and scattering cross-sections, respectively. The black trace is the total photothermal signal, while the blue and red traces are the sum of the sine and cosine parts of the Φ_{int} and Φ_{sca}. The z_p value is picked at each wavelength to maximize the total signal, as is what is approximately done in experiment. The heating beam power of these calculations is set to 500μW. (a) Heating beam wavelength is varied while the probe beam wavelength is held constant at 685 nm. (b) Probe beam wavelength is varied while the heating beam wavelength is fixed at 532 nm.

$\sigma_{\text{abs}}/w_{\text{h},0}^2$. As $\Phi_{\text{sca}} > \Phi_{\text{int}}$, the quadratic term begins to influence the structure of the spectra more heavily at the lower wavelengths. Thus, even for particles at 50 nm in radius, the photothermal signal deviates from the Mie absorption cross-section at wavelengths around the LSP resonance.

While photothermal spectra varying the heating beam wavelength is a common experiment, it is rare to study the photothermal signal as a function of probe wavelength. In this case, many terms in Eqs. 5.21 - 5.22 are varied. Fig. 5.2b demonstrates this by varying the probe wavelength while the heating beam wavelength is kept fixed at 532 nm. For small particles, no peaks are observed because the signal is dominated by the thermal lens, which as no resonances in the optical spectrum. However as the nanoparticles begin to scatter more,

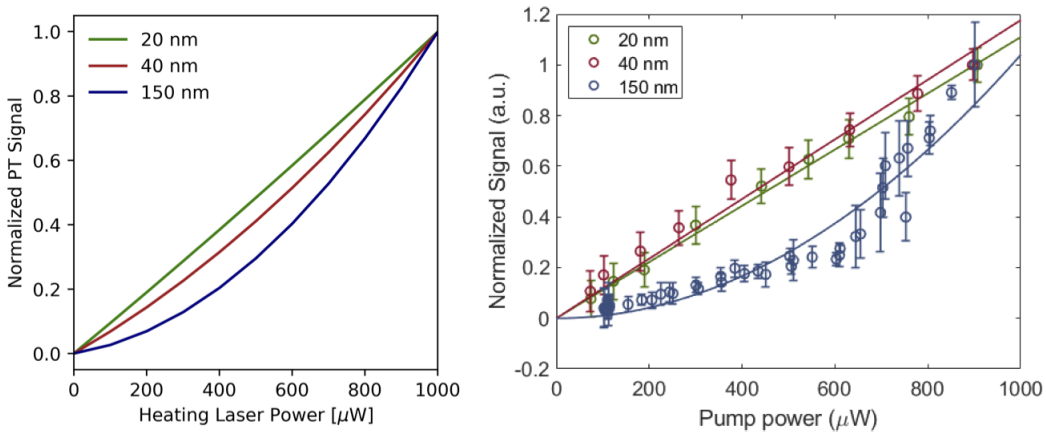

Figure 5.3: Normalized photothermal signals as a function of heating laser power dependency for 20 nm (green), 40 nm (red), and 150 nm (blue) diameter gold spheres. For 20 nm and 40 nm diameter spheres, the relationship between the heating laser power and the normalized photothermal signal is linear in both theory and experiment. However as seen in Fig. 5.2, for larger particles Φ_{sca} becomes non-negligible and as predicted in Eqs. 5.21 - 5.22, when $Phi_{\text{sca}} \not\approx 0$, the dependency of the signal on the heating power becomes nonlinear. This is verified theoretically and experimentally in the 150 nm diameter traces.

starting around r = 30 nm, it is clear that a peak begins to grow in around the scattering Mie resonance. As the particle increases in size, the peak in the photothermal signal red shifts due to the complicated nature of Eqs. 5.21 - 5.22.

The relative dominance of Φ_{sca} compared to Φ_{int} brings into question how the photothermal signal changes with respect to the heating beam's power. Recent work [106] which does account for the scattering term in the photothermal signal performed a heating beam power measurement which demonstrated that even for large particles, the dependence of the photothermal signal on the power of the heating beam is linear. However, when this study is performed over a much greater range in powers, this dependence becomes nonlinear. Fig. 5.3a shows the calculated total photothermal signal as a function of heating beam power. For small particles, the relationship is linear. However for large particles, this trend becomes non-linear. This is as expected due to the linear plus quadratic power dependency in Eq. 5.22 and the observation in Fig. 5.2 that the scattering term in the photothermal signal

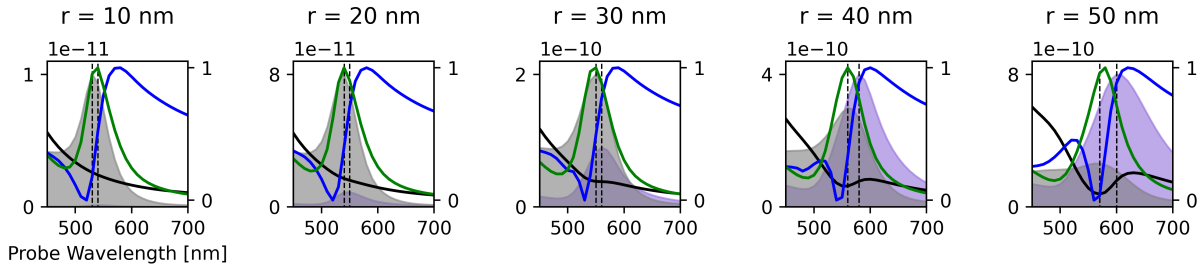

Figure 5.4: A comparison between COBRI and photothermal spectroscopies. The shaded gray and purple regions are the Mie $l = 1$ absorption and scattering, respectively, with the dashed lines indicating the peaks. The green trace is the scattering intensity, the blue trace is the COBRI spectra, and the black trace is the photothermal spectra.

dominates for large particles.

A companion experiment performed in similar conditions is shown in Fig. 5.3b. In order to ensure accuracy of the experiment, each of the heating power data points were taken by selecting a random power. (I.e., the photothermal signal was not collected by sweeping the heating power from lowest to highest.) To ensure the particles were not damaged from exposure to the high powers, the lower power values were measured again after the particles had been exposed to the high powers. This verified that the same signal was measured before and after exposure to the higher powers and that the particles were not damaged. Additional microscope image analysis was performed to ensure the images did not change before and after measurements. As observed in theory, the experimental data shows that for small particles, the photothermal signal has a linear dependence on heating beam power. For larger particles, this dependence becomes nonlinear. The traces are linear fits for the small particles, and a fit of a linear term plus a quadratic term for the large particle.

Lastly, a theoretical comparison between different microscopy techniques is performed to compare how well photothermal imaging holds up against other similar scattering microscopies. Fig. 5.4 shows photothermal spectra against Mie theory at $l = 1$, confocal COBRI,

and the core-shell dipole scattering intensity.

$$\begin{aligned} I_{\text{sca}} &= \frac{cn_b}{8\pi}|\mathbf{E}_{\text{sca},T_0}|^2 \\ I_{\text{COBRI}} &= \frac{cn_b}{8\pi}\big(2\text{Re}[\mathbf{E}_{\text{p}} + \mathbf{E}_{\text{sca},T_0}] + |\mathbf{E}_{\text{sca},T_0}|^2\big) \end{aligned} \tag{5.23}$$

where $\mathbf{E}_{\text{sca},T_0} = \mathbf{G}(\mathbf{x}) \cdot \alpha_{\text{pt},T_0}\mathbf{E}_{\text{np}}(\mathbf{x})$. For comparison, the photothermal signal can be approximated as (see Appendix F):

$$I_{\text{pt}} = \frac{cn_b}{8\pi}\big(|\mathbf{E}_{\text{sca},T_{\max}}|^2 - |\mathbf{E}_{\text{sca},T_0}|^2 + 2\text{Re}\big(\mathbf{E}^*_{\text{sca},T_{\max}} - \mathbf{E}^*_{\text{sca},T_0}\big)\big) \tag{5.24}$$

In the above expression, the lockin integral has been evaluated and all fields are time independent. $\mathbf{E}_{\text{sca},T_{\max}}$ is the field scattered by the core-shell polarizability when the heating beam is maximum, or $t = 0$. This approximation is only valid when the modulation frequency, Ω, is small.

While there are absorptive effects occurring in the photothermal measurement, Fig. 5.4 shows that this experiment is able measure the scattering resonance approximately as well as the COBRI experiment. Both the photothermal spectra and the COBRI spectra cannot detect the scattering resonance for small particles and deviate strongly from the scattering spectra for all nanoparticle sizes at low wavelengths. Despite no lockin procedure and no modulated heating beam, the spectra resulting from both experiments are quite similar.

5.6 Conclusion

A new model, closely related to prior effective dipole models, has been derived to account for the scattering effects of large nanoparticles in the photothermal imaging experiment. It is verified that photothermal spectroscopy may be used to approximate absorption spectroscopy for small particles when the heating beam wavelength is varied and the probe wavelength is held constant. For larger particles, however, the lower wavelengths deviate significantly from the absorption cross section. Oppositely, for small particles, varying the probe wavelength

does not reproduce a scattering spectrum. However for larger particles, the approximate location of the scattering resonance can be inferred from the photothermal spectrum. A nonlinear heating beam power dependency for large, scattering particles is predicted by the model and verified experimentally. Lastly, the model developed in this work is used to compare the differences between photothermal and COBRI experiments. Both methods perform similarly with respect to scattering, while COBRI cannot be used for absorption (because it does not have a heating beam).

Recently, researchers have installed modulated heating beams within COBRI and iSCAT experiments [106, 116, 117]. These may be considered photothermal measurements, and they are often in wide-field geometries. The theories developed herein are only valid for confocal microscopes. While the images produced by wide-field and confocal microscopes may seem similar, the spectra resulting from the two approaches are very different [10]. Further studies should be done to compare the differences between confocal and wide-field photothermal spectroscopy experiments.

5.7 Acknowledgments

This work was supported by the U.S. National Science Foundation under Grants NSF CHE-1727092 (D.J.M), CHE1727122 (S.L.), and CHE-1728340 (K.A.W.). S.L. also acknowledges support from the Robert A. Welch Foundation (Grant C-1664). The experimental work was conducted in part using resources of the Shared Equipment Authority at Rice University. The theoretical work was facilitated through the use of advanced computational, storage, and networking infrastructure provided by the Hyak supercomputer system at the University of Washington.

Part III

ELECTRON MICROSCOPIES AND SPECTROSCOPIES FOR NANOSCIENCE CHARACTERIZATION

Part III of this dissertation shifts to another microscopy and spectroscopy technique, electron energy loss spectroscopy (EELS). These electron microscopy and spectroscopy approaches are markedly different from the photothermal microscopy discussed in Part II, and other light-based techniques. The following published manuscript is presented in this Part:

- Chapter 6: **West, C.***, Olafsson, A.*, Pakeltis, G., Garfinkel, D., Rack, P., Masiello, D., Camden, J., & Idrobo, J. Plasmon hybridization in nanorhombus assemblies. *J. Phys. Chem. C.* 124, 49, 27009-27016 (2020). [13]

* indicates co-first authorship

Chapter 6

PLASMON HYBRIDIZATION IN NANORHOMBUS ASSEMBLIES

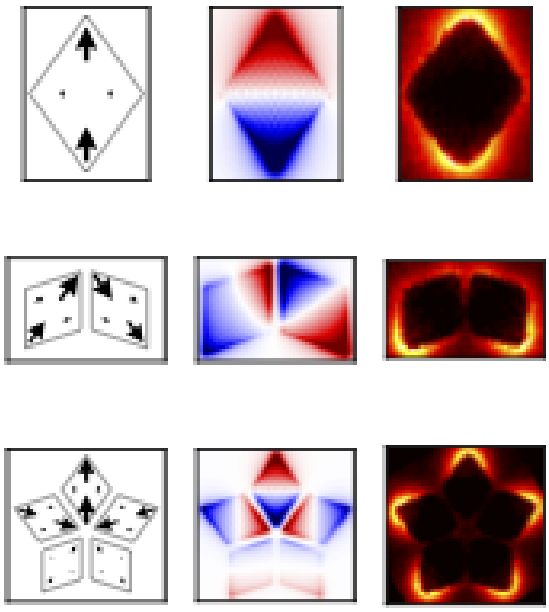

Reprinted with permission from:

West, C.,* Olafsson, A.,* Pakeltis, G., Garfinkel, D., Rack, P., Masiello, D., Camden, J., & Idrobo, J. Plasmon hybridization in nanorhombus assemblies. *J. Phys. Chem. C.* 124, 49, 27009-27016 (2020).

6.1 Abstract

Understanding resonant coupling in plasmonic nanoassemblies is a challenging scientific endeavor, especially for particles with complex nanoarchitectures. Our ability to both model and measure this optical behavior, however, has rapidly developed in the last 20 years via a confluence of fabrication, spectroscopy, and theoretical analysis. Here we precisely nanofabricate, characterize, and model the coupling and infrared optical responses of different plasmonic nanorhombus assemblies. Ranging from a monomer to a pentamer ensemble, experimental and simulated point spectra, spectrum images, and near-field maps agree well with the results of an analytical coupled normal mode model developed here. The analytical model reveals that the infrared optical responses of the nanorhombus systems can be explained by the coupling of the major and minor axis dipole and a quadrupole localized surface plasmon modes arising from the individual nanorhombus monomers. This model can be used to predict the plasmonic behavior of more complicated systems, and it elucidates the role that short-, intermediate-, and far-field coupling effects play in extended plasmonic assemblies more generally. This work also highlights how localized electron probes in the new generation of monochromated aberration-corrected scanning transmission electron microscopes can be used to study the optical responses of nanofabricated assemblies in the infrared spectral regime.

6.2 Introduction

Over the past several decades significant effort has been invested to characterize the localized surface plasmon (LSP) resonances in noble metal nanoparticle assemblies [118, 119, 120, 121]. LSP resonances are geometry-specific collective oscillations of the free conduction-band electrons in a metal. They offer the unique ability to capture far-field light and convert it to intense surface-bound electric fields, effectively focusing light in systems below the diffraction limit[26, 27]. There have been numerous studies demonstrating the high sensitivity of the LSP to its local environment, including the nanoparticle shape [122], proximity to other

particles [123], substrate [124, 125], and other chemical and physical aspects of the system [126, 127]. Each of these considerations, however, also presents an opportunity to control the LSP energy, typically in the near-infrared to ultraviolet range, making LSPs excellent candidates for uses in biological/chemical sensing [128, 129], waveguiding [130], catalysis [131, 132], and in optoelectronic devices [133, 134].

The unique optical properties of nanoparticle assemblies are determined by the coupled and hybridized LSPs of the individual particles that comprise the assembly[26, 27]. Many studies have examined how interparticle LSP coupling is affected by varying the particle size [135], particle shape [136], inter-particle distance [137], and environment [138, 139, 140, 141]. These analyses are often limited to ensemble material properties because diffraction-limited optical methods are unable to resolve nanometer scale phenomena. Near-field optical scanning microscopy [142, 143, 144] and scanning transmission electron microscopy (STEM) [145, 146, 147], however, have the ability to study the long and short range coupling of LSP modes with both nanometer spatial resolution and high energy resolution. Yet even with these techniques, most of the studies have been concentrated on nanostructures that have simple geometries such as spheres, disks, and rods because their plasmonic properties are easier to interpret and to model.

In this Chapter, we use high spatial and energy resolution in monochromated aberration-corrected STEM, combined with theoretical modeling, to study the evolution of plasmon coupling in nanostructures with more complex geometries. Using electron energy-loss (EEL) spectroscopy in STEM, we identify the spatial and energy profile of a single plasmonic nanorhombus and study the LSP evolution as more nanorhombi couple to it. Using this approach we also develop a theoretical model based on the normal modes of coupled dipoles to study and predict the LSP hybridization profiles of coupled assemblies. This simplified model not only allows for the interpretation of both the experimental and simulated results presented herein, but also lays the foundation for understanding plasmonic coupling in much larger plasmonic assemblies that are not computationally tractable with standard numerical Maxwell equation solvers.

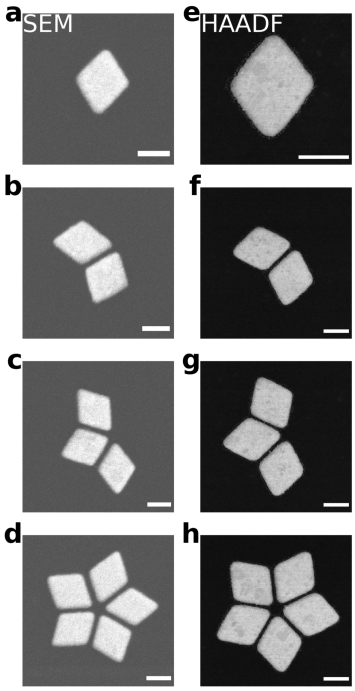

Figure 6.1: Post-fabrication SEM images (a-d) show consistent fabrication across the sample. HAADF images of similar structures (e-h) taken at the time of measurements confirm the high fidelity of the fabricated nanorhombi. Scale bar corresponds to 200 nm.

6.3 Results & Discussion

Fig. 6.1 shows the set of Au nanorhombus assemblies used to build our understanding of plasmon coupling, beginning with a single oblong, kite-like rhombus monomer (Fig. 6.1a,e), and ending in a 5-pointed star-like pentamer (Fig. 6.1d,h). This approach requires structures with low geometric tolerances in order to ensure that any measurable differences are due to particle interactions, not particle heterogeneity. The representative scanning electron microscope (SEM) images (Fig. 6.1a-d) of the as-fabricated nanorhombi and the high-angle annular dark-field (HAADF) images (Fig. 6.1e-h) of the as-measured nanorhombi show good fidelity. This demonstrates that the samples underwent almost no degradation after fabrication. A minimal amount of corner rounding is observed. Each nanorhombus was designed to have a thickness of 20 nm with an edge length of 250 nm, yielding a long and a short axis length of 400 nm and 300 nm, respectively. A 20 nm gap distance was chosen as smaller gaps had slight inconsistencies.

The EEL point spectra (Fig. 6.2a) of the nanorhombus monomer highlight the importance of understanding the spatial distribution of LSP resonance energies. The green and blue traces in Fig. 6.2a represent the EEL spectra collected near the end of one of the long axis and short axis positions, respectively (see inset). Both point spectra show an identical peak labeled Q at 1250 meV. However, the two lower energy peaks in the spectra are clearly different, one occurring at 800 meV (L, green trace), and the other at 1000 meV (S, blue trace). Electron-driven discrete dipole approximation (e-DDA) simulations[148] were performed and the resulting e-DDA spectra (dashed) show similar peaks when the impact parameter is in the same position as the experimentally acquired data, set to be 10 nm away from the particle corners. The simulated nanorhombus was modeled with rounded corners to approximate the experimentally fabricated particles. All simulations of the nanorhombi were calculated in vacuum. The silicon nitride substrate present in the experiment has no resonances and is dispersionless in the energy range measured. Thus, the only effect the substrate will have on the nanorhombus is an overall red shift of the resonances due to the

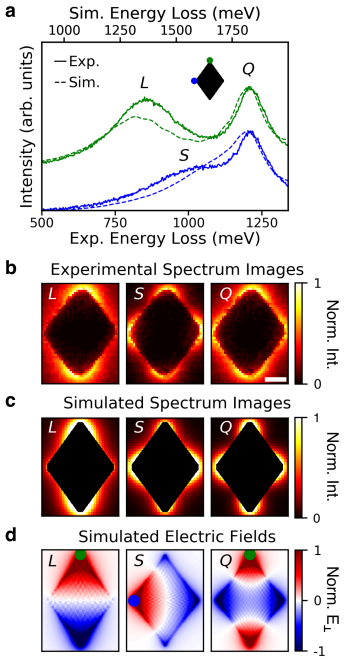

Figure 6.2: EEL point spectra (a), spectrum images (b-c), and simulated electric field maps (d) of an isolated nanorhombus show the three dominant lowest energy modes of the system: a long axis dipole L, a short axis dipole S, and a quadrupole Q. Experimental (solid, bottom x-axis) and full-wave electrodynamic simulations (dashed, top x-axis) of the EEL spectra are obtained at two different electron beam positions (as schematically shown by the colored circles in the inset). The intensity and energy loss of the simulated spectra have been rescaled (top x-axis) to account for substrate effects, which were not present in simulation. The calculated S peak (at $\sim$ 1000 meV) is located at a higher energy than the experiment. Since the peak is broad and weak, it appears as a vague shoulder in the simulation and it is not as clearly resolved as in the experiment. Experimental (b) and simulated (c) spectrum images were taken by rastering the electron beam across the nanorhombus and collecting the energy lost at each point over a narrow energy window spanning the resonance. Scale bar size is 100 nm and the experimental spectrum image energy window is 100 meV (centered at the energy values denoted in each panel). The normal component of the electric fields (d) calculated at the three dominant resonances show the dipole / quadrupole orientations at each mode.

image effect. While in specific scenarios the presence of a substrate causes non-negligible plasmonic interactions[149, 150, 151], this is not the case for silicon nitride in this energy window. The thin silicon nitride substrate has a near uniform refractive index of $n = 2.1$ in the studied energy range, and will not cause any mode mixing or appreciable linewidth broadening.

The identification of the LSP resonances are confirmed by collecting spectrum images at each peak (Fig. 6.2b-c). In these measurements, the electron beam is rastered over the sample area and an EEL spectrum is collected at each electron probe position. Each recorded spectrum is energy aligned and normalized to the zero loss peak maximum, no further processing was performed (i.e., denoising). An energy window of 100 meV was used to obtain the spectrum images, which is approximately five times the energy resolution of the experiment and therefore sufficient to identify the individual LSP modes observed in this study. The experimental (Fig. 6.2b) and simulated (Fig. 6.2c) images show that the two lowest energy modes L and S are dipolar LSPs, and the higher energy mode Q is a quadrupolar LSP. It is clear then that the longer axis dipole LSP is shifted lower in energy due to the elongated shape (400 nm diameter versus 300 nm diameter). Simulated electric field maps (Fig. 6.2d) of the normal component of the electric field evaluated on a plane parallel to and 4 nm above the surface of the nanorhombus further validate the identity of the modes. The electron beam positions that drive each mode are labeled on the maps. Note that the electric field map of the short axis excitation in Fig. 6.2d is not symmetric because the electron beam probe is driving a linear combination of both the short axis dipole and quadrupole modes as they overlap spectrally (see Fig. 6.2a).

A useful approach for understanding the hybridization schemes of coupled nanorhombi is to study the eigenmodes or normal modes of the assembly. Normal modes are independent of driving field, yet allows for the interpretation of peaks in the spectra. Numerical software for calculating eigenmodes exists[152, 153], however, we use a course-grained modeling scheme to reduce the dimensionality of the calculations. There are numerous reduced-order procedures for modeling coupled plasmonic nanoparticles [154, 155, 156, 157]. The semi-analytic

approach presented here expands upon previous work[156, 157] on cornered nanoparticles. Past work demonstrated that the optical responses of such nanoparticles could be modeled with coupled dipoles localized at the corners of the nanoparticle. However, what the previous models do not account for is how to use this course-graining procedure to accurately quantify interparticle coupling. In this work, we use a similar course-grained modeling scheme to approximate the lowest energy modes of the rhombus monomer as generalized normal mode oscillators and use them to accurately describe the rhombus-rhombus coupling in different nanorhombus assemblies.

Using a single nanorhombus, we build the model by placing x-oriented and y-oriented dipole oscillators inside the four corners of a nanorhombus as shown in Fig. 6.3a. Each symmetrically equivalent dipole oscillator is assigned a unique radius, which dictates its effective mass, damping rate, and resonance frequency[115]. All eight dipoles couple according to $g_{ij} = e^2 \hat{\mathbf{q}}_i \cdot \mathbf{\Lambda}_{ij} \cdot \hat{\mathbf{q}}_j$ where $\hat{\mathbf{q}}_i$ is the unit vector of the i^{th} dipole, and $\mathbf{\Lambda}_{ij} = \Big[(3\hat{\mathbf{n}}_{ij}\hat{\mathbf{n}}_{ij} - \mathbf{1})/r_{ij}^3 - ik/r_{ij}^2(3\hat{\mathbf{n}}_{ij}\hat{\mathbf{n}}_{ij} - \mathbf{1}) - k^2/r_{ij}(\hat{\mathbf{n}}_{ij}\hat{\mathbf{n}}_{ij} - \mathbf{1})\Big]e^{ir_{ij}k}$ is the dipole relay tensor where r_{ij} is the distance between dipoles i and j, $\hat{\mathbf{n}}_{ij}$ is the unit vector in the r_{ij} direction, and k is the wave vector. The coupled equations of motion become

$$m_i\ddot{q}_i + m_i\gamma_i\dot{q}_i + m_i\omega_{0i}^2 q_i - \sum_{j\neq i}^{N} g_{i,j}q_j = 0, \tag{6.1}$$

where $N = 8$ for the eight oscillators, q_i is the amplitude, m_i is effective mass, γ_i is the radiative and nonradiative damping, and ω_{0i} is the resonance frequency of the i^{th} oscillator. Solving Eq. (6.1) results in eight normal modes that can be used to predict all possible LSP resonances of the nanorhombus. By fitting the three lowest energy eigenmodes and eigenvalues of Eq. (6.1) to the simulated field maps (Fig. 6.2d), resonance frequencies, and damping rates extracted from the simulated spectra, dipole positions and radii for the coupled dipole model are determined. These fits are accurate to within 30 meV of the simulated EEL spectra of the nanorhombus. The three predicted modes (L, S, Q) are shown in Fig. 6.3b where the black arrows indicate the dipole orientations and magnitudes at the given energy

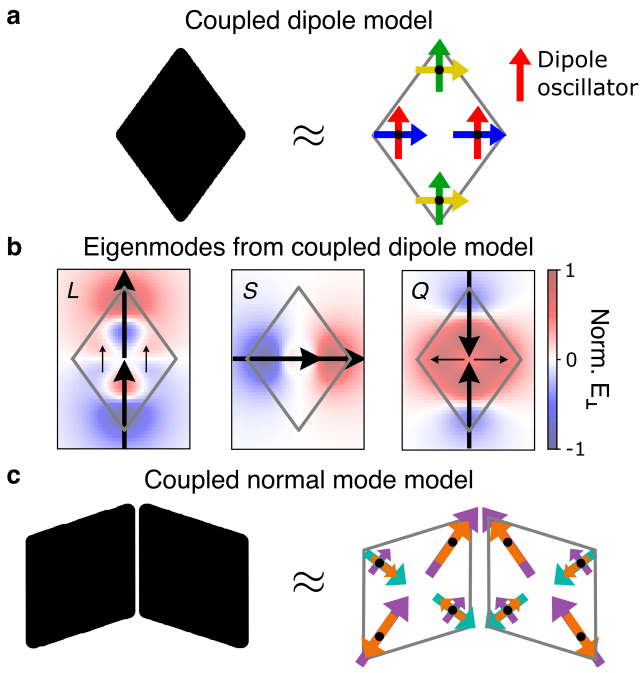

Figure 6.3: Illustration of the coupled dipole model (a-b) and coupled normal mode model (c) used to approximate the optical response of nanorhombus assemblies. The coupled dipole model (a) consists of eight unique dipole oscillators placed near the corners of the nanorhombi. The positions and polarizabilities of each dipole are determined by fitting the three lowest eigenmodes and eigenenergies of Eq. (6.1) to the simulated field maps, resonance frequencies, and damping rates of the long axis dipole (L), short axis dipole (S), and quadrupole (Q) in Fig. 6.2. Each dipole with the same color is assigned the same polarizability. The resulting three lowest eigenmodes (b) are used to build the coupled normal mode model (c) where each nanorhombus is instead assigned three generalized oscillators representing the three lowest energy modes (purple: long axis dipole L, turquoise: short axis dipole S, orange: quadrupole Q.) The overlayed electric field maps in (b) are the fields of the sphere dipoles evaluated in a plane parallel to and 60 nm above the dipoles.

and phase. The normal component of the electric fields produced by each dipole oscillator are overlaid for ease in comparison to Fig. 6.2d. Agreement between Fig. 6.3b and Fig. 6.2d reflects the coupled dipole model and the fit parameters (radii and dipole positions) accurately account for the optical response of an individual nanorhombus.

However, the coupled dipole model will not suffice in modeling the rhombus-rhombus interactions primarily because the coupling among the corner-located dipoles on each nanorhombus will be overestimated. Instead, the dipole orientations, mode energies, and damping rates of the three lowest energy eigenmodes (L, S, Q) from the coupled dipole model are used to parameterize generalized normal mode oscillators. This new model is depicted in Fig. 6.3c where each colored arrow corresponds to one of the normal modes (purple: long axis dipolar LSP, turquoise: short axis dipolar LSP, orange: quadrupolar LSP.) The equations of motion become

$$m\ddot{x}_\mu + m\gamma_\mu \dot{x}_\mu + m\omega_{0\mu}^2 x_\mu - \sum_{\nu \neq \mu} \sum_{i,j} \frac{q_{\mu i}}{\bar{q}_\mu} g_{\mu i,\nu j} x_\nu = 0, \tag{6.2}$$

where the Greek indices refer to the generalized normal mode coordinates, and the Latin indices refer to the comprising corner-located dipoles. x_μ is the oscillator coordinate of one of the three normal modes on each particle, m is a geometric mass assigned to each normal mode, and $\omega_{0\mu}$ and γ_μ are the real and imaginary parts of the eigenvalue from the coupled dipole model. The pairwise coupling between the nanorhombi is defined by taking a weighted sum of the dipole-dipole coupling among all corner-located dipoles where $\bar{q}_\mu = \sum_i q_{\mu i}/N$.

We demonstrate the efficacy of the model by comparing it to experimental and e-DDA simulated spectra, spectrum images, and field maps of a nanorhombus dimer. The EEL spectra acquired at four unique electron beam positions of the coupled dimer are shown in Fig. 6.4a. The spatial configuration of the six eigenmodes predicted by the analytic model are shown in Fig. 6.4b. The normal modes have been vertically aligned with the corresponding simulated electric fields (Fig. 6.4c-d) and experimental spectrum images (Fig. 6.4e) taken at each resonance position. Arrows have been drawn on the simulated electric

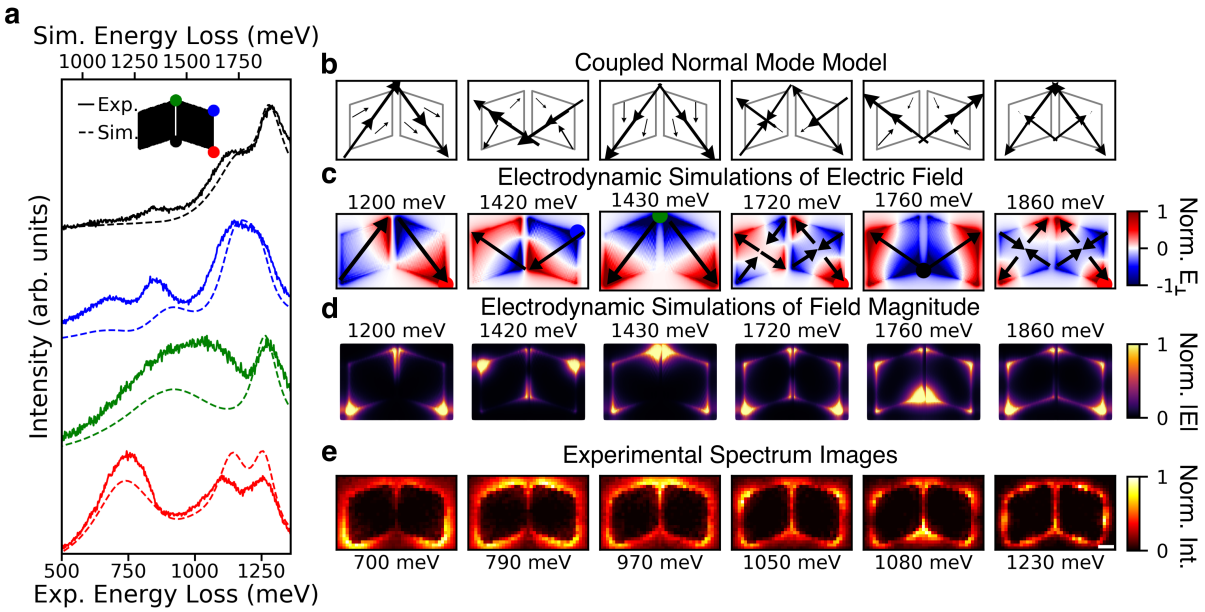

Figure 6.4: Simulated (dashed, top x-axis) and experimental (solid, bottom x-axis) EEL spectra (a) were taken at four different positions of a nanorhomus dimer as illustrated schematically by the colored circles in the inset. The coupled normal mode analysis procedure was used to predict the eigenmodes of the dimer (b) by approximating each rhombus as the three lowest energy modes predicted by the conventional coupled dipole theory. Simulated electric field maps (c) taken at the indicated beam positions and energies show all six hybridized modes of the coupled nanorhombi that were predicted by the normal mode model. Arrows representing the total dipole moments from the field maps are overlaid on (c) to aid in the comparison with (b). Agreement between the predicted eigenmodes and the simulated field maps demonstrate the utility of the coupled normal mode model. The magnitude of the field maps (d) can be compared to the experimental spectrum images (e) to show that theory, simulation, and experiment are in agreement. The scale bar corresponds to 50 nm and the experimental spectrum image energy window is 100 meV (centered at the energy values denoted in each panel).

field maps to facilitate comparison between the simulated maps and the modes obtained from the analytical model. The agreement between the *e*-DDA simulations and experiment with the analytical model shown in Fig. 6.4b-e demonstrates that the optical responses of the coupled nanorhombi system can be well described by the coupled normal mode model developed here.

The corroboration of the analytic model allows for the interpretation of the spectra in Fig. 6.4a. The two lowest energy normal modes are the head-to-tail aligned hybridized long axis dipoles (700 meV) and short axis dipoles (790 meV). The dipoles are best driven when the electron beam is positioned on either corner of the outer edges of the nanorhombus dimer, and they show up as the lowest energy peaks in the spectra (red and blue circles in the inset of Fig. 6.4a). The complements of the long axis and short axis hybridized modes (tail-to-tail) are driven most strongly when the electron beam is located at the two corners of the edges shared by the two nanorhombi (green and black circles in the inset of Fig. 6.4a). Lastly, the quadrupole hybridization is best observed when the electron beam is located at the outer corners of the longest axes (red spectra), with the two highest energy peaks showing the signature peak splitting of the head-to-tail and tail-to-tail modes.

The three particle coupled nanorhombus assembly (Fig. 6.5a-d) and a highly symmetric five particle coupled assembly (Fig. 6.5e-h) offer two additional systems to study the hybridization schemes. As with Fig. 6.4, simulated and experimental point spectra were taken at different beam positions (labeled with color circles in the inset). While the theoretical model predicts nine possible normal modes for the trimer and fifteen normal modes for the pentamer, only the five shown in each system are resolvable. The other normal modes are inaccessible because of the near degeneracy and spectral overlap within the energy resolution of the data. Nevertheless, a clear indication of the hybridization between the long axis dipole LSP, short axis dipole LSP, and quadruple LSP are observed. Once again, the point spectra as well as the spectrum images have LSP resonances that are highly sensitive to the host geometry and near-field coupling behavior.

A subset of the predicted normal modes (Fig. 6.5b,g) are aligned with the simulated

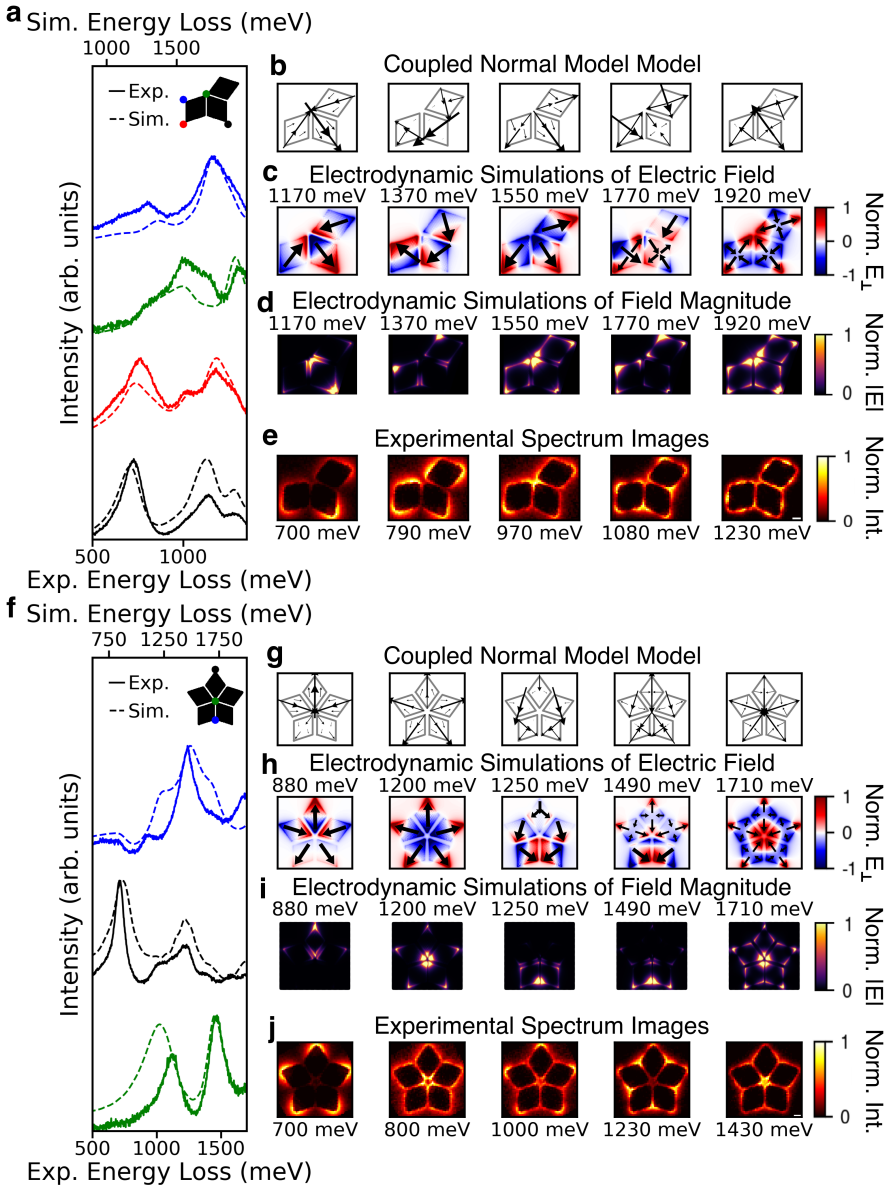

Figure 6.5: Normal mode analysis of the trimer (a-d) and pentamer (e-h) show hybridization of the long axis dipole, short axis dipole, and quadrupole. (a,e) Simulated (dashed, top x-axis) and experimental (solid, bottom x-axis) spectra were taken at the beam positions labeled in the inset. Of the normal modes predicted by the coupled normal mode model, only the five shown in (b,f) can be resolved in the spectra. The simulated electric fields (c,g) exactly correspond to the predicted eigenmodes. The experimental spectrum images (d,h) were taken at the corresponding energies and further validate the identities of the hybridized modes. Scale bar size is 50 nm and the experimental spectrum image energy window is 100 meV (centered at the energy values denoted in each panel).

electric field maps (Fig. 6.5c-d, h-i) and experimental spectrum images (Fig. 6.5 e,j) of each resonance. Similar to the dimer, the three lowest energy modes of the trimer, as measured experimentally, are the head-to-tail long axis (700 meV), head-to-tail short axis (790 meV), and tail-to-tail long axis (970 meV) hybridized modes. However contrary to the dimer, the next energy mode (1080 meV) is not clearly an all-long axis, all-short axis, or all-quadrupole hybridization scheme. Instead, it is a mixture of the short axis and quadruple modes and is accessible at all electron beam positions. The field profiles on each nanorhombus are also mixing between the short axis and quadrupole orientations. Furthermore, while the tail-to-tail quadrupole clearly exists (1230 meV), the head-to-tail hybridization appears as a predicted normal mode but does not arise as an isolated feature in the spectra. This is due to the spectral overlap of the all-quadrupole and quadrupole-quadrupole-short axis modes, where the latter mode dominates.

Similar to the trimer, the pentamer also supports five resolvable normal modes that were predicted by the analytic model. The two lowest energy modes, as measured experimentally, are the long axis dipole hybridized into the head-to-tail (700 meV) and all tail-to-tail (800 meV) arrangements. In this case, there are not any observable all short-axis dipole modes, and instead only combinations arising from short axis dipole-quadrupole coupling. Similar to the trimer, however, the analytic model does predict a head-to-tail all-short axis mode arrangement, but it is again not resolvable due to the overlap of the third mode presented here. Lastly, the all-quadrupole tail-to-tail mode is once again present (1430 meV) and easily excitable when the electron beam is positioned at the center of the pentamer.

6.4 Conclusions

In conclusion, our work demonstrates the ability to precisely nanofabricate nanorhombus assemblies, characterize their plasmonic properties, and model the interparticle coupling across a variety of arrangements. As we build from a monomer to a pentamer, the experimental and simulated point spectra, spectrum images, and near-field maps agree well with the coupled normal mode model developed here. We observe that the infrared optical responses

of coupled nanorhombus systems can be explained by coupling among the nanorhombus' two dipolar and one quadrupolar LSP modes. By examining these different assemblies, we see that the head-to-tail arrangement of the long axis dipoles always yields the lowest energy hybrid peak observed in the spectra. Therefore, we predict that examining low-energy hybrid modes across heterogeneous nanorhombus structures can be greatly simplified by measuring along this axis. Similarly, the all-quadrupole tail-to-tail modes lie higher in energy and are easily excitable and resolvable at the same probe positions. However, in the mid-range energy window the short axis dipole and the quadrupole LSPs mix on the particles themselves, and across the hybridized normal mode itself.

The simple coupled normal mode model presented here is able to quantitatively predict the plasmon modes of the nanorhombus across a wide range of energies and spatial distributions. We expect the model will help further guide experiments and data analysis even when examining larger and more extended nanorhombus assemblies. Additionally, the analytical model can be reparameterized with different monomer sizes and shapes to quickly predict the normal modes and energies of other coupled systems. This offers the ability to easily explore the plasmonic responses of many other corner-dominated nanoparticle arrangements. While in this work we studied the near-field coupling and hybridization effects of cornered nanoparticle clusters, the approach shown here can furthermore be applied to study the role of short- intermediate-, and far-field coupling effects in extended plasmonic assemblies.

6.5 Methods

6.5.1 Experimental Fabrication/Characterization

The deconstructed rhombuses are fabricated via electron-beam lithography (JEOL 9300FS) using a lift-off process. A 300 μm Si wafer with 30 nm of low pressure chemical vapor deposited SiNx is spin coated with PMMA 495 A4 and exposed. The pattern is then developed using methyl isobutyl ketone:isopropyl alcohol (IPA) (1:3). 25 nm of Au is sputter deposited via DC magnetron sputtering onto the substrate followed by soaking in

a heated NMP bath, sonicating in NMP and acetone, and rinsing with IPA and deionized water. The backside of the wafer is then spin coated with P20 and S1818 and exposed using photolithography to create the windows of the TEM. Reactive ion etching is used to remove the backside nitride layer and the wafer is subsequently submerged in a heated KOH bath to etch the Si windows and TEM grid edges.

6.5.2 Experimental STEM-EELS

EEL spectra in the infrared regime were collected using a Nion aberration-corrected high energy resolution monochromated EELS-STEM (Nion HERMES^{TM}) operating at 60 kV accelerating voltage. Point spectra and spectrum images were collected with convergence semiangle of 30 mrad and collection semiangle of 20 mrad, with a beam current of $\sim$ 10 pA [158, 159, 160]. Scattered electrons were dispersed in a Nion Iris spectrometer at 2 meV/channel and the energy resolution (full width half maximum of the Zero Loss Peak) was approximately 16 meV. Point spectra had their ZLP maxima normalized to unity and their background subtracted.

6.6 Acknowledgments

C.A.W. and D.J.M. acknowledge the support by the U.S. Department of Energy (DOE), Office of Science, Office of Basic Energy Sciences (BES), Materials Sciences and Engineering Division under Award DE-SC0018040. The numerical simulations were facilitated through the use of advanced computational, storage, and networking infrastructure provided by the Hyak supercomputer system at the University of Washington. J.P.C. and A.O. acknowledge the Department of Energy (DOE), Office of Science, Office of Basic Energy Sciences (BES), Materials Sciences and Engineering Division under Award DE-SC0018169. A.O. also acknowledges the HERE program at Oak Ridge National Laboratory. The authors acknowledge that the plasmonic structures were synthesized, and the EELS measurements were conducted at the Center for Nanophase Materials Sciences, which is a DOE Office of Science User Facility. P.D.R. and G.P. acknowledge NSF DMR-1709275 which supported

the experimental synthesis. G.P. also acknowledges supplemental support via a fellowship sponsored by the Center for Materials Processing at the University of Tennessee.

Part IV

NANOSCIENCE EDUCATION

The last chapter of this dissertation is a pivot from the content in the preceding chapters. Last year, I designed a virtual nanoscience summer camp geared towards middle to high school students. I created the lesson plans, selected the materials to be mailed to students for at-home experimentation, I assembled these kits, and taught the camp three times in July and August 2021. The motivation for the summer camp was to increase student's science identity and knowledge of nanoscience to inspire them to continue in their math and science courses to perhaps pursue a science career. To access whether or not the summer camp had an impact on the students, I conducted the following study described in Ch. 7. This in preparation publication will be submitted to an education journal, e.g. ACS's Journal of Chemical Education.

Chapter 7

ACCESSING THE IMPACT OF A VIRTUAL NANOSCIENCE SUMMER CAMP ON MIDDLE - HIGH SCHOOL STUDENTS' ENGAGEMENT WITH CONTENT AND SCIENCE IDENTITY

7.1 Introduction

A significant body of research has investigated the well-documented need for a diverse science workforce [161, 162, 163, 164]. As a result, universities, industries, and government agencies invest in a considerable amount of resources towards kindergarten through twelfth grade (K-12) outreach programs [165, 166] with the purpose of increasing interest and engagement in science in students at a young age. These enrichment programs may be formal or informal. Informal science education comprises science-related experiences which occur outside of the classroom, including museum / aquarium visits, summer camps, and after school programs. These out-of-classroom learning experiences present opportunities for combating the systemic discrimination faced by underrepresented populations of students [167, 168]. Yet, sometimes the students who would benefit the most from these programs do not have access to them for a variety of reasons including their geographic location, parent / guardian engagement, and accessibility [169]. For example, K-12 students who live near research universities will be more exposed to science outreach compared to students who live and go to school far away from universities. If not addressed, this may compound equity-related issues by continuing to provide "science capital" to the same populations of students [170].

One emergent opportunity which may address this problem is offering students virtual learning experiences accompanied with kits containing materials to perform at-home science experiments. Many traditional informal science education programs began to offer this in response to the stay-at-home orders issued due to the COVID-19 pandemic. Inadvertently,

this enabled students in the aforementioned environments access to new science learning opportunities. The onset of these new programs must be accompanied by careful assessments on impact these programs have on the students and their relationships to science.

A new program for middle to high school students was created at the University of Washington (UW) in 2021 to inspire students with inquiry-based nanoscience lessons and experiments. This program, *NanoCamp!*, was a five-day virtual summer camp which ran for three hours each day. It was designed and taught by graduate students at UW with desired outcomes to 1) increase student's perception of their science identity, and 2) engage with and understand core concepts of nanoscience. As defined in Ref. [171], science identity is seeing oneself as a scientist. It results from competence in scientific content, performance of scientific practices, and recognition by oneself and others as a "science person". Science identity is constantly renegotiated depending on a person's environment [172]. Fostering a student's science identity has been shown to serve as a good metric for whether students will persist in science.[173, 174]

The purpose of this study is to access the impact *NanoCamp!* had on the participating students. Specifically, the research questions are:

1. To what extent did *NanoCamp!* impact the students' science identity?

2. Did *NanoCamp!* increase the students' knowledge of nanoscience?

Two instruments are used to answer the above questions. The first instrument is a Likert-style science identity pre- and post-survey developed in Ref. [175]. The second instrument uses some questions from Ref. [176], and some questions specifically written for the program. There additionally were three free response / reflection questions written specifically for *NanoCamp!* that the students answered about their experience in *NanoCamp!* that day.

Lesson	Nanoscience Content	Hands On
Experiment with Nanomaterials	Size & Shape	Yes
Model of an Atom	Size & Shape	No
Lithography: Methods to Make Nanomaterials	Size & Shape	Yes
Make a Spectroscope	Size & Shape	Yes
Virtual Lab Experience	Size & Shape	No
Strength of Structures with Origami	Structure of Matter	Yes
Meet a Researcher (2)	Size & Shape	No
Model of Carbon Allotropes	Structure of Matter	Yes
Observations of the Electromagnetic Force	Forces & Interactions	Yes
Thin Film Interferences	Forces & Interactions	Yes

Table 7.1: Lessons taught during *NanoCamp!*

7.2 Methods

7.2.1 Format

NanoCamp! was conducted over Zoom in July and August 2021. The program involved multiple hands-on activities, experiments, and inquiry-based lessons. The experiments and activities are listed in Table 7.2.1. The students answered the nanoscience and science identity pre-surveys before nanoscience instruction or on the first day of the program. During the five days, the students and instructors all together performed experiments using their at-home kits. They were asked to present their data either by unmuting to speak, turning on their video, or communicating through the chat feature. At the end of the second, third, and fourth day, the students anonymously answered the free response questions. On the last day, the post-surveys were administered and the students were given time to answer the questions.

7.2.2 Participants

Fifty-nine students located in the United States and Canada participated in *NanoCamp!*. The program was taught to three different groups of students. The first group consisted of

a class of nineteen ninth- and tenth-grade students who participated in UW's GEAR UP Achievers program (Gaining Early Awareness & Readiness for Undergraduate Programs) in South King County. Approximately half of the students participated by logging into the Zoom summer program while sitting together in one room. Although technically in person, the students primarily interacted through Zoom and not in-person. The remainder of the GEAR UP participants attended the program at a personal residence.

The last two groups of students participated in *NanoCamp!* through Youth and Teen Programs hosted by UW Continuum College. These forty students were primarily located across Washington state, with two students outside of Washington. All attended classes remotely at a personal residence, and were in sixth through eighth grade.

All students participated in this study, though some did not fill out all surveys or all questions in the surveys. This did not impact their experience in the program. Student responses had keys assigned to each survey which allowed pre- and post-survey responses to be matched without breaking anonymity. This research study was registered through UW's Human Subject Division Institutional Review Board STUDY00013671. After review, it was determined that this study presented "No greater than minimal risk" and was therefore declared exempt.

7.2.3 Instrumentation

The impact of *NanoCamp!* on the participants' science identity and nanoscience knowledge was investigated using a combination of two surveys and free response questions. All instruments are reproduced in Appendix G.

The science identity instrument was developed in Ref. [175] to evaluate the impact of an informal education experience on middle school students' science identity. The instrument was specifically designed to be short with minimal classroom disruption. In addition, the instrument offers a quantitative resource for evaluating science identity, while many others are qualitative. The instrument relies on the three constructs of science identity: competence, performance, and recognition [171]. Each construct has five questions associated with it. The

questions are asked on a Likert scale.

The nanoscience content instrument was designed specifically for this program. Part of the questions came from Ref. [176], while others were created by the instructor. Unlike the science identity instrument, this instrument was not rigorously tested for reliability or validity. It consists of fifteen true / false and multiple choice questions on some of the core concepts of nanoscience: size / shape / scale, structure of matter, and forces and interactions. Five questions were asked for each core concept.

7.3 Results & Discussion

The data collected from the science identity surveys is shown in Figure 7.3. Each panel contains the data from the pre- and post-survey results from all *NanoCamp!* participants for a single question. The title of the panel labels the question, where all questions are displayed on the right with their label. The students had the option to select the following choices in response to each question: "Strongly agree" (blue), "Agree" (green), "Neutral" (yellow), "Disagree" (orange), and "Strongly disagree" (red). The numbers overlaid on each bar section indicate the number of participants who selected the corresponding answer to the labelled question. All data has been included; i.e., the data from students who did not entirely complete both the pre- and post- surveys has been included.

Table 7.3 includes the means and standard deviations of the pre- and post- survey data for each question from Figure 7.3. "Strongly disagree" is coded to equal 1, "Disagree" is assigned 2, up to "Strongly agree" equal to 5. The difference between the means of the pre- and post-surveys from each question may be used to understand the impact *NanoCamp!* had on the participants. For the competence construct, each of the five questions had an increase in mean value after the program (Mean Pre $-$ Mean Post < 0), suggesting that participants felt more competent in science after participating in the program. Similarly, for each question in the performance construct, the mean post-survey increased from the pre-survey. However, for the recognition construct, two out of the five questions had a larger mean value in the pre-survey compared to the post-survey. The two questions are: "When

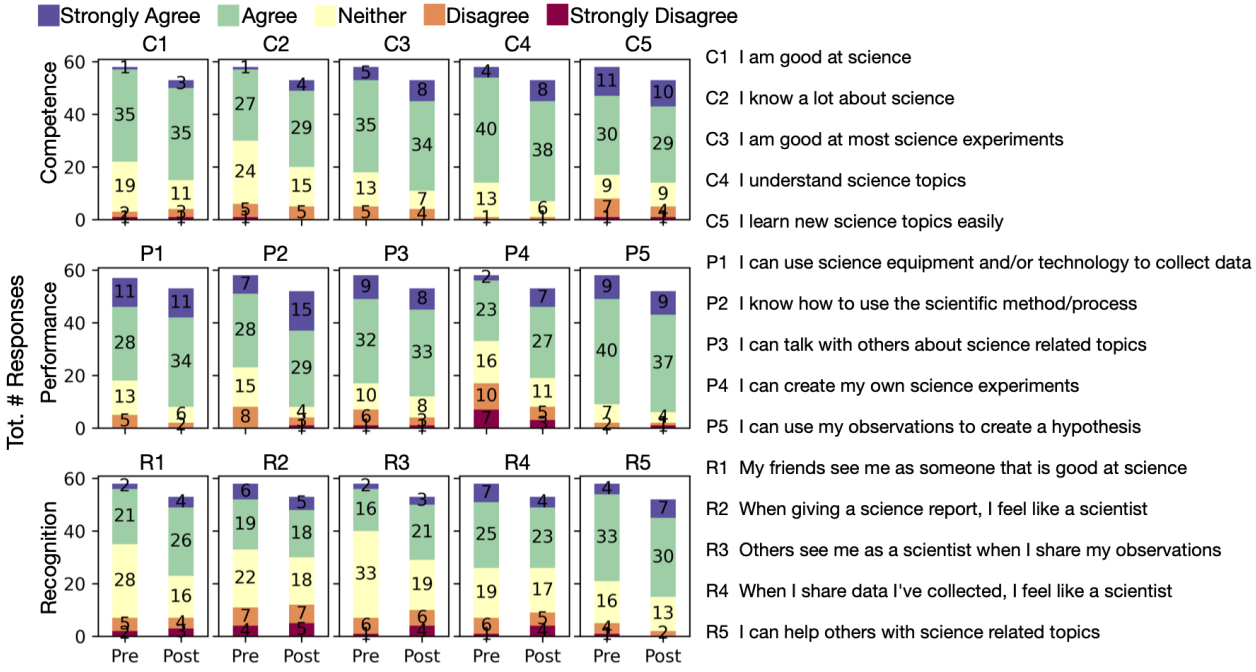

Figure 7.1: Total pre- and post-survey Likert data from the science identity instrument. Each row contains the results from each construct: competence (row 1), performance (row 2), and recognition (row 3). The numbers overlaid on the charts indicate the total number of responses in each category. The categories range from "Strongly Agree" (blue) to "Strongly Disagree (red), as indicated in the legend. No data was excluded from this analysis. The students who only filled out one out of the two surveys were included in this data set, which explains the fewer data in the post-survey column. The questions corresponding to each data set are listed on the right. Table 7.3 contains the descriptive statics corresponding to this data.

	C1		C2		C3		C4		C5	
	Mean	SD.	Mean	SD.	Mean	SD.	Mean	SD.	Mean	SD.
Pre	3.57	0.68	3.38	0.75	3.69	0.75	3.81	0.58	3.74	0.97
Post	3.68	0.75	3.60	0.77	3.87	0.76	4.00	0.59	3.81	0.90
	P1		**P2**		**P3**		**P4**		**P5**	
	Mean	SD.	Mean	SD.	Mean	SD.	Mean	SD.	Mean	SD.
Pre	3.79	0.86	3.59	0.88	3.72	0.91	3.05	1.10	3.97	0.65
Post	4.02	0.69	4.04	0.88	3.83	0.83	3.57	1.03	4.00	0.71
	R1		**R2**		**R3**		**R4**		**R5**	
	Mean	SD.	Mean	SD.	Mean	SD.	Mean	SD.	Mean	SD.
Pre	3.28	0.81	3.28	1.04	3.21	0.74	3.53	0.90	3.60	0.79
Post	3.45	0.95	3.21	1.10	3.25	1.00	3.34	1.02	3.81	0.72

Table 7.2: Descriptive statistics of Likert scale science identity data.

giving a science report, I feel like a scientist", and "When I share data I've collected, I feel like a scientists." The data indicates that the participants felt *less* like a scientist when giving a science report and sharing their data.

	Mean	**Std. Dev.**	**SEM**	**Lower**	**Upper**	**t**	**df**	**Sig.**
Total	-2.479	5.35	0.77	-4.03	-0.93	-3.21	47	0.002
Competence	-0.813	2.16	0.312	-1.440	-0.185	-2.606	47	0.012
Performance	-1.46	2.475	0.36	-2.177	-0.740	-4.082	47	0
Recognition	-0.208	2.63	0.38	-0.97	0.55	-0.548	47	0.586

Table 7.3: Paired sample t-tests comparing the pre- survey and post-survey data. C.V. for df = 47 is 2.012. The students' reported total science identity increased with a statistically significant value. This resulted from increased of the students competence and performance. However, the data shows that the students did not experience a statistically significant change in the recognition construct.

To further explore these findings, paired-sample t-tests were performed on the subset of the data where every pre-survey response could be connected to a post-survey response using SPSS. The advantage of using this test is that it is performed by matching each participant's pre- and post-survey data, which can indicate the change each student individually had by participating in *NanoCamp!*. To match the pre-surveys to the post-surveys, data had to be excluded. This reduced the data set to 48 responses. The results of this test are shown in Table 7.3. In this test, the five questions for each construct have been grouped together. The mean is calculated by taking the average of the differences between pre-survey data and post-survey data from each student. A negative mean indicates that the pre-survey was less than the post-survey, i.e., the participants' science identity increased after the nanoscience program. The column labeled 'Std. Dev.' is the standard deviation between the data. 'SEM' stands for the standard error mean, which is calculated by dividing the standard deviation by the square root of the sample size. 'Lower' and 'Upper' are the lower and upper 95% confidence interval of difference. 't' is the t-value for the paired-sample t test. 'df' is the degrees of freedom. 'Sig.' is the p-value with df degrees of freedom.

For the competence and performance constructs, a statistically significant increase in the participants' identity is measured. This is because the lower and upper 95% confidence interval of difference have the same sign, the t value is greater than 2.012 (calculated from df= 47), and Sig. (2-tailed), the p-vale, is ¡ 0.05. However, even though recognition has a negative mean (indicating a positive intervention), the lower / upper values have different signs, the t values is > 2.012, and Sig. (2-tailed) is > 0.05. Therefore, while the competence and performance constructs increased after *NanoCamp!*, there is no statistically significant change in the recognition construct.

	Mean	Std. Dev.	SEM	Lower	Upper	t	df	Sig.
Total	-.511	2.06	0.31	-1.13	0.11	-1.66	44	0.104

Table 7.4: Paired sample t-tests comparing the pre- and post-surveys. C.V. for df = 47 is 2.012. The results from the instrument and data analysis indicate that the students' nanoscience knowledge did not change with any statistical significant.

The data resulting from the nanoscience content instrument is displayed in Table 7.3. By the sign difference between the lower / upper confidence interval values, the t value greater than 2.012, and Sig. or p value ¿ 0.05, no statistically significant change in the students' nanoscience knowledge can be claimed. This could either be because the instrument had not been validated and tested for reliability, or it could be because the participants did not measurably learn nanoscience content.

7.4 Conclusion

In conclusion, the participants' science identity increased after attending *NanoCamp!*, but there was no statistically significant change in their nanoscience education. The students experienced an increase in competence and performance, yet not recognition. This could be explained due to the virtual environment of the program making the students feel less-recognized than maybe they would have in an in-person environment. Given the question breakdown, it's suggested that more effort should be put into encouraging students to share data. This is a difficult task to do virtually, made worse when the majority of students can only interact with video and audio off. From the collected data, it seems the students' nanoscience knowledge did not increase. This could be because the instrument did not accurately test for a middle to high school students' nanoscience knowledge.

Future studies similar to this one would benefit from the creation of a validated and reliable nanoscience content instrument. Without a tested instrument, drawing conclusions from the data is difficult. Furthermore, additional post-survey should be administered one

to six months after the program to test whether the changes observed immediately following the program persisted once the students are in different environments.

BIBLIOGRAPHY

[1] Jay M Enoch. History of mirrors dating back 8000 years. *Optom. Vis. Sci.*, 83(10):775–781, 2006.

[2] John Weiner and Frederico Nunes. *Light Matter Interaction: Physics and Engineering at the Nanoscale*. Oxford Scholarship Online, 2017.

[3] F. David Peat. *Infinite Potential: The Life and Times of David Bohm*. Basic Books, 1997.

[4] Rufus H Ritchie. Plasma losses by fast electrons in thin films. *Phys. Rev.*, 106(5):874, 1957.

[5] CJ Powell and JB Swan. Effect of oxidation on the characteristic loss spectra of aluminum and magnesium. *Phys. Rev.*, 118(3):640, 1960.

[6] Sheldon Schultz, David R Smith, Jack J Mock, and David A Schultz. Single-target molecule detection with nonbleaching multicolor optical immunolabels. *PNAS*, 97(3):996–1001, 2000.

[7] C Sönnichsen, S Geier, NE Hecker, G Von Plessen, J Feldmann, H Ditlbacher, B Lamprecht, JR Krenn, FR Aussenegg, V ZH Chan, et al. Spectroscopy of single metallic nanoparticles using total internal reflection microscopy. *Appl. Phys. Lett.*, 77(19):2949–2951, 2000.

[8] Mustafa Yorulmaz, Sara Nizzero, Anneli Hoggard, Lin-Yung Wang, Yi-Yu Cai, Man-Nung Su, Wei-Shun Chang, and Stephan Link. Single-particle absorption spectroscopy by photothermal contrast. *Nano Lett.*, 15(5):3041–3047, 2015.

[9] Phillip A Reinhardt, Abigail P Crawford, Claire A West, Gabe DeLong, Stephan Link, David J Masiello, and Katherine A Willets. Toward quantitative nanothermometry using single-molecule counting. *The Journal of Physical Chemistry B*, 2021.

[10] Seyyed Ali Hosseini Jebeli, Claire A West, Stephen A Lee, Harrison J Goldwyn, Connor R Bilchak, Zahra Fakhraai, Katherine A Willets, Stephan Link, and David J Masiello. Wavelength-dependent photothermal imaging probes nanoscale temperature differences among subdiffraction coupled plasmonic nanorods. *Nano Lett.*, 2021.

[11] Rashad Baiyasi, Harrison J Goldwyn, Lauren A McCarthy, Claire A West, Seyyed Ali Hosseini Jebeli, David J Masiello, Stephan Link, and Christy F Landes. Coupled-dipole modeling and experimental characterization of geometry-dependent trochoidal dichroism in nanorod trimers. *ACS Photonics*, 8(4):1159–1168, 2021.

[12] Grace Pakeltis, Enzo Rotunno, Siamak Khorassani, David A Garfinkel, Robyn Collette, Claire A West, Scott T Retterer, Juan Carlos Idrobo, David J Masiello, and Philip D Rack. High spatial and energy resolution electron energy loss spectroscopy of the magnetic and electric excitations in plasmonic nanorod oligomers. *Optics Express*, 29(3):4661–4671, 2021.

[13] Claire A West, Agust Olafsson, Grace Pakeltis, David A Garfinkel, Philip D Rack, David J Masiello, Jon P Camden, and Juan Carlos Idrobo. Plasmon hybridization in nanorhombus assemblies. *J. Phys. Chem. C*, 124(49):27009–27016, 2020.

[14] Ujjal Bhattacharjee, Claire A West, Seyyed Ali Hosseini Jebeli, Harrison J Goldwyn, Xiang-Tian Kong, Zhongwei Hu, Elliot K Beutler, Wei-Shun Chang, Katherine A Willets, Stephan Link, et al. Active far-field control of the thermal near-field via plasmon hybridization. *ACS Nano*, 13(8):9655–9663, 2019.

[15] Xiaoyu Cheng, Taryn P Anthony, Claire A West, Zhongwei Hu, Vignesh Sundaresan, Aaron J McLeod, David J Masiello, and Katherine A Willets. Plasmon heating pro-

motes ligand reorganization on single gold nanorods. *The journal of physical chemistry letters*, 10(6):1394–1401, 2019.

[16] Grace Pakeltis, Zhongwei Hu, Austin G Nixon, Eva Mutunga, C Praise Anyanwu, Claire A West, Juan Carlos Idrobo, Harald Plank, David J Masiello, Jason D Fowlkes, et al. Focused electron beam induced deposition synthesis of 3d photonic and magnetic nanoresonators. *ACS Applied Nano Materials*, 2(12):8075–8082, 2019.

[17] Charles Cherqui, Yueying Wu, Guoliang Li, Steven C Quillin, Jacob A Busche, Niket Thakkar, Claire A West, Nicholas P Montoni, Philip D Rack, Jon P Camden, et al. Stem/eels imaging of magnetic hybridization in symmetric and symmetry-broken plasmon oligomer dimers and all-magnetic fano interference. *Nano letters*, 16(10):6668–6676, 2016.

[18] J. Jackson. *Classical Electrodynamics*. Wiley, New York NY, 1999.

[19] Martin G Blaber, Matthew D Arnold, and Michael J Ford. A review of the optical properties of alloys and intermetallics for plasmonics. *J. Condens. Matter Phys.*, 22(14):143201, 2010.

[20] Peter B Johnson and R-WJPrB Christy. Optical constants of the noble metals. *Phys. Rev. B*, 6(12):4370, 1972.

[21] Edward D Palik. *Handbook of optical constants of solids*, volume 3. Academic press, 1998.

[22] Kevin M McPeak, Sriharsha V Jayanti, Stephan JP Kress, Stefan Meyer, Stelio Iotti, Aurelio Rossinelli, and David J Norris. Plasmonic films can easily be better: rules and recipes. *ACS Photonics*, 2(3):326–333, 2015.

[23] Mark W Knight, Nicholas S King, Lifei Liu, Henry O Everitt, Peter Nordlander, and Naomi J Halas. Aluminum for plasmonics. *ACS Nano*, 8(1):834–840, 2014.

[24] Emilie Ringe. Shapes, plasmonic properties, and reactivity of magnesium nanoparticles. *J. Phys. Chem. C*, 124(29):15665–15679, 2020.

[25] Krystyna Kolwas and Anastasiya Derkachova. Impact of the interband transitions in gold and silver on the dynamics of propagating and localized surface plasmons. *Nanomaterials*, 10(7):1411, 2020.

[26] Stefan Alexander Maier. *Plasmonics: fundamentals and applications*. Springer Science & Business Media, 2007.

[27] Craig F Bohren and Donald R Huffman. *Absorption and scattering of light by small particles*. John Wiley & Sons, 2008.

[28] Amirmostafa Amirjani and Sayed Khatiboleslam Sadrnezhaad. Computational electromagnetics in plasmonic nanostructures. *J. Mater. Chem. C*, 2021.

[29] Bruce T Draine and Piotr J Flatau. Discrete-dipole approximation for scattering calculations. *J. Opt. Soc. Am. A*, 11(4):1491–1499, 1994.

[30] Kevin C. Smith. *Theoretical Models of Hybrid Light-Matter Systems and Their Applications*. PhD thesis, University of Washington, 2021.

[31] Charles Cherqui, Nicholas W Bigelow, Alex Vaschillo, Harrison Goldwyn, and David J Masiello. Combined tight-binding and numerical electrodynamics understanding of the stem/eels magneto-optical responses of aromatic plasmon-supporting metal oligomers. *ACS Photonics*, 1(10):1013–1024, 2014.

[32] Nicholas P Montoni, Steven C Quillin, Charles Cherqui, and David J Masiello. Tunable spectral ordering of magnetic plasmon resonances in noble metal nanoclusters. *ACS Photonics*, 5(8):3272–3281, 2018.

[33] Christopher L Baldwin, Nicholas W Bigelow, and David J Masiello. Thermal signatures

of plasmonic fano interferences: toward the achievement of nanolocalized temperature manipulation. *J. Phys. Chem. Lett.*, 5(8):1347–1354, 2014.

[34] Sandra P Sanchez-Rodriguez, Jeremy P Sauer, Sarah A Stanley, Xi Qian, Andrew Gottesdiener, Jeffrey M Friedman, and Jonathan S Dordick. Plasmonic activation of gold nanorods for remote stimulation of calcium signaling and protein expression in hek 293t cells. *Biotechnol. Bioeng.*, 113(10):2228–2240, 2016.

[35] Michael J Caterina, Mark A Schumacher, Makoto Tominaga, Tobias A Rosen, Jon D Levine, and David Julius. The capsaicin receptor: a heat-activated ion channel in the pain pathway. *Nature*, 389(6653):816–824, 1997.

[36] Jeff DeFalco, Mark Tomishima, Hongyan Liu, Connie Zhao, XiaoLi Cai, Jamey D Marth, Lynn Enquist, and Jeffrey M Friedman. Virus-assisted mapping of neural inputs to a feeding center in the hypothalamus. *Science*, 291(5513):2608–2613, 2001.

[37] Ali Ghoreyshi and RH Victora. Optical modeling of media for heat assisted magnetic recording. *Appl. Phys. Lett.*, 108(9):092401, 2016.

[38] Haitian Xu, Ghazal Hajisalem, Geoffrey M Steeves, Reuven Gordon, and Byoung C Choi. Nanorod surface plasmon enhancement of laser-induced ultrafast demagnetization. *Sci. Rep.*, 5(1):1–7, 2015.

[39] Rong Ji, Baoxi Xu, Zhanhong Cen, Ji Feng Ying, and Yeow Teck Toh. Thermal effects on transducer material for heat assisted magnetic recording application. *J. Appl. Phys.*, 117(17):17A918, 2015.

[40] Nan Zhou, Xianfan Xu, Aaron T Hammack, Barry C Stipe, Kaizhong Gao, Werner Scholz, and Edward C Gage. Plasmonic near-field transducer for heat-assisted magnetic recording. *Nanophotonics*, 3(3):141–155, 2014.

[41] Guillaume Baffou, Julien Polleux, Herve Rigneault, and Serge Monneret. Super-heating and micro-bubble generation around plasmonic nanoparticles under cw illumination. *J. Phys. Chem. C*, 118(9):4890–4898, 2014.

[42] Nathaniel J Hogan, Alexander S Urban, Ciceron Ayala-Orozco, Alberto Pimpinelli, Peter Nordlander, and Naomi J Halas. Nanoparticles heat through light localization. *Nano Lett.*, 14(8):4640–4645, 2014.

[43] Oara Neumann, Alexander S Urban, Jared Day, Surbhi Lal, Peter Nordlander, and Naomi J Halas. Solar vapor generation enabled by nanoparticles. *ACS Nano*, 7(1):42–49, 2013.

[44] Zheyu Fang, Yu-Rong Zhen, Oara Neumann, Albert Polman, F Javier Garcia de Abajo, Peter Nordlander, and Naomi J Halas. Evolution of light-induced vapor generation at a liquid-immersed metallic nanoparticle. *Nano Lett.*, 13(4):1736–1742, 2013.

[45] Guillaume Baffou, Romain Quidant, and F Javier Garcia de Abajo. Nanoscale control of optical heating in complex plasmonic systems. *ACS Nano*, 4(2):709–716, 2010.

[46] Guillaume Baffou and Romain Quidant. Thermo-plasmonics: using metallic nanostructures as nano-sources of heat. *Laser Photonics Rev.*, 7(2):171–187, 2013.

[47] Larousse Khosravi Khorashad, Lucas V Besteiro, Zhiming Wang, Jason Valentine, and Alexander O Govorov. Localization of excess temperature using plasmonic hot spots in metal nanostructures: combining nano-optical antennas with the fano effect. *J. Phys. Chem. C*, 120(24):13215–13226, 2016.

[48] Gregory V Hartland. Optical studies of dynamics in noble metal nanostructures. *Chem. Rev.*, 111(6):3858–3887, 2011.

[49] Yun Yu, Kanishka D Wijesekara, Xiaoxing Xi, and Katherine A Willets. Quantifying wavelength dependent plasmonic hot carrier energy distributions at metal semiconductor interfaces. *ACS Nano*, 13(3):3629–3637, 2019.

[50] Jon P Camden, Jon A Dieringer, Yingmin Wang, David J Masiello, Lawrence D Marks, George C Schatz, and Richard P Van Duyne. Probing the structure of single-molecule surface-enhanced raman scattering hot spots. *J. Am. Chem. Soc.*, 130(38):12616–12617, 2008.

[51] Guillaume Baffou, Christian Girard, and Romain Quidant. Mapping heat origin in plasmonic structures. *Phys. Rev. Lett.*, 104(13):136805, 2010.

[52] Khaled Metwally, Serge Mensah, and Guillaume Baffou. Isosbestic thermoplasmonic nanostructures. *ACS Photonics*, 4(6):1544–1551, 2017.

[53] Zachary J Coppens, Wei Li, D Greg Walker, and Jason G Valentine. Probing and controlling photothermal heat generation in plasmonic nanostructures. *Nano Lett.*, 13(3):1023–1028, 2013.

[54] Pablo Albella, Rodrigo Alcaraz de la Osa, Fernando Moreno, and Stefan A Maier. Electric and magnetic field enhancement with ultralow heat radiation dielectric nanoantennas: considerations for surface-enhanced spectroscopies. *ACS Photonics*, 1(6):524–529, 2014.

[55] Guillaume Baffou, Pascal Berto, Esteban Bermudez Urena, Romain Quidant, Serge Monneret, Julien Polleux, and Herve Rigneault. Photoinduced heating of nanoparticle arrays. *ACS Nano*, 7(8):6478–6488, 2013.

[56] Ryoko Shimada, Hitomi Sakai, Jun Yamamoto, and Hiroshi Watanabe. Creation of large, periodic temperature gradient via plasmonic heating from mesoscopic planar lattice of metal domains. *Int. J. Therm. Sci.*, 118:247–258, 2017.

[57] Xin Yan, Guohua Liu, Jinliang Xu, and Shuai Wang. Plasmon heating of one-dimensional gold nanoparticle chains. *Sol. Energy*, 173:665–674, 2018.

[58] Stéphane Berciaud, Laurent Cognet, Gerhard A Blab, and Brahim Lounis. Photothermal heterodyne imaging of individual nonfluorescent nanoclusters and nanocrystals. *Phys. Rev. Lett.*, 93(25):257402, 2004.

[59] Markus Selmke, Marco Braun, and Frank Cichos. Gaussian beam photothermal single particle microscopy. *J. Opt. Soc. Am. A*, 29(10):2237–2241, 2012.

[60] Laurent Cognet, Catherine Tardin, David Boyer, Daniel Choquet, Philippe Tamarat, and Brahim Lounis. Single metallic nanoparticle imaging for protein detection in cells. *PNAS*, 100(20):11350–11355, 2003.

[61] Alexander Gaiduk, Paul V Ruijgrok, Mustafa Yorulmaz, and Michel Orrit. Detection limits in photothermal microscopy. *Chem. Sci.*, 1(3):343–350, 2010.

[62] Ying Fang, Wei-Shun Chang, Britain Willingham, Pattanawit Swanglap, Sergio Dominguez-Medina, and Stephan Link. Plasmon emission quantum yield of single gold nanorods as a function of aspect ratio. *ACS Nano*, 6(8):7177–7184, 2012.

[63] Steven C Quillin, Charles Cherqui, Nicholas P Montoni, Guoliang Li, Jon P Camden, and David J Masiello. Imaging plasmon hybridization in metal nanoparticle aggregates with electron energy-loss spectroscopy. *J. Phys. Chem. C*, 120(37):20852–20859, 2016.

[64] Emil Prodan, Corey Radloff, Naomi J Halas, and Peter Nordlander. A hybridization model for the plasmon response of complex nanostructures. *Science*, 302(5644):419–422, 2003.

[65] Mustafa Yorulmaz, Anneli Hoggard, Hangqi Zhao, Fangfang Wen, Wei-Shun Chang, Naomi J Halas, Peter Nordlander, and Stephan Link. Absorption spectroscopy of an individual fano cluster. *Nano Lett.*, 16(10):6497–6503, 2016.

[66] Liane S Slaughter, Wei-Shun Chang, Pattanawit Swanglap, Alexei Tcherniak, Bishnu P Khanal, Eugene R Zubarev, and Stephan Link. Single-particle spectroscopy of gold

nanorods beyond the quasi-static limit: varying the width at constant aspect ratio. *J. Phys. Chem. C*, 114(11):4934–4938, 2010.

[67] Edward M Purcell and Carlton R Pennypacker. Scattering and absorption of light by nonspherical dielectric grains. *Ap. J.*, 186:705–714, 1973.

[68] Jon S Donner, Guillaume Baffou, David McCloskey, and Romain Quidant. Plasmon-assisted optofluidics. *ACS Nano*, 5(7):5457–5462, 2011.

[69] Harsha Reddy, Urcan Guler, Alexander V Kildishev, Alexandra Boltasseva, and Vladimir M Shalaev. Temperature-dependent optical properties of gold thin films. *Opt. Mater. Express*, 6(9):2776–2802, 2016.

[70] Yun-Ling Luo, Yi-Syun Shiao, and Yu-Fen Huang. Release of photoactivatable drugs from plasmonic nanoparticles for targeted cancer therapy. *ACS Nano*, 5(10):7796–7804, 2011.

[71] Jibin Song, Jiajing Zhou, and Hongwei Duan. Self-assembled plasmonic vesicles of sers-encoded amphiphilic gold nanoparticles for cancer cell targeting and traceable intracellular drug delivery. *J. Am. Chem. Soc.*, 134(32):13458–13469, 2012.

[72] Hyung Joon Kim, Sun-Mi Lee, Kyu-Hyung Park, Chin Hee Mun, Yong-Beom Park, and Kyung-Hwa Yoo. Drug-loaded gold/iron/gold plasmonic nanoparticles for magnetic targeted chemo-photothermal treatment of rheumatoid arthritis. *Biomaterials*, 61:95–102, 2015.

[73] Xiaohua Huang, Prashant K Jain, Ivan H El-Sayed, and Mostafa A El-Sayed. Plasmonic photothermal therapy (pptt) using gold nanoparticles. *J. Lasers Med. Sci.*, 23(3):217–228, 2008.

[74] Joseph R Cole, Nikolay A Mirin, Mark W Knight, Glenn P Goodrich, and Naomi J Halas. Photothermal efficiencies of nanoshells and nanorods for clinical therapeutic applications. *J. Phys. Chem. C*, 113(28):12090–12094, 2009.

[75] Surbhi Lal, Susan E Clare, and Naomi J Halas. Nanoshell-enabled photothermal cancer therapy: impending clinical impact. *Acc. Chem. Res.*, 41(12):1842–1851, 2008.

[76] Shaunak Mukherjee, Florian Libisch, Nicolas Large, Oara Neumann, Lisa V Brown, Jin Cheng, J Britt Lassiter, Emily A Carter, Peter Nordlander, and Naomi J Halas. Hot electrons do the impossible: plasmon-induced dissociation of h2 on au. *Nano Lett.*, 13(1):240–247, 2013.

[77] Phillip Christopher, Hongliang Xin, and Suljo Linic. Visible-light-enhanced catalytic oxidation reactions on plasmonic silver nanostructures. *Nat. Chem.*, 3(6):467–472, 2011.

[78] Tianyu Liu and Yat Li. Plasmonic solar desalination. *Nat. Photonics*, 10(6):361–362, 2016.

[79] Mahak Dhiman, Ayan Maity, Anirban Das, Rajesh Belgamwar, Bhagyashree Chalke, Yeonhee Lee, Kyunjong Sim, Jwa-Min Nam, and Vivek Polshettiwar. Plasmonic colloidosomes of black gold for solar energy harvesting and hotspots directed catalysis for co2 to fuel conversion. *Chem. Sci.*, 10(27):6594–6603, 2019.

[80] WA Challener, Chubing Peng, AV Itagi, D Karns, Wei Peng, Yingguo Peng, XiaoMin Yang, Xiaobin Zhu, NJ Gokemeijer, Y-T Hsia, et al. Heat-assisted magnetic recording by a near-field transducer with efficient optical energy transfer. *Nat. Photonics*, 3(4):220–224, 2009.

[81] Daniel O'Connor and Anatoly V Zayats. The third plasmonic revolution. *Nat. Nanotechnol.*, 5(7):482–483, 2010.

[82] Shantha Vedantam, Hyojune Lee, Japeck Tang, Josh Conway, Matteo Staffaroni, and Eli Yablonovitch. A plasmonic dimple lens for nanoscale focusing of light. *Nano Lett.*, 9(10):3447–3452, 2009.

[83] Kosei Ueno, Satoaki Takabatake, Yoshiaki Nishijima, Vygantas Mizeikis, Yukie Yokota, and Hiroaki Misawa. Nanogap-assisted surface plasmon nanolithography. *J. Phys. Chem. Lett.*, 1(3):657–662, 2010.

[84] Jesper Tranekjær Jørgensen, Kamilla Norregaard, Pengfei Tian, Poul Martin Bendix, Andreas Kjaer, and Lene B Oddershede. Single particle and pet-based platform for identifying optimal plasmonic nano-heaters for photothermal cancer therapy. *Sci. Rep.*, 6(1):1–10, 2016.

[85] Kevin D Heylman, Kassandra A Knapper, and Randall H Goldsmith. Photothermal microscopy of nonluminescent single particles enabled by optical microresonators. *J. Phys. Chem. Lett.*, 5(11):1917–1923, 2014.

[86] Nicki Hogan, Shengxiang Wu, and Matthew Sheldon. Photothermalization and hot electron dynamics in the steady state. *J. Phys. Chem. C*, 124(9):4931–4945, 2019.

[87] Jin Zhong Zhang. Biomedical applications of shape-controlled plasmonic nanostructures: a case study of hollow gold nanospheres for photothermal ablation therapy of cancer. *J. Phys. Chem. Lett.*, 1(4):686–695, 2010.

[88] Minho Kim, Jung-Hoon Lee, and Jwa-Min Nam. Plasmonic photothermal nanoparticles for biomedical applications. *Adv. Sci.*, 6(17):1900471, 2019.

[89] Jing Wang, Yiting Chen, Xi Chen, Jiaming Hao, Min Yan, and Min Qiu. Photothermal reshaping of gold nanoparticles in a plasmonic absorber. *Opt. Express*, 19(15):14726–14734, 2011.

[90] Rituraj Borah and Sammy W Verbruggen. Silver–gold bimetallic alloy versus core–shell nanoparticles: Implications for plasmonic enhancement and photothermal applications. *J. Phys. Chem. C*, 124(22):12081–12094, 2020.

[91] Eric A Pozzi, Alyssa B Zrimsek, Clotilde M Lethiec, George C Schatz, Mark C Hersam, and Richard P Van Duyne. Evaluating single-molecule stokes and anti-stokes sers for nanoscale thermometry. *J. Phys. Chem. C*, 119(36):21116–21124, 2015.

[92] Aquiles Carattino, Martín Caldarola, and Michel Orrit. Gold nanoparticles as absolute nanothermometers. *Nano Lett.*, 18(2):874–880, 2018.

[93] Mariano Barella, Ianina L Violi, Julian Gargiulo, Luciana P Martinez, Florian Goschin, Victoria Guglielmotti, Diego Pallarola, Sebastian Schlucker, Mauricio Pilo-Pais, Guillermo P Acuna, et al. In situ photothermal response of single gold nanoparticles through hyperspectral imaging anti-stokes thermometry. *ACS Nano*, 2020.

[94] Juan Carlos Idrobo, Andrew R Lupini, Tianli Feng, Raymond R Unocic, Franklin S Walden, Daniel S Gardiner, Tracy C Lovejoy, Niklas Dellby, Sokrates T Pantelides, and Ondrej L Krivanek. Temperature measurement by a nanoscale electron probe using energy gain and loss spectroscopy. *Phys. Rev. Lett.*, 120(9):095901, 2018.

[95] Xingxu Yan, Chengyan Liu, Chaitanya A Gadre, Ruqian Wu, and Xiaoqing Pan. Probing thermal-induced phonon energy shift of sic in nanoscale by in situ vibrational spectroscopy. *Microsc. Microanal.*, 25(S2):622–623, 2019.

[96] David Boyer, Philippe Tamarat, Abdelhamid Maali, Brahim Lounis, and Michel Orrit. Photothermal imaging of nanometer-sized metal particles among scatterers. *Science*, 297(5584):1160–1163, 2002.

[97] Ilia M Pavlovetc, Eduard A Podshivaylov, Pavel A Frantsuzov, Gregory V Hartland, and Masaru Kuno. Quantitative infrared photothermal microscopy. In *Single Molecule Spectroscopy and Superresolution Imaging XIII*, volume 11246, page 1124613. International Society for Optics and Photonics, 2020.

[98] Ilia M Pavlovetc, Eduard A Podshivaylov, Rusha Chatterjee, Gregory V Hartland,

Pavel A Frantsuzov, and Masaru Kuno. Infrared photothermal heterodyne imaging: Contrast mechanism and detection limits. *J. Appl. Phys.*, 127(16):165101, 2020.

[99] Zhongming Li, Kyle Aleshire, Masaru Kuno, and Gregory V Hartland. Super-resolution far-field infrared imaging by photothermal heterodyne imaging. *J. Phys. Chem. B*, 121(37):8838–8846, 2017.

[100] Kyle Aleshire, Ilia M Pavlovetc, Robyn Collette, Xiang-Tian Kong, Philip D Rack, Shubin Zhang, David J Masiello, Jon P Camden, Gregory V Hartland, and Masaru Kuno. Far-field midinfrared superresolution imaging and spectroscopy of single high aspect ratio gold nanowires. *PNAS*, 117(5):2288–2293, 2020.

[101] Chad P Byers, Benjamin S Hoener, Wei-Shun Chang, Mustafa Yorulmaz, Stephan Link, and Christy F Landes. Single-particle spectroscopy reveals heterogeneity in electrochemical tuning of the localized surface plasmon. *J. Phys. Chem. B*, 118(49):14047–14055, 2014.

[102] Markus Selmke, Marco Braun, and Frank Cichos. Photothermal single-particle microscopy: detection of a nanolens. *ACS Nano*, 6(3):2741–2749, 2012.

[103] Harrison J Goldwyn, Stephan Link, and David J Masiello. Resolving resonance effects in the theory of single particle photothermal imaging. *arXiv preprint arXiv:2103.01494*, 2021.

[104] Subhasis Adhikari, Patrick Spaeth, Ashish Kar, Martin Dieter Baaske, Saumyakanti Khatua, and Michel Orrit. Photothermal microscopy: imaging the optical absorption of single nanoparticles and single molecules. *ACS Nano*, 14(12):16414–16445, 2020.

[105] Pierre Vermeulen, Laurent Cognet, and Brahim Lounis. Photothermal microscopy: optical detection of small absorbers in scattering environments. *Journal of microscopy*, 254(3):115–121, 2014.

[106] Yu-Chien Huang, Te-Hsin Chen, Jz-Yuan Juo, Shi-Wei Chu, and Chia-Lung Hsieh. Quantitative imaging of single light-absorbing nanoparticles by widefield interferometric photothermal microscopy. *ACS Photonics*, 8(2):592–602, 2021.

[107] Zhi-Cong Zeng, Hao Wang, Paul Johns, Gregory V Hartland, and Zachary D Schultz. Photothermal microscopy of coupled nanostructures and the impact of nanoscale heating in surface-enhanced raman spectroscopy. *The Journal of Physical Chemistry C*, 121(21):11623–11631, 2017.

[108] Kassandra A Knapper, Feng Pan, Morgan T Rea, Erik H Horak, Jeremy D Rogers, and Randall H Goldsmith. Single-particle photothermal imaging via inverted excitation through high-q all-glass toroidal microresonators. *Optics express*, 26(19):25020–25030, 2018.

[109] Richard W Taylor and Vahid Sandoghdar. Interferometric scattering microscopy: seeing single nanoparticles and molecules via rayleigh scattering. *Nano Letters*, 19(8):4827–4835, 2019.

[110] Gavin Young and Philipp Kukura. Interferometric scattering microscopy. *Annual review of physical chemistry*, 70:301–322, 2019.

[111] Zhonghong Shi, Jiufeng Huang, Xi Huang, Yangwei Huang, Lijun Wu, and Qiang Li. Resonant scattering enhanced interferometric scattering microscopy. *Nanoscale*, 12(14):7969–7975, 2020.

[112] Pedro MR Paulo, Alexander Gaiduk, Florian Kulzer, SF Gabby Krens, Herman P Spaink, Thomas Schmidt, and Michel Orrit. Photothermal correlation spectroscopy of gold nanoparticles in solution. *The Journal of Physical Chemistry C*, 113(27):11451–11457, 2009.

[113] Markus Selmke and Frank Cichos. The physics of the photothermal detection of single absorbing nano-objects: A review. *arXiv preprint arXiv:1510.08669*, 2015.

[114] Hung-Yi Chung, Pui-Tak Leung, and Din-Ping Tsai. Dynamic modifications of polarizability for large metallic spheroidal nanoshells. *The Journal of chemical physics*, 131(12):124122, 2009.

[115] Alexander Moroz. Depolarization field of spheroidal particles. *J. Opt. Soc. of Am. B*, 26(3):517–527, 2009.

[116] Zhonghong Shi, Xiaorui Tian, Zhangzeng Luo, Rongchen Huang, Lijun Wu, and Qiang Li. Photothermal imaging of individual nano-objects with large scattering cross sections. *The Journal of Physical Chemistry A*, 124(8):1659–1665, 2020.

[117] Qiang Li, Zhonghong Shi, Lijun Wu, and Hong Wei. Resonant scattering-enhanced photothermal microscopy. *Nanoscale*, 12(15):8397–8403, 2020.

[118] Daniel W Brandl, Nikolay A Mirin, and Peter Nordlander. Plasmon modes of nanosphere trimers and quadrumers. *J. Phys. Chem. B*, 110(25):12302–12310, 2006.

[119] Kui Bao, Nikolay A Mirin, and Peter Nordlander. Fano resonances in planar silver nanosphere clusters. *Appl. Phys. A*, 100(2):333–339, 2010.

[120] Zhong-Jian Yang, Zong-Suo Zhang, Wei Zhang, Zhong-Hua Hao, and Qu-Quan Wang. Twinned fano interferences induced by hybridized plasmons in au–ag nanorod heterodimers. *Appl. Phys. Lett.*, 96(13):131113, 2010.

[121] Bo Yan, Svetlana V Boriskina, and Bjoirn M Reinhard. Optimizing gold nanoparticle cluster configurations (n$\leq$ 7) for array applications. *J. Phys. Chem. C*, 115(11):4578–4583, 2011.

[122] Colleen L Nehl and Jason H Hafner. Shape-dependent plasmon resonances of gold nanoparticles. *J. Mater. Chem.*, 18(21):2415–2419, 2008.

[123] Daniel Dregely, Mario Hentschel, and Harald Giessen. Excitation and tuning of higher-order fano resonances in plasmonic oligomer clusters. *ACS Nano*, 5(10):8202–8211, 2011.

[124] Peter Nordlander and Emil Prodan. Plasmon hybridization in nanoparticles near metallic surfaces. *Nano Lett.*, 4(11):2209–2213, 2004.

[125] Yumin Wang, Ziwei Li, Ke Zhao, Ali Sobhani, Xing Zhu, Zheyu Fang, and Naomi J Halas. Substrate-mediated charge transfer plasmons in simple and complex nanoparticle clusters. *Nanoscale*, 5(20):9897–9901, 2013.

[126] Nathaniel K Grady, Naomi J Halas, and Peter Nordlander. Influence of dielectric function properties on the optical response of plasmon resonant metallic nanoparticles. *Chem. Phys. Lett.*, 399(1-3):167–171, 2004.

[127] Molly M Miller and Anne A Lazarides. Sensitivity of metal nanoparticle surface plasmon resonance to the dielectric environment. *J. Phys. Chem. B*, 109(46):21556–21565, 2005.

[128] Paul L Stiles, Jon A Dieringer, Nilam C Shah, and Richard P Van Duyne. Surface-enhanced raman spectroscopy. *Annu. Rev. Anal. Chem.*, 1:601–626, 2008.

[129] Kandammathe Valiyaveedu Sreekanth, Yunus Alapan, Mohamed El Kabbash, Efe Ilker, Michael Hinczewski, Umut A Gurkan, Antonio De Luca, and Giuseppe Strangi. Extreme sensitivity biosensing platform based on hyperbolic metamaterials. *Nat. Mater.*, 15(6):621–627, 2016.

[130] Thomas Schadle and Boris Mizaikoff. Mid-infrared waveguides: a perspective. *Appl. Spectrosc.*, 70(10):1625–1638, 2016.

[131] James R Adleman, David A Boyd, David G Goodwin, and Demetri Psaltis. Heterogenous catalysis mediated by plasmon heating. *Nano Lett.*, 9(12):4417–4423, 2009.

[132] Jun Guo, Yin Zhang, Lin Shi, Yanfei Zhu, Megersa F Mideksa, Ke Hou, Wenshi Zhao, Dawei Wang, Meiting Zhao, Xiaofei Zhang, and et al. Boosting hot electrons in hetero-superstructures for plasmon-enhanced catalysis. *J. Am. Chem. Soc.*, 139(49):17964–17972, 2017.

[133] César Clavero. Plasmon-induced hot-electron generation at nanoparticle/metal-oxide interfaces for photovoltaic and photocatalytic devices. *Nat. Photon.*, 8(2):95, 2014.

[134] Amir Zada, Pir Muhammad, Waqas Ahmad, Zahid Hussain, Sharafat Ali, Maaz Khan, Qasim Khan, and Muhammad Maqbool. Surface plasmonic-assisted photocatalysis and optoelectronic devices with noble metal nanocrystals: design, synthesis, and applications. *Adv. Funct. Mater.*, 30(7):1906744, 2020.

[135] Stephan Link and Mostafa A El-Sayed. Size and temperature dependence of the plasmon absorption of colloidal gold nanoparticles. *J. Phys. Chem. B*, 103(21):4212–4217, 1999.

[136] Rongchao Jin, YunWei Cao, Chad A Mirkin, K Lance Kelly, George C Schatz, and JG Zheng. Photoinduced conversion of silver nanospheres to nanoprisms. *Science*, 294(5548):1901–1903, 2001.

[137] Prashant K Jain, Wenyu Huang, and Mostafa A El-Sayed. On the universal scaling behavior of the distance decay of plasmon coupling in metal nanoparticle pairs: a plasmon ruler equation. *Nano Lett.*, 7(7):2080–2088, 2007.

[138] Christopher Tabor, Desiree Van Haute, and Mostafa A El-Sayed. Effect of orientation on plasmonic coupling between gold nanorods. *ACS Nano*, 3(11):3670–3678, 2009.

[139] Alison M Funston, Carolina Novo, Tim J Davis, and Paul Mulvaney. Plasmon coupling of gold nanorods at short distances and in different geometries. *Nano Lett.*, 9(4):1651–1658, 2009.

[140] LinLin Zhao, K Lance Kelly, and George C Schatz. The extinction spectra of silver nanoparticle arrays: influence of array structure on plasmon resonance wavelength and width. *J. Phys. Chem. B*, 107(30):7343–7350, 2003.

[141] Emilie Ringe, Jeffrey M McMahon, Kwonnam Sohn, Claire Cobley, Younan Xia, Jiaxing Huang, George C Schatz, Laurence D Marks, and Richard P Van Duyne. Unraveling the effects of size, composition, and substrate on the localized surface plasmon resonance frequencies of gold and silver nanocubes: a systematic single-particle approach. *J. Phys. Chem. C*, 114(29):12511–12516, 2010.

[142] Fritz Keilmann and Rainer Hillenbrand. Near-field microscopy by elastic light scattering from a tip. *Philos. Trans. R. Soc. A*, 362(1817):787–805, 2004.

[143] Eliza Hutter and Janos H Fendler. Exploitation of localized surface plasmon resonance. *Adv. Mater.*, 16(19):1685–1706, 2004.

[144] Anatoly V Zayats, Igor I Smolyaninov, and Alexei A Maradudin. Nano-optics of surface plasmon polaritons. *Phys. Rep.*, 408(3-4):131–314, 2005.

[145] Mathieu Kociak and Odile Stéphan. Mapping plasmons at the nanometer scale in an electron microscope. *Chem. Soc. Rev.*, 43(11):3865–3883, 2014.

[146] Yueying Wu, Guoliang Li, and Jon P Camden. Probing nanoparticle plasmons with electron energy loss spectroscopy. *Chem. Rev.*, 118(6):2994–3031, 2017.

[147] Charles Cherqui, Niket Thakkar, Guoliang Li, Jon P Camden, and David J Masiello. Characterizing localized surface plasmons using electron energy-loss spectroscopy. *Annu. Rev. Phys. Chem.*, 67:331–357, 2016.

[148] Nicholas W. Bigelow, Alex Vaschillo, Vighter Iberi, Jon P. Camden, and David J. Masiello. Characterization of the electron- and photon-driven plasmonic excitations of metal nanorods. *ACS Nano*, 6(8):7497–7504, 2012. PMID: 22849410.

[149] Charles Cherqui, Guoliang Li, Jacob A. Busche, Steven C. Quillin, Jon P. Camden, and David J. Masiello. Multipolar nanocube plasmon mode-mixing in finite substrates. *J. Phys. Chem. Lett.*, 9(3):504–512, 2018.

[150] Guoliang Li, Charles Cherqui, Nicholas W. Bigelow, Gerd Duscher, Patrick J. Straney, Jill E. Millstone, David J. Masiello, and Jon P. Camden. Spatially mapping energy transfer from single plasmonic particles to semiconductor substrates via stem/eels. *Nano Lett.*, 15:3465–3471, 2015.

[151] Yueying Wu, Guoliang Li, Charles Cherqui, Nicholas W. Bigelow, Niket Thakkar, David J. Masiello, Jon P. Camden, and Philip D. Rack. Electron energy loss spectroscopy study of the full plasmonic spectrum of self-assembled au-ag alloy nanoparticles: unraveling size, composition, and substrate effects. *ACS Photonics*, 3(1):130–138, 2016.

[152] Ardavan F Oskooi, David Roundy, Mihai Ibanescu, Peter Bermel, John D Joannopoulos, and Steven G Johnson. Meep: A flexible free-software package for electromagnetic simulations by the fdtd method. *Comput. Phys. Commun.*, 181(3):687–702, 2010.

[153] Ulrich Hohenester and Andreas Trügler. Mnpbem–a matlab toolbox for the simulation of plasmonic nanoparticles. *Comput. Phys. Commun.*, 183(2):370–381, 2012.

[154] Mohammad Mahdi Salary, Ali Forouzmand, and Hossein Mosallaei. Model order reduction of large-scale metasurfaces using a hierarchical dipole approximation. *ACS Photonics*, 4(1):63–75, 2017.

[155] Mohammad Mahdi Tajdini and Hossein Mosallaei. Characterization of large array of plasmonic nanoparticles on layered substrate: dipole mode analysis integrated with complex image method. *Opt. Express*, 19:A173–A193, 2011.

[156] Sarah Griffin, Nicholas P. Montoni, Guoliang Li, Patrick J. Straney, Jill E. Millstone, David J. Masiello, and Jon P. Camden. Imaging energy transfer in pt-decorated au

nanoprisms via electron energy-loss spectroscopy. *J. Phys. Chem. Lett.*, 7(19):3825–3832, 2016. PMID: 27617864.

[157] Jessica Rodriguez-Fernandez, Carolina Novo, Viktor Myroshnychenko, Alison M. Funston, Ana Sánchez-Iglesias, Isabel Pastoriza-Santos, Jorge Perez-Juste, F. Javier Garcia de Abajo, Luis M. Liz-Marzan, and Paul Mulvaney. Spectroscopy, imaging, and modeling of individual gold decahedra. *J. Phys. Chem. C*, 113(43):18623–18631, 2009.

[158] Ondrej L. Krivanek, Tracy C. Lovejoy, Niklas Dellby, Toshihiro Aoki, R. W. Carpenter, Peter Rez, Emmanuel Soignard, Jiangtao Zhu, Philip E. Batson, Maureen J. Lagos, and et al. Vibrational spectroscopy in the electron microscope. *Nature*, 514(7521):209–212, 2014.

[159] Jordan A. Hachtel, Andrew R. Lupini, and Juan Carlos Idrobo. Exploring the capabilities of monochromated electron energy loss spectroscopy in the infrared regime. *Sci. Rep.*, 8(1):5637, 2018.

[160] T.C. Lovejoy, G.C. Corbin, N. Dellby, M.V. Hoffman, and O.L. Krivanek. Advances in ultra-high energy resolution stem-eels. *Microsc. Microanal.*, 24(S1):446–s447, 2018.

[161] Vincent Basile and Kevin Murray. Uncovering the need for diversity among k–12 stem educators. *Teacher Education and Practice*, 28(2/3):255–268, 2015.

[162] June E Downing and Kathryn D Peckham-Hardin. Inclusive education: What makes it a good education for students with moderate to severe disabilities? *Research and Practice for Persons with Severe Disabilities*, 32(1):16–30, 2007.

[163] Jeffrey M Valla and Wendy Williams. Increasing achievement and higher-education representation of under-represented groups in science, technology, engineering, and mathematics fields: A review of current k-12 intervention programs. *Journal of women and minorities in science and engineering*, 18(1), 2012.

[164] Enrica Ruggs and Michelle Hebl. Literature overview: Diversity, inclusion, and cultural awareness for classroom and outreach education. *Apply research to practice (ARP) resources*, pages 9781315437453–3, 2012.

[165] Marianne E Krasny. University k–12 science outreach programs: How can we reach a broad audience? *BioScience*, 55(4):350–359, 2005.

[166] Alexa R Warwick, Angela Kolonich, Kristin M Bass, Louise S Mead, and Frieda Reichsman. Ten simple rules for partnering with k–12 teachers to support broader impact goals, 2020.

[167] Patrice Potvin and Abdelkrim Hasni. Interest, motivation and attitude towards science and technology at k-12 levels: a systematic review of 12 years of educational research. *Studies in science education*, 50(1):85–129, 2014.

[168] Lisa Tsui. Effective strategies to increase diversity in stem fields: A review of the research literature. *The Journal of Negro Education*, pages 555–581, 2007.

[169] Tonny Oyana, Sonia Garcia, Timothy Hawthorne, Jennifer Haegele, Joe Morgan, and Nekya Young. Nurturing diversity in stem fields through geography: The past, the present, and the future. *Journal of STEM Education*, 16(2), 2015.

[170] Jennifer DeWitt and Louise Archer. Participation in informal science learning experiences: the rich get richer? *International Journal of Science Education, Part B*, 7(4):356–373, 2017.

[171] Heidi B Carlone and Angela Johnson. Understanding the science experiences of successful women of color: Science identity as an analytic lens. *Journal of Research in Science Teaching: The Official Journal of the National Association for Research in Science Teaching*, 44(8):1187–1218, 2007.

[172] Richard H Kozoll and Margery D Osborne. Finding meaning in science: Lifeworld, identity, and self. *Science Education*, 88(2):157–181, 2004.

[173] John Fraser and Patricia Ward. Ise professionals knowledge and attitudes regarding science identity for learners in informal environments: Results of a national survey. *ILI Draft Report*, 91104, 2009.

[174] Mark J Graham, Jennifer Frederick, Angela Byars-Winston, Anne-Barrie Hunter, and Jo Handelsman. Increasing persistence of college students in stem. *Science*, 341(6153):1455–1456, 2013.

[175] Jennifer A Schon. *Science identity in informal education*. University of Idaho, 2015.

[176] Konrad J Schönborn, Gunnar E Höst, and KE Lundin Palmerius. Measuring understanding of nanoscience and nanotechnology: development and validation of the nano-knowledge instrument (nanoki). *Chem. Educ. Res. Pract.*, 16(2):346–354, 2015.

[177] H.S. Carslaw and J.C. Jaeger. *Conduction of Heat in Solids*. Oxford University Press, 2 edition, 1959.

[178] Michael Meier and A Wokaun. Enhanced fields on large metal particles: dynamic depolarization. *Optics letters*, 8(11):581–583, 1983.

[179] Steven C. Quillin, Charles Cherqui, Nicholas P. Montoni, Guoliang Li, Jon P. Camden, and David J. Masiello. Imaging plasmon hybridization in metal nanoparticle aggregates with electron energy-loss spectroscopy. *J. Phys. Chem. C*, 120(37):20852–20859, 2016.

[180] Jonathan A Fan, Chihhui Wu, Kui Bao, Jiming Bao, Rizia Bardhan, Naomi J Halas, Vinothan N Manoharan, Peter Nordlander, Gennady Shvets, and Federico Capasso. Self-assembled plasmonic nanoparticle clusters. *Science*, 328(5982):1135–1138, 2010.

[181] Thomas L Derrien, Shogo Hamada, Max Zhou, Detlef-M Smilgies, and Dan Luo. Three-dimensional nanoparticle assemblies with tunable plasmonics via a layer-by-layer process. *Nano Today*, 30:100823, 2020.

[182] Shawn J Tan, Michael J Campolongo, Dan Luo, and Wenlong Cheng. Building plasmonic nanostructures with dna. *Nat. Nanotechnol.*, 6(5):268, 2011.

[183] Carsten Sönnichsen, Björn M Reinhard, Jan Liphardt, and A Paul Alivisatos. A molecular ruler based on plasmon coupling of single gold and silver nanoparticles. *Nat. Biotechnol.*, 23(6):741–745, 2005.

[184] Prashant K Jain and Mostafa A El-Sayed. Plasmonic coupling in noble metal nanostructures. *Chem. Phys. Lett.*, 487(4-6):153–164, 2010.

[185] Baptiste Auguié and William L Barnes. Collective resonances in gold nanoparticle arrays. *Phys. Rev. Lett.*, 101(14):143902, 2008.

[186] Wolfgang SM Werner, Kathrin Glantschnig, and Claudia Ambrosch-Draxl. Optical constants and inelastic electron-scattering data for 17 elemental metals. *J. Phys. Chem. Ref. Data*, 38(4):1013–1092, 2009.

[187] Enrique J. Galvez. Gaussian beams - Colgate University. Unpublished, 2014.

[188] Claire A. West, Jesse Shooter, Katherine A. Willets, Stephan Link, and David J. Masiello. Nonlinear effects in photothermal imaging of strongly scattering plasmonic nanoparticles. Unpublished.

[189] Stefan Hollos. A Lattice Green Function Introduction. Unpublished, 2005.

[190] József Cserti. Application of the lattice green's function for calculating the resistance of an infinite network of resistors. *Am. J. Phys.*, 68(10):896–906, 2000.

Appendix A

COUPLED OSCILLATOR NORMAL MODE APPROACH

This Appendix outlines an approach to approximate the normal modes for a coupled nanoparticle system as coupled harmonic oscillators. This approach is exact for small spheres and spheroids, but once retardation effects are added the normal modes must be approximated numerically. The equation of motion for a damped, un-driven harmonic oscillator is

$$m\ddot{x} + m\gamma_{\text{tot}}\dot{x} + m\omega_0^2 x = 0 \tag{A.1}$$

where x is the oscillator coordinate, m is the mass of the oscillator, γ_{tot} is the total damping, and ω_0 is the resonance frequency. The following sections derive expressions for these oscillator parameters which enable the mapping of the dipole LSP onto harmonic oscillator equations of motion.

A.1 Resonance frequency and effective mass for quasi-static sphere

These derivations begin with the Clausius–Mossotti polarizability and the Drude model:

$$\alpha(\omega) = \frac{3V}{4\pi}\frac{\epsilon(\omega) - \epsilon_b}{\epsilon(\omega) + 2\epsilon_b} \tag{A.2}$$

$$\epsilon(\omega) = \epsilon_\infty - \frac{\omega_p^2}{\omega^2 + i\omega\gamma} \tag{A.3}$$

Multiplying the numerator and denominator of Eq. A.2 by $(\omega^2 + i\omega\gamma)$ gives

$$\alpha(\omega) = \frac{3V}{4\pi}\frac{(\epsilon_\infty - \epsilon_b)(\omega^2 + i\omega\gamma) - \omega_p^2}{(\epsilon_\infty + 2\epsilon_b)(\omega^2 + i\omega\gamma) - \omega_p^2}. \tag{A.4}$$

To define m and ω_0 in terms of an oscillator equation of motion, recall that $\alpha(\omega)$ can be written in the form:

$$\alpha(\omega) = \frac{e}{E}x(\omega) = \frac{e^2/m}{(-\omega^2 - i\omega\gamma + \omega_0^2)}. \tag{A.5}$$

To isolate the $-\omega^2$ term in the denominator of Eq. A.4, multiply the numerator and denominator by $-1/(\epsilon_\infty + 2\epsilon_b)$. This leaves Eq. A.4 as:

$$\begin{aligned}\alpha(\omega) &= \frac{3V}{4\pi}\frac{\frac{(\epsilon_\infty-\epsilon_b)}{(\epsilon_\infty+2\epsilon_b)}(-\omega^2 - i\omega\gamma) + \omega_p^2/(\epsilon_\infty + 2\epsilon_b)}{-\omega^2 - i\omega\gamma + \omega_p^2/(\epsilon_\infty + 2\epsilon_b)} \\ &= \frac{3V}{4\pi}\frac{\frac{(\epsilon_\infty-\epsilon_b)}{(\epsilon_\infty+2\epsilon_b)}(-\omega^2 - i\omega\gamma) + \omega_0^2}{-\omega^2 - i\omega\gamma + \omega_0^2}\end{aligned} \tag{A.6}$$

This enables the definition of ω_0 to be:

$$\omega_0 = \sqrt{\frac{\omega_p^2}{\epsilon_\infty + 2\epsilon_b}} \tag{A.7}$$

In the numerator, add and subtract $\frac{\epsilon_\infty-\epsilon_b}{\epsilon_\infty+2\epsilon_b}\omega_0^2$ to cancel the left term in the numerator with the denominator. This results in the static part and the ω varying part

$$\alpha(\omega) = \frac{3V}{4\pi}\left[\frac{\epsilon_\infty - \epsilon_b}{\epsilon_\infty + 2\epsilon_b} + \frac{\omega_0^2 - \frac{\epsilon_\infty-\epsilon_b}{\epsilon_\infty+2\epsilon_b}\omega_0^2}{-\omega^2 - i\omega\gamma + \omega_0^2}\right]. \tag{A.8}$$

Lastly, take the second term in the polarizability, and compare this to Eq. A.5 to define m:

$$\begin{aligned}\frac{e^2}{m} &= \frac{3V}{4\pi}\left[\omega_0^2 - \frac{\epsilon_\infty - \epsilon_b}{\epsilon_\infty + 2\epsilon_b}\omega_0^2\right] \\ &= \frac{3V}{4\pi}\left[\frac{\epsilon_\infty + 2\epsilon_b - \epsilon_\infty + \epsilon_b}{\epsilon_\infty + 2\epsilon_b}\right]\omega_0^2 \\ &= \frac{3V}{4\pi}\left[\frac{3\epsilon_b}{\epsilon_\infty + 2\epsilon_b}\right]\omega_0^2\end{aligned} \tag{A.9}$$

After plugging in $V = \frac{4}{3}\pi a^3$, this leads to:

$$m = \frac{e^2}{a^3\omega_0^2}\frac{(\epsilon_\infty + 2\epsilon_b)}{3\epsilon_b} \tag{A.10}$$

A.2 Resonance frequency and effective mass for quasi-static prolate spheroid

The polarizability for a prolate spheroid is defined as [27]:

$$\alpha(\omega) = \frac{V}{4\pi}\frac{\epsilon - \epsilon_b}{L(\epsilon - \epsilon_b) + \epsilon_b} \tag{A.11}$$

where L is a geometric factor ($L_{\text{sphere}} = \frac{1}{3}$)

$$\begin{aligned} L_z &= \frac{1 - e_s^2}{e_s^3}(-e_s + \tanh^{-1} e_s) \\ L_x &= L_y = \frac{1 - L_z}{2} \end{aligned} \tag{A.12}$$

and the eccentricity, e_s:

$$e_s = \sqrt{\frac{c^2 - a^2}{c^2}}. \tag{A.13}$$

Following the same procedure as above, the Drude mode (Eq. 2.2) may be plugged into the polarizability for the prolate spheroid (Eq. A.11) and multiplied by $(\omega^2 + i\omega\gamma)$:

$$\alpha(\omega) = \frac{V}{4\pi}\frac{(\epsilon_\infty - \epsilon_b)(\omega^2 + i\omega\gamma) - \omega_p^2}{[L(\epsilon_\infty - \epsilon_b) + \epsilon_b](\omega^2 + i\omega\gamma) - L\omega_p^2} \tag{A.14}$$

Then isolating the ω^2 term in the denominator returns:

$$\alpha(\omega) = \frac{V}{4\pi}\frac{[(\epsilon_\infty - \epsilon_b)(\omega^2 + i\omega\gamma) - \omega_p^2]/[L(\epsilon_\infty - \epsilon_b) + \epsilon_b]}{\omega^2 + i\omega\gamma - L\omega_p^2/[L(\epsilon_\infty - \epsilon_b) + \epsilon_b]}. \tag{A.15}$$

This allows for the definition of ω_0 when comparison to Eq. A.5 as:

$$\omega_0^2 = \frac{L\omega_p^2}{L(\epsilon_\infty - \epsilon_b) + \epsilon_b}. \tag{A.16}$$

Plugging in w_0 and simplify out terms in numerator:

$$\alpha(\omega) = \frac{V}{4\pi}\left[\frac{\frac{(\epsilon_\infty-\epsilon_b)(-\omega^2-i\omega\gamma)}{L(\epsilon_\infty-\epsilon_b)+\epsilon_b}+\omega_0^2/L}{-\omega^2-i\omega\gamma+\omega_0^2}\right]. \tag{A.17}$$

Separating the static and dynamic terms by adding and subtracting terms in the numerator,

$$\begin{aligned}\alpha(\omega) &= \frac{V}{4\pi}\left[\frac{\frac{(\epsilon_\infty-\epsilon_b)(-\omega^2-i\omega\gamma+w_0^2)}{L(\epsilon_\infty-\epsilon_b)+\epsilon_b}-\frac{(\epsilon_\infty-\epsilon_b)\omega_0^2}{L(\epsilon_\infty-\epsilon_b)+\epsilon_b}+\omega_0^2/L}{-\omega^2-i\omega\gamma+\omega_0^2}\right] \\ &= \frac{V}{4\pi}\left[\frac{(\epsilon_\infty-\epsilon_b)}{L(\epsilon_\infty-\epsilon_b)+\epsilon_b}-\frac{\frac{(\epsilon_\infty-\epsilon_b)\omega_0^2}{L(\epsilon_\infty-\epsilon_b)+\epsilon_b}+\omega_0^2/L}{-\omega^2-i\omega\gamma+\omega_0^2}\right].\end{aligned} \tag{A.18}$$

Then by taking the dynamic part, and setting it equal to the oscillator polarizability

$$\begin{aligned}\frac{e^2}{m} &= \frac{V}{4\pi}\left[\frac{-(\epsilon_\infty-\epsilon_b)\omega_0^2}{L(\epsilon_\infty-\epsilon_b)+\epsilon_b}+\omega_0^2/L\right] \\ &= \frac{V}{4\pi}\left[\frac{\omega_0^2\epsilon_b}{L^2(\epsilon_\infty-\epsilon_b)+L\epsilon_b}\right].\end{aligned} \tag{A.19}$$

Therefore,

$$m = \frac{4\pi e^2}{V}\frac{L^2(\epsilon_\infty-\epsilon_b)+L\epsilon_b}{\omega_0^2\epsilon_b} \tag{A.20}$$

A.3 Long-wavelength approximation

For particles outside of the quasi-static limit, retardation effects must be considered. This was first derived analytically in Ref. [178] for a sphere by defining a depolarization field, $\mathbf{E}_{\text{dep}}$, which corresponds to the field generated by the polarized matter surrounding the center of the particle. The polarization $\mathbf{P}$ of the sphere is $4\pi\mathbf{P} = (\epsilon-1)(\mathbf{E}_0+\mathbf{E}_{\text{dep}})$. The field $\mathbf{E}_{\text{dep}}$ is then determined by assigning a dipole moment, $d\mathbf{p}(\mathbf{r}) = \mathbf{P}dV$, to each volume element, calculating the retarded dipole field generated by $d\mathbf{p}$, and integrating over the volume of the sphere by expanding the Mie coefficients and only keeping terms up to k^3.

Ref. [115] continued this derivation and arrived at a modified polarizability for spheroids:

$$\alpha_{\mathrm{MW}} = \frac{\alpha}{1 - \frac{k^2}{l_E} D\alpha - i\frac{2k^3}{3}\alpha} \tag{A.21}$$

where D is the dynamic geometric factor ($D_{\mathrm{sphere}} = 1$)

$$\begin{aligned} D_z &= \frac{3}{4}\Big(\frac{1+e_s^2}{1-e_s^2} L_z + 1\Big) \\ D_x = D_y &= \frac{a}{2c}\Big(\frac{3}{e_s}\tanh^{-1} e_s - D_z\Big) \end{aligned} \tag{A.22}$$

The oscillator polarizability can be subbed in for α, and α_{MW} can be rewritten in the same form as α_{osc} by defining modified dipole parameters, $\tilde{m}, \tilde{\gamma}, \tilde{\omega}_0$.

$$\begin{aligned} \alpha_{\mathrm{MW}} &= \frac{1}{\frac{-\omega^2 - i\omega\gamma + \omega_0^2}{e^2/m} - \frac{k^2}{l_E} D - i\frac{2}{3}k^3} \\ &= \frac{e^2/m}{-\omega^2 - i\omega\gamma\omega_0^2 - \frac{e^2}{m}\frac{D}{l_E}\frac{n^2}{c^2}\omega^2 - i\frac{2}{3}\frac{e^2}{m}\frac{n^3}{c^3}\omega^3} \\ &= \frac{e^2/m}{-\omega^2(1 + \frac{e^2}{m}\frac{D}{l_E}\frac{n^2}{c^2}) - i\omega(\gamma + \frac{2}{3}\frac{e^2}{m}\frac{n^3}{c^3}\omega^2) + \omega_0^2} \\ &= \frac{e^2/m(1 + \frac{e^2}{m}\frac{D}{l_E}\frac{n^2}{c^2})^{-1}}{-\omega^2 - i\omega(\gamma + \frac{2}{3}\frac{e^2}{m}\frac{n^3}{c^3}\omega^2)(1 + \frac{e^2}{m}\frac{D}{l_E}\frac{n^2}{c^2})^{-1} + \omega_0^2(1 + \frac{e^2}{m}\frac{D}{l_E}\frac{n^2}{c^2})^{-1}} \\ &= \frac{e^2/\tilde{m}}{-\omega^2 - i\omega\tilde{\gamma} + \tilde{\omega}_0^2} \end{aligned} \tag{A.23}$$

where

$$\begin{aligned} \tilde{m} &= m\Big(1 + \frac{e^2}{m}\frac{D}{l_E}\frac{n^2}{c^2}\Big) = m + \frac{e^2 D}{l_E}\frac{n^2}{c^2} \\ \tilde{\gamma} &= \frac{\gamma + \frac{2}{3}\frac{e^2}{m}\frac{n^3}{c^3}\omega^2}{1 + \frac{e^2}{m}\frac{D}{l_E}\frac{n^2}{c^2}} \\ &= \frac{m(\gamma + \frac{2}{3}\frac{e^2}{m}\frac{n^3}{c^3}\omega^2)}{\tilde{m}} \\ &= \frac{m}{\tilde{m}}\gamma + \frac{2e^2 n^3}{3\tilde{m}c^3}\omega^2 \end{aligned} \tag{A.24}$$

Appendix B

DERIVATION OF GAUSSIAN BEAM

This derivation is included in this dissertation because there are multiple ways of deriving the Gaussian beam which lead to physically different answers. This derivation follows the unpublished notes in Ref. [187]

This derivation seeks a solution to he wave equation:

$$\nabla^2 \mathbf{E}(\mathbf{x},t) - \frac{\epsilon}{c^2}\frac{\partial^2 \mathbf{E}(\mathbf{x},t)}{\partial t^2} = 0, \tag{B.1}$$

which has harmonic time-dependence and the appropriate symmetries. To begin, pull out the time-dependence in $\mathbf{E}$ by letting $\mathbf{E}(\mathbf{x},t) = \mathbf{U}(\mathbf{x})e^{-i\omega t}$, which reduces the wave equation to the Helmholtz equation:

$$\nabla^2 \mathbf{U}(\mathbf{x}) + k^2 \mathbf{U}(\mathbf{x}) = 0. \tag{B.2}$$

Taking the field to be a plane wave propagating along the z axis, $\mathbf{U}(\mathbf{x}) = \mathbf{U}_0(\mathbf{x})e^{ikz}$, but varies slowly with respect to z ($\partial^2 \mathbf{U}_0/\partial z^2 \approx 0$) leads to

$$\frac{\partial^2 \mathbf{U}_0(\mathbf{x})}{\partial x^2} + \frac{\partial^2 \mathbf{U}_0(\mathbf{x})}{\partial y^2} + 2ik\frac{\partial \mathbf{U}_0(\mathbf{x})}{\partial z} = 0. \tag{B.3}$$

Eq. B.3 is called the paraxial wave equation. Guess the solution to be of the following form:

$$U_0 = Ae^{ik(x^2+y^2)/2q(z)}e^{ip(z)} \tag{B.4}$$

where q is complex and takes the form $q(z) = z - iz_R$. Therefore,

$$\frac{1}{q(z)} = \frac{1}{z + z_R^2/z} + i\frac{1}{z^2/z_R + z_R} \tag{B.5}$$

Let $R(z) = z + z_R^2/z$, $k = 2\pi n_b/\lambda$, and given $w_0 = \sqrt{z_R\lambda/\pi n_b}$, then

$$w(z) = \frac{1}{w_0^2}\frac{1}{1 + z^2/z_R^2} \tag{B.6}$$

Finally, $e^{ip(z)} = \frac{w_0}{w(z)}e^{-i\psi(z)}$ where $\psi(z) = \arctan(z/z_r)$. By setting the focus to be at z_p, the final expression is:

$$\mathbf{E}_{\mathrm{g}}(\mathbf{x}, t) = E_0\hat{\mathbf{x}}\frac{w_0}{w(z)}e^{-(x^2+y^2)/w(z)^2}e^{ik(z-z_f)}e^{ik(x^2+y^2)/(2R(z))}e^{-i\psi(z)}e^{-i\omega t} \tag{B.7}$$

Appendix C

STEADY STATE HEAT DIFFUSION

In the steady-state, the time-dependent heat diffusion equation reduces to:

$$-\boldsymbol{\nabla}\cdot[\kappa(\mathbf{r})\boldsymbol{\nabla}T(\mathbf{r})]=Q(\mathbf{r}) \tag{C.1}$$

When considering the temperature outside of a nanoparticle heat source, this equation is quite easy to solve using an approach similar to Gauss's Law.

$$\begin{aligned}\int dV\boldsymbol{\nabla}\cdot[\kappa(\mathbf{r})\boldsymbol{\nabla}T(\mathbf{r})] &= -\int dVQ(\mathbf{r})\\ \oint dS\hat{\mathbf{r}}\cdot[\kappa(\mathbf{r})\boldsymbol{\nabla}T(\mathbf{r})] &= -P\\ \kappa(r=r')\frac{\partial T}{\partial r}(4\pi r^2) &= -P\end{aligned} \tag{C.2}$$

Integrating both sides leads to:

$$T(r)=\frac{P}{4\pi\kappa r} \tag{C.3}$$

where κ is the thermal conductivity of the background.

Appendix D

TIME-DEPENDENT HEAT DIFFUSION

D.1 Photothermal Time-Dependant Temperature Distribution

Necessary to modeling the photothermal imaging experiment is an appropriate model for the temperature distribution produced by a spherical, time dependant heat source. In photothermal experiments, the heating beam is typically amplitude modulated according to $P = \frac{1}{2}P_0(1 + \cos\Omega t)$. The spherical absorber will therefore provide the the following heat source

$$P_{\text{abs}}(t) = \frac{1}{2}P_{\text{abs},0}(1 + \cos\Omega t). \tag{D.1}$$

This power therefore may be used to define the time-dependant heat source. While there are numerous ways to solve the problem, I have followed an approach described in §2.6 of Ref. [177].

The starting assumption is that instead of a nanosphere heat source in an infinite background, we instead solve the problem of an infinitesimal heat source in an infinite background. Therefore, the following solution will only be valid at all points except exactly at the origin. Given that we won't be solving for the temperature at the origin, we can then solve the homogeneous, or heat diffusion equation without a heat source:

$$c_p\rho\frac{\partial T(\mathbf{r},t)}{\partial t} = \kappa\nabla^2 T(\mathbf{r},t) \tag{D.2}$$

where c_p is the specific heat capacity $\left[\frac{\text{J}}{\text{kg K}}\right]$, ρ is the mass density, and κ is the thermal conductivity. By superposition, this problem can be solved by calculating the time-independent term, T_1 (produced from the heat source $1/2P_0$), and the time-dependant term, T_2 (produced from the heat source $1/2P_0\cos\Omega t$). $2T_1$ has been solved for in Appendix C; the following

discussion will solve for T_2. At the end, the two solution will be added together.

Given the spherical symmetry of the problem, the Laplacian reduces to:

$$c_p\rho\frac{\partial T(r,t)}{\partial t} = \kappa\Big[\frac{2}{r}\frac{\partial T(r,t)}{\partial r} + \frac{\partial^2 T(r,t)}{\partial r^2}\Big] \tag{D.3}$$

Now make the substitution $v = rT(r,t)$ and define $C \equiv c_p\rho$ as the heat capacity per volume, Eq. D.3 then reduces to:

$$\frac{\partial v(r,t)}{\partial t} = \frac{\kappa}{C}\frac{\partial^2 v(r,t)}{\partial r^2}. \tag{D.4}$$

From here, suppose the solution: $v = u(r)e^{i\Omega t}$. Plugging this into Eq. D.4 results in:

$$\frac{\partial^2 u(r)}{\partial r^2} = \frac{C}{\kappa}i\Omega u(r) \tag{D.5}$$

This leads to the the clear guess of $u(r) = Ae^{-r\sqrt{iC\Omega/\kappa}} + Be^{r\sqrt{iC\Omega/\kappa}}$, yet because $u(r)$ cannot diverge as $r \to \infty$, then $B = 0$. Using the identity $\sqrt{i} = \frac{1}{\sqrt{2}}(1+i)$, $u(r)$ reduces to:

$$u(r) = Ae^{-ir\sqrt{C\Omega/2\kappa}}e^{-r\sqrt{C\Omega/2\kappa}} \tag{D.6}$$

At this point I will define $r_{\text{th}} \equiv \sqrt{2\kappa/C\Omega}$ to simplify the expressions. Going back to $v(r,t)$:

$$v(r,t) = Ae^{i(\Omega t - r/r_{\text{th}})}e^{-r/r_{\text{th}}} \tag{D.7}$$

The temperature must be real, so after taking the real part of Eq. D.7 and rewriting it in terms of $T(r,t)$

$$T(r,t) = \frac{A}{r}e^{-r/r_{\text{th}}}\cos\left(\Omega t - r/r_{\text{th}}\right) \tag{D.8}$$

To solve for A, enforce the following boundary condition of the flux at r' and $t = 0$:

$$\begin{aligned}
&\lim_{r'\to 0}\left[-\kappa\frac{\partial T}{\partial r} = \frac{P_{\text{abs}}(t=0)}{4\pi r^2}\right]_{r=r'} \\
&\lim_{r'\to 0}\left[-\frac{\partial}{\partial r}\Big[\frac{A}{r}e^{-r/r_{\text{th}}}\cos\big(-r/r_{\text{th}}\big)\Big] = \frac{1/2P_{\text{abs},0}}{4\pi\kappa r^2}\right]_{r=r'} \\
&\lim_{r'\to 0}\left[\frac{A}{r^2}e^{-r/r_{\text{th}}}\Big[(1+r/r_{\text{th}})\cos\big(r/r_{\text{th}}\big) + r/r_{\text{th}}\sin\big(r/r_{\text{th}}\big)\Big] = \frac{P_{\text{abs},0}}{8\pi\kappa r^2}\right]_{r=r'} \\
&\lim_{r'\to 0}\left[\frac{A}{r'^2} = \frac{P_{\text{abs},0}}{8\pi\kappa r'^2}\right] \\
&A = \frac{P_{\text{abs},0}}{8\pi\kappa}
\end{aligned} \tag{D.9}$$

Putting it together,

$$T(r,t) = \frac{P_{\text{abs},0}}{8\pi\kappa r}e^{-r/r_{\text{th}}}\cos\big(\Omega t - r/r_{\text{th}}\big) \tag{D.10}$$

This is the result for T_2. T_1 will be equal to the steady-state solution derived in Appendix C multiplied by $1/2$ given $P_{\text{abs}}(t=0) = 1/2P_{\text{abs},0}$.

$$T_1 = \frac{P_{\text{abs},0}}{8\pi\kappa r} \tag{D.11}$$

Putting it all together, $T(r,t)$:

$$\begin{aligned}
T(r,t) &= T_1 + T_2 \\
&= \frac{P_{\text{abs},0}}{8\pi\kappa r}\Big[1 + e^{-r/r_{\text{th}}}\cos\big(\Omega t - r/r_{\text{th}}\big)\Big]
\end{aligned} \tag{D.12}$$

It is useful to consider the physical importance of r_{th} introduced in the previous derivation. This quantity is commonly referred to as the thermal radius and sets the characteristic length for heat diffusion. This is the distance which bounds the region for which energy transfers appreciably to the environment.

Appendix E

GREEN'S FUNCTION OF A SPHERE

The following is a derivation of the Green's function for a sphere. Consider a sphere of radius a and a point charge at r'. The solution to Poisson's equation:

$$-\epsilon\nabla^2 G(\mathbf{r},\mathbf{r}';\omega) = 4\pi\delta(\mathbf{r}-\mathbf{r}'), \tag{E.1}$$

is given in Ref. [18] to be

$$G(\mathbf{r},\mathbf{r}';\omega) = \sum_{l,m}\left(A_{l,m}r^l + B_{l,m}r^{-(l+1)}\right)Y_{l,m}(\theta,\phi) \tag{E.2}$$

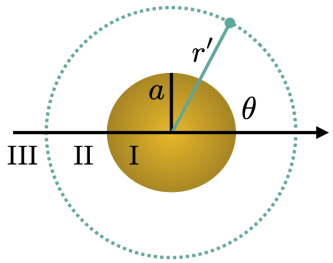

Figure E.1: Problem set up for solving for the Green's function of a sphere

where $Y_{l,m}(\theta,\phi)$ are the spherical harmonics. We know that in each region, the Green's function must take the following forms:

$$\begin{aligned}
\text{Region I}: \quad & G(\mathbf{r},\mathbf{r}';\omega) = \sum_{l,m} \big(A_{l,m} r^{l}\big) Y_{l,m}(\theta,\phi) \\
\text{Region II}: \quad & G(\mathbf{r},\mathbf{r}';\omega) = \sum_{l,m} \big(C_{l,m} r^{l} + D_{l,m} r^{-(l+1)}\big) Y_{l,m}(\theta,\phi) \\
\text{Region III}: \quad & G(\mathbf{r},\mathbf{r}';\omega) = \sum_{l,m} \big(F_{l,m} r^{-(l+1)}\big) Y_{l,m}(\theta,\phi)
\end{aligned} \tag{E.3}$$

subject to the following boundary conditions: $\mathbf{D}$ is continuous across the sphere boundary,

$$\epsilon(\omega) \frac{\partial G_{\mathrm{I}}}{\partial r}\Big|_{r=a} = \epsilon_b \frac{\partial G_{\mathrm{II}}}{\partial r}\Big|_{r=a}, \tag{E.4}$$

$\mathbf{D}$ is discontinuous across the δ boundary,

$$\epsilon_b \frac{\partial G_{\mathrm{III}}}{\partial r}\Big|_{r=r'} - \epsilon_b \frac{\partial G_{\mathrm{II}}}{\partial r}\Big|_{r=r'} = 4\pi\delta(\mathbf{r}-\mathbf{r}'), \tag{E.5}$$

G is continuous across the sphere boundary,

$$G_{\mathrm{I}}\big|_{r=a} = G_{\mathrm{II}}\big|_{r=a}, \tag{E.6}$$

and G is continuous across the δ boundary,

$$G_{\mathrm{II}}\big|_{r=r'} = G_{\mathrm{III}}\big|_{r=r'}. \tag{E.7}$$

Enforcing these conditions allows us to solve for $A_{l,m}, B_{l,m}, C_{l,m}, D_{l,m}$ and $F_{l,m}$ in Eq. E.3. Putting everything together leads to:

$$G(\mathbf{r},\mathbf{r}',\omega) = \frac{1}{\epsilon_b|\mathbf{r}-\mathbf{r}'|} - \sum_{l,m} \frac{4\pi}{2l+1} \frac{a^{2l+1}}{r'^{l+1} r^{(l+1)}} \frac{l[\epsilon(\omega)/\epsilon_b - 1]}{\epsilon_b + l[\epsilon(\omega)+\epsilon_b]} \mathrm{Y}_{lm}(\theta,\phi)\mathrm{Y}^{*}_{lm}(\theta',\phi') \tag{E.8}$$

Notice that for $l = 1$, the frequency dependence of Eq. E.8 is exactly the Clausius–Mossotti polarizability, Eq. 2.6.

Appendix F

COMPARISON BETWEEN TIME-INDEPENDENT AND TIME-DEPENDENT PHOTOTHERMAL SOLUTIONS

It is intuitively convenient to think about the photothermal signal after the lock-in has been preformed. Many in the field even start their theories that way. Furthermore, in Refs. [14, 10], the computations were performed in the time-independent limit which agreed well with experiment. This Appendix verifies that this approach is valid in the limit of large modulation frequency. Specifically, does the intensity which reaches the detector I_{det} minus the intensity of the background signal (i.e. signal when no NP exists) I_{bg} after both terms have been evaluated by the lock-in detector ($\mathcal{L}$) equal to a separate experiment wherein there is no lock in, and instead you're subtracting the static signal with the heating beam on minus the static signal of the heating beam off (yet the probe still over the NP):

$$\mathcal{L}\big[I_{\text{det}}(t) - I_{\text{bg}}(t)\big] \stackrel{?}{=} I_{\text{pump on}} - I_{\text{pump off}} \tag{F.1}$$

In this section, all variables with subscripts containing 0 do not change with time. Beginning with the left side of the equation:

$$\mathcal{L}\big[I_{\text{det}}(t) - I_{\text{bg}}(t)\big] = \mathcal{L}\big[|\mathbf{E}_{\text{sca}}(t)|^2 + 2\text{Re}[\mathbf{E}_{\text{p}}(t)\cdot\mathbf{E}^*_{\text{sca}}(t)]\big]. \tag{F.2}$$

The first term in Eq. F.2 is

$$\begin{aligned}\mathbf{E}_{\text{sca}}(t) &= \mathbf{G}\cdot\alpha_{\text{pt}}(t)\mathbf{E}_{\text{p}}(t)\\ &= \mathbf{G}\cdot\big[\alpha_{\text{pt},T_0} + \frac{d\alpha_{\text{pt}}}{dT}T_{\text{avg}}\big]\mathbf{E}_{\text{p},0}e^{-i\omega t}\end{aligned} \tag{F.3}$$

Recalling that the average temperature is defined as:

$$\begin{aligned} T_{\text{avg}}(t) &= \frac{P_{\text{abs},0} r_{\text{th}}^2}{\kappa V_{\text{th}}} \big(0.25 + c_1 \cos\Omega t + c_2 \sin\Omega t\big) \\ &\equiv T_{\text{avg},0} + T_{c_1,0} \cos\Omega t + T_{c_2,0} \sin\Omega t \end{aligned} \tag{F.4}$$

Returning to Eq. F.2, the time dependence in $|\mathbf{E}_{\text{sca}}(t)|^2$ and $2\text{Re}\big[\mathbf{E}_{\text{p}}(t) \cdot \mathbf{E}_{\text{sca}}(t)\big]$ need to be integrated out. Performing this on the first term:

$$\begin{aligned} &\frac{1}{\tau}\int_0^\tau |\mathbf{E}_{\text{sca}}(t)|^2 \begin{Bmatrix} \sin\Omega t \\ \cos\Omega t \end{Bmatrix} dt \\ &\quad= \int_0^\tau \left| \mathbf{G} \cdot \Big(\alpha_{\text{pt},T_0} + \frac{d\alpha_{\text{pt}}}{dT} \Big[T_{\text{avg},0} + T_{c_1,0} \cos\Omega t + T_{c_2,0} \sin\Omega t \Big] \Big) \mathbf{E}_{p,0} e^{-i\omega t} \right|^2 \begin{Bmatrix} \sin\Omega t \\ \cos\Omega t \end{Bmatrix} dt \\ &\quad\equiv \int_0^\tau \Big| \mathbf{E}_{\text{st}}(t) + \mathbf{E}_{\Omega}(t) \Big|^2 \begin{Bmatrix} \sin\Omega t \\ \cos\Omega t \end{Bmatrix} dt \end{aligned} \tag{F.5}$$

where for mathematical simplicity, $\mathbf{E}_{\Omega}$ and $\mathbf{E}_{\text{st}}$ are defined to separate the terms that have Ω dependence and terms do not.

$$\begin{aligned} \mathbf{E}_{\text{st}}(t) &\equiv \mathbf{G} \cdot \Big(\alpha_{\text{pt},T_0} + \frac{d\alpha_{\text{pt}}}{dT} T_{\text{avg},0} \Big) \mathbf{E}_{p,0} e^{-i\omega t} \\ &\equiv \mathbf{E}_{\text{st},0} e^{-i\omega t} \\ \mathbf{E}_{\Omega}(t) &\equiv \mathbf{G} \cdot \Big(\frac{d\alpha_{\text{pt}}}{dT} \Big[T_{c_1,0} \cos\Omega t + T_{c_2,0} \sin\Omega t \Big] \Big) \mathbf{E}_{p,0} e^{-i\omega t} \\ &\equiv \mathbf{E}_{\Omega,01} e^{-i\omega t} \cos\Omega t + \mathbf{E}_{\Omega,02} e^{-i\omega t} \sin\Omega t \end{aligned} \tag{F.6}$$

Expanding Eq. F.5 leads to:

$$\begin{aligned} &\frac{1}{\tau}\int_0^\tau \Big| \mathbf{E}_{\text{st},0} e^{-i\omega t} + \Big(\mathbf{E}_{\Omega,01} e^{-i\omega t} \cos\Omega t + \mathbf{E}_{\Omega,02} e^{-i\omega t} \sin\Omega t \Big) \Big|^2 \begin{Bmatrix} \sin\Omega t \\ \cos\Omega t \end{Bmatrix} dt \\ &= \frac{1}{\tau}\int_0^\tau 2\text{Re}\Big(\mathbf{E}_{\text{st},0} \cdot (\mathbf{E}_{\Omega,01}^* \cos\Omega t + \mathbf{E}_{\Omega,02}^* \sin\Omega t) \Big) \begin{Bmatrix} \sin\Omega t \\ \cos\Omega t \end{Bmatrix} dt \\ &= \text{Re}\big(\mathbf{E}_{\text{st},0} \cdot \big(\mathbf{E}_{\Omega,01}^* + \mathbf{E}_{\Omega,02}^* \big) \big) \end{aligned} \tag{F.7}$$

This leaves the last term in Eq. F.2,

$$\begin{aligned}
&\frac{2}{\tau}\int_0^\tau \mathrm{Re}\big(\mathbf{E}_{\mathrm{p}}(t)\cdot\mathbf{E}_{\mathrm{sca}}(t)^*\big)\begin{Bmatrix}\sin\Omega t\\ \cos\Omega t\end{Bmatrix}dt\\
&\quad=\frac{2}{\tau}\int_0^\tau \mathrm{Re}\Big(\mathbf{E}_{\mathrm{p},0}e^{-i\omega t}\cdot\big(\mathbf{E}^*_{\mathrm{st},0}e^{i\omega t}+\mathbf{E}^*_{\Omega,01}e^{i\omega t}\cos\Omega t+\mathbf{E}^*_{\Omega,02}e^{i\omega t}\sin\Omega t\big)\Big)\begin{Bmatrix}\sin\Omega t\\ \cos\Omega t\end{Bmatrix}dt\\
&\quad=\mathrm{Re}\big(\mathbf{E}_{\mathrm{p},0}\cdot\big(\mathbf{E}^*_{\Omega,01}+\mathbf{E}^*_{\Omega,02}\big)\big)
\end{aligned}\tag{F.8}$$

Putting this all together, the left side of Eq. F.1 is

$$\frac{cn_b}{8\pi}\Big[\mathrm{Re}\big(\mathbf{E}_{\mathrm{st},0}\cdot(\mathbf{E}^*_{\Omega,01}+\mathbf{E}^*_{\Omega,02})\big)+\mathrm{Re}\big(\mathbf{E}_{p,0}\cdot(\mathbf{E}^*_{\Omega,01}+\mathbf{E}^*_{\Omega,02})\big)\Big]\tag{F.9}$$

The last step is to define these functions in terms of the fields scattered when the heating beam is at a maximum power ($\mathbf{E}_H$) and minimum power ($\mathbf{E}_R$).

$$\begin{aligned}
\mathbf{E}_H \equiv&\mathbf{E}_{\mathrm{st},0}+\mathbf{E}_{\Omega,0}=\mathbf{G}\cdot\big(\alpha(T_R)+\frac{d\alpha}{dT}\Big|_{T=T_R}T_{\max}\big)\mathbf{E}_{p,0}\\
\mathbf{E}_R \equiv&\mathbf{E}_{\mathrm{st},0}-\mathbf{E}_{\Omega,0}=\mathbf{G}\cdot\alpha(T_R)\mathbf{E}_{p,0}
\end{aligned}\tag{F.10}$$

By taking the approximation $\mathbf{E}_{\Omega,0}\approx\mathbf{E}_{\Omega,01}+\mathbf{E}_{\Omega,02}$, then Eq. F.9 simplifies to

$$\frac{cn_b}{8\pi}\Big[|\mathbf{E}_H|^2-|\mathbf{E}_R|^2+\mathrm{Re}\big(\mathbf{E}_{p,0}\cdot(\mathbf{E}_H-\mathbf{E}_R)^*\big)\Big].\tag{F.11}$$

This approximation is valid for modulation frequencies around MHz. However if the frequency becomes too big, this approximation will not hold.

Now the right side of the equation:

$$I_{\text{heat on}}-I_{\text{heat off}}=\frac{cn_b}{8\pi}\Big[|\mathbf{E}_H+\mathbf{E}_{p,0}|^2-|\mathbf{E}_R+\mathbf{E}_{p,0}|^2\Big]\tag{F.12}$$

This reduces to:

$$\frac{cn_b}{8\pi}\Big[|\mathbf{E}_H|^2-|\mathbf{E}_R|^2+\mathrm{Re}\big(\mathbf{E}_{p,0}\cdot(\mathbf{E}_H-\mathbf{E}_R)^*\big)\Big]\tag{F.13}$$

Therefore, taking this time-independent approach is approximately equivalent to fully evaluating the lockin integral. The approximation breaks down when the modulation frequency is large.

Appendix G

NANOCAMP! INSTRUMENTS FOR EVALUATING SCIENCE IDENTITY AND CONTENT ENGAGEMENT

The following three instruments were used to access to what extend science identity and nanoscience content engagement changed over the course of the five-day summer camp.

G.1 Science Identity

This instrument was designed and validated in Ref. [175] to measure the change in middle and high school students' science identity after participating in an informal education environment (e.g.,outdoor science school). All questions from this instrument were used exactly in the study conducted herein to ensure validity and reliability. The questions were asked on a Likert scale: Strongly disagree, Disagree, Neither Agree nor Disagree, Agree, Strongly Agree. Responses were collected in a Google Form. The students' pre-survey and post-survey included this instrument.

1. I am good at science.

2. I know a lot about science.

3. I am good at most science experiments.

4. I understand science topics.

5. I learn new science topics easily.

6. I can use science equipment and/or technology to collect data.

7. I know how to use the scientific method method/process.

8. I can talk with others about science related topics.

9. I can create my own science experiments.

10. I can use my observations to create a hypothesis.

11. My friends see me as someone that is good at science.

12. When giving a science report, I feel like a scientist.

13. Others see me as a scientists when I share my observations.

14. When I share data I've collected, I feel like a scientist.

15. I can help others with science related topics.

G.2 Nanoscience Content Engagement

The following was the nanoscience survey given to the students before and after the camp. Most of the questions were taken from Ref. [176]. The full instrument was not used because the organizations we worked with did not want the students to take a long survey, and we wanted to cater the instrument to the nanoscience activities we had planned. Because the exact survey we gave the students had not been validated, we need to be careful about the conclusions we draw from it. I created questions 5, 10, 14, and 15.

G.2.1 Nanoscience Content Instrument

1. A nanometer is $1,000,000$ (1 million) times smaller than a meter (i.e., 1 m = 1,000,000 nm).

   (a) True

(b) False

2. Objects at the nanoscale are just large enough to be visible to the naked eye.

   (a) True

   (b) False

3. Nanomaterials do not occupy any volume.

   (a) True

   (b) False

4. Objects at the nanoscale can have different physical properties compared to their everyday, macroscopic counterparts.

   (a) True

   (b) False

5. Which of the following are 1 - 100 nm?

   (a) Carbon atom

   (b) Width of human hair

   (c) Width of DNA

   (d) Human blood cell

6. Nanotechnology allows scientists to arrange atoms, but only in ways that already occur in nature.

   (a) True

   (b) False

7. Carbon nanotubes consist of carbon atoms bonded to each other in a regular (repeating) pattern.

   (a) True

   (b) False

8. The properties of objects at the nanoscale may give rise to both advantages and risks of nanotechnology.

   (a) True

   (b) False

9. Pencil graphite, a diamond, a car tire, and charcoal are all made from the same atom, Carbon.

   (a) True

   (b) False

10. Researchers create nanomaterials by:

    (a) removing small sections of a material (similar to sculptures chipping away from a block of stone)

    (b) placing atoms or molecules one at a time

    (c) researchers do not make nanomaterials, all are found in nature

    (d) Both (a) and (b)

11. Forces between objects at the nanoscale are stronger when the surface area between them is larger.

    (a) True

(b) False

12. Objects at the nanoscale are kept in random motion by continuous collisions with other particles.

    (a) True

    (b) False

13. The extremely high surface area to volume relationship of objects at the nanoscale gives them different properties compared to everyday objects.

    (a) True

    (b) False

14. The gravitational force acting on a gold bar is as important to determining its properties as the gravitational force acting on a gold nanoparticle.

    (a) True

    (b) False

15. The multi-colored patterns (iridescence) we see in peacock feathers, oil spills, and bubbles is caused by the

    (a) material absorbing certain colors of light but not others

    (b) material reflecting light waves which interfere with one another

    (c) temperature of the material changing the way light interacts with it

    (d) electric charges in the material emitting different colors

G.3 Free Response Questions

During days two, three, and four, the students filled out the following three prompts:

1. What was your favorite activity today? Why?

2. What was one challenge you overcame in camp today?

3. What else would you like us to know?